Quantitative studies of porphyroblastic textures

by

David Marshall Hirsch, B.S.

Dissertation

Presented to the Faculty of the Graduate School of

The University of Texas at Austin

in Partial Fulfillment

of the Requirements

for the Degree of

Doctor of Philosophy
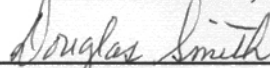
The University of Texas at Austin

December, 2000

Quantitative studies of porphyroblastic textures

Approved by
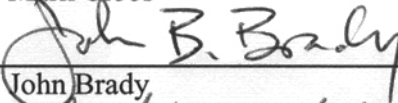**Dissertation Committee:**
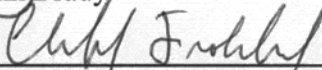
_____
William D. Carlson, Supervisor

_____
Douglas Smith

_____
Mark Cloos

_____
John Brady

_____
Clifford Frohlich

Dedication

This work is dedicated to my ever-patient wife, Heather.

Acknowledgements

Quantitative studies of porphyroblastic textures

David Marshall Hirsch, Ph.D.

The University of Texas at Austin, 2000

Supervisor: William D. Carlson

Advances in technology and theory – including high-resolution X-ray computed tomography, orientation contrast imaging, X-ray mapping of element abundances, and novel models and techniques for numerical simulation of crystallization – have recently made it possible to analyze textures in metamorphic rocks quantitatively. This study uses these methods to develop deeper understanding of porphyroblast crystallization in metamorphic rocks.

Statistical Tools. Spatial correlation functions are used to constrain metamorphic crystallization mechanisms in seven previously studied garnetiferous rocks from three localities. The results confirm prior inferences that the nucleation and growth rates of the garnet porphyroblasts in these specimens were governed by rates of intergranular diffusion.

Nucleation Mechanisms. Orientation contrast imaging (OCI) and electron backscatter diffraction patterns refute a recently published model for garnet nucleation and growth in rocks from Harpswell Neck, Maine that regards these porphyroblasts as compound crystals produced by coalescence of multiple individuals growing from independent nucleation centers, marked by high Mn concentrations. OCI reveals few crystallographic misorientations; those observed are mostly very small (< 1-2°) and do not correlate with Mn content. A favored interpretation invokes disequilibrium crystallization, in which garnet overgrows and inherits inhomogeneities in the Mn-content of its precursor matrix.

Nucleation Rates. In a pelitic schist from the Picuris Mountains, New Mexico, the size and abundance of equant biotite porphyroblasts vary from layer to layer on a ~3 cm scale. Two analyzed layers differ in mean crystal volume (10×10^{-4} *vs*. 2.4×10^{-4} cm^3), crystal number density (229 *vs*. 574 crystals per cm^3), and

volume fraction (20% *vs*. 13%). These variations result from differences in nucleation rates. Estimates from numerical simulations of biotite crystallization agree on an approximate crystallization interval of 12 m.y., implying different average nucleation rates of 19.1 and 47.8 nuclei cm^{-3} $m.y.^{-1}$.

Size vs. Grade. Garnet porphyroblasts in three Ca-rich pelites from the Waterville Formation, south-central Maine, spanning garnet through sillimanite grade, document diffusion-controlled nucleation and growth. Simulations of crystallization for the three samples, differing only in initial density of nucleation sites and the temperatures at the onset of nucleation, closely match measured crystal size distributions. This suggests that the commonly observed increase in crystal size with metamorphic grade may be a direct consequence of increasing nucleation temperature.

Table of Contents

List of Tables

List of Figures

Chapter 1. An evaluation of spatial correlation functions in textural analysis of metamorphic rocks

ABSTRACT

Spatial correlation functions, which quantify spatial relationships among porphyroblasts over a range of length scales, can be used in combination with other techniques of quantitative textural analysis to constrain crystallization mechanisms in metamorphic rocks. The utility, reliability, and robustness of these functions, however, depend critically upon correct methods of calculation and application to geological samples.

Application of the L'-function, Pair Correlation Function, and Mark Correlation Function (Stoyan and Stoyan, 1994) to artificial arrangements of crystals yields results consistent with their predetermined ordering and clustering qualities. These results serve as a foundation for the interpretation of more complex simulated and natural crystal arrays. Analysis of artificial and simulated crystal arrays in which ordering signals are obscured in various ways (displacing crystals in an ordered array by increasing amounts, reducing the number of crystals, and increasing the sample's aspect ratio) demonstrates that these scale-dependent functions are robust indicators of effects diagnostic of certain crystallization mechanisms, even in complex circumstances. The effects of clustering of nucleation sites, however, can strongly obscure any underlying signal that might reveal crystallization mechanisms.

The L'-function and the Pair Correlation Function are sensitive to short-range ordering of crystals, which may reflect suppression of nucleation in the vicinity of growing porphyroblasts. The Mark Correlation Function is sensitive to size-isolation correlations, which may reflect retardation of growth among crystals competing for nutrients. Interpretation of these functions, however, requires careful attention to proper calculation of Monte Carlo simulations, which are used to identify values of the functions that constitute a null-hypothesis region for comparison to samples with unknown ordering and clustering characteristics. To yield functional values commensurate with those calculated for a particular natural rock specimen, each simulation must match as closely as possible several critical features of the natural rock, including the set of crystal radii, limitations on the observability of crystals, and the shape and size of the bounding surface of the sample.

Crystallization mechanisms in seven previously studied garnetiferous rocks from three localities (Carlson et al., 1995; Denison and Carlson, 1997) have been re-assessed using both scale-dependent correlation functions and single-valued spatial statistics, both evaluated by comparison to rigorously computed null-hypothesis regions. The results confirm previous inferences that the nucleation and growth rates of the garnet porphyroblasts in these specimens were governed by rates of diffusion through the intergranular medium.

INTRODUCTION

Porphyroblast crystallization in metamorphic rocks results from the interplay of several atomic-scale processes involved in nucleation and growth. Because these cannot be directly observed, we must infer their relative importance and rates by reference to features in natural samples. One such avenue to understanding the kinetics of porphyroblast crystallization is through quantitative analysis of metamorphic textures. An obvious requirement for this is the existence of textural measures that discriminate among various processes that may have operated in the rocks during metamorphic recrystallization.

Recently, spatial correlation functions taken from the statistics literature and in use in the biological sciences have been proposed as promising tools for textural analysis (Raeburn, 1996; Daniel and Spear, 1999). This study examines these statistical measures to determine their utility, reliability, and extent of agreement with previously used statistics and other tools used to infer details of metamorphic processes and their kinetics.

BACKGROUND: DIFFUSIONAL VS. INTERFACIAL CONTROLS ON NUCLEATION AND GROWTH

During the crystallization of a metamorphic mineral, a number of interconnected processes must occur, as documented by numerous workers (Carmichael, 1969; Spry, 1969; Kretz, 1973, 1974; Walther and Wood, 1984; Rubie and Thompson, 1985; Ridley and Thompson, 1986; Carlson, 1989; Joesten, 1991; Kerrick et al., 1991; Kretz, 1994; Rubie, 1998). There must be heat input for the reaction to progress, if it is endothermic; the reactants must dissolve into the intergranular medium; chemical components of the mineral must diffuse through or be transported by the medium to the surface of the growing crystal; they must be incorporated into the structure of the crystal; and chemical species produced by the reaction but not incorporated into the crystal must diffuse or be transported away from the growing porphyroblast. Whichever of these sequential processes is the slowest will determine the overall rate of the reaction (Fisher, 1978). Because heat-flow control implies extremely limited nucleation, it is not thought to be a rate-limiting process during most episodes of metamorphic crystallization. The goal therefore reduces to discerning the differing effects of diffusional versus interfacial control on nucleation and growth. As described in Kretz (1974) and Carlson (1989), diffusional control (slow intergranular diffusion relative to the rate of surface reactions) affects both nucleation and growth. As preexisting crystals reduce the chemical affinity for reaction in their neighborhood by depleting the local nutrient supply, nucleation in this nearby region is suppressed, which

leads to spatial ordering of crystal centers relative to an interface-controlled case (Fig. 1.1). Continued reduction in chemical affinity near growing crystals causes the depleted zones for adjacent crystals to impinge, so these crystals tend to be smaller than more isolated crystals that nucleated at the same time (Fig. 1.2).

These effects of diffusional control on crystallization have measurable macroscopic consequences: the resulting textures should tend towards spatial ordering and should embody correlations between a crystal's size and measures of its degree of isolation. Spatial correlation functions can reveal these effects, and thus provide tests of competing hypotheses for the mechanisms that govern the crystallization of porphyroblasts.

In our description of the presumed effects of diffusion control on metamorphic textures, it is implicitly assumed that the precursor is sufficiently fine-grained so as to be uniform at the scale of a porphyroblast's depleted zone. This is required because heterogeneous nucleation on preferred surfaces of certain phases could control the distribution of nucleation sites, and the distribution of precursor phases that supply the reactant species can control the rate and amount of growth. To the extent that favored nucleation sites and localized sources of nutrients are inhomogeneously distributed at the scale of observation, textural features will depart from the idealized cases described below. As described below, part of the utility of correlation functions lies in their ability to identify such departures.

CORRELATION FUNCTIONS

Previous work

A number of statistics have been used previously to quantify the ordering effects induced by diffusional control on nucleation and growth, and thereby distinguish between diffusional and interfacial control on nucleation and growth of porphyroblasts. These include the ordering index, the clustering index, and the impingement index (Kretz, 1974; Carlson, 1989; Denison et al., 1997). Recently, a new class of statistics has been proposed as improvements on these previously used measures of ordering and clustering (Raeburn, 1996; Daniel and Spear, 1999). These correlation functions, which measure the number or sizes of crystals whose centers are separated by a given distance, have the advantage of measuring a given statistic over a range of length scales, in contrast to single-valued statistics, which do not have this type of scale dependency.

The three correlation functions examined here are the *L*-function, the Pair Correlation Function, and the Mark Correlation Function. Ripley (1976) first introduced a *K*-function, which, when normalized, gives

his *L*-function. Other workers have developed derivatives of the *K*-function, which are briefly reviewed in Konig (1991). Those used in this work are the *L*-function, the Pair Correlation Function and the Mark Correlation Function. Each of these functions as used for this work is described in detail below.

Correlation functions were first employed in the spatial statistics literature to describe ordering and clustering of point arrays, and have since been applied principally in the biological and physical sciences. They were used for textural analysis of crystals in metamorphic rocks first by Raeburn (1996), then by Daniel and Spear (1999). These studies inferred interfacial controls on crystallization, in contrast to prior work using other statistical methods that inferred diffusional controls on nucleation and growth in a variety of samples (Carlson, 1989, 1991; Carlson and Denison, 1992; Denison and Carlson, 1997; Denison et al., 1997). The contrast between these results raised the possibility that different statistical approaches might be responsible for differences in inferred mechanisms, although Hirsch and Carlson (1997) used correlation functions to confirm earlier inferences of diffusional control based on single-valued statistics.

It is important to note that statistical measures are not the only method of distinguishing diffusional controls from interfacial controls. Another approach is that of iterated domain calculations (Denison et al., 1997). In this method, diffusional control is assumed, and each crystal is assigned a nucleation time based upon its size. Nucleation and growth of the natural crystal array is simulated, and inconsistencies between the simulation and the natural rock are progressively removed through iteration by adjusting the nucleation times assigned to each crystal. Samples that do not converge towards a solution, or that lead to physically impossible geometries, are deemed to violate the initial assumption of diffusion control. Also, chemical means of discrimination in the form of Kretz's (1974) normalized radius-rate diagrams have also been widely used for zoned garnet (Kretz, 1974; Carlson, 1989; Raeburn, 1996; Denison and Carlson, 1997; Daniel and Spear, 1999). These alternative approaches should be used whenever possible to provide independent tests of conclusions drawn from spatial statistics.

The *L′*-function

The *L′*-function is a slightly modified version of the *L*-function, the value of which is related to the number of crystal centers within a certain distance of each crystal center. The *L′*-function is positive if there are more crystal centers within this distance than would be expected if the crystal centers were Poisson-distributed (spatially random and sparse), and negative if there are fewer. A schematic illustration useful for understanding these functions appears in Figure 1.3.

The basis for the calculation is the *K*-function (Ripley, 1976), which measures the number of crystal centers within a certain distance *r* of each crystal center (Fig. 1.3). The *K*-function, $K(r)$, can be estimated using the quantity $\hat{k}_2(r)$, an unbiased estimator for $\lambda^2 K(r)$, where λ in this discussion is the number of crystals per unit volume (Stoyan and Stoyan, 1994, p. 280). The estimator $\hat{k}_2(r)$ is calculated from

$$\hat{k}_2(r) = \sum_{i=1}^{n} \sum_{\substack{j=1 \\ (j \neq i)}}^{n} \frac{I\left(r, \|\bar{x}_i - \bar{x}_j\|\right)}{V(W)}, \tag{1.1}$$

where *n* is the number of crystals in the sample region *W*, $\bar{x}_i$ is the vector from an arbitrary but consistent origin to the center of crystal *i*, $V(W)$ is the volume of the sample region, *r* is a specified test distance, $\|\bar{x}_i - \bar{x}_j\|$ is merely the distance between crystals *i* and *j*, which we can denote *d*, and $I(r,d)$ is an indicator function that takes the value zero if $d > r$, and the value unity if $d \leq r$. In this and the following presentation of the mathematical basis for the correlation functions, symbols conform to the usage of Stoyan and Stoyan (1994).

The *K*-function has a value of $(4/3)\pi r^3$ for a homogeneous randomly distributed array of crystal centers, a greater value at a given test distance for clustered arrays, and a smaller value for ordered arrays. The reason for this becomes clear when one considers that for a Poisson distribution,

$$\hat{k}_2(r) \approx \frac{n_{total} n_{d \leq r}}{V(W)}, \tag{1.2}$$

and so the *K*-function tends towards

$$K(r) = \frac{\hat{k}_2(r)}{\lambda^2} \approx \frac{n_{total} n_{d \leq r}}{V(W)} \frac{V(W)}{n_{total}} \frac{V_{d \leq r}}{n_{d \leq r}} = V_{d \leq r} = \frac{4\pi r^3}{3}, \tag{1.3}$$

where $n_{d \leq r}$ is the number of crystals within a spherical examination region of radius *r* and $V_{d \leq r}$ is the volume of this spherical region. The approximation is present because we are treating the number of crystals per unit volume, λ, first as $n_{total}/V(W)$ and then as $n_{d \leq r}/V_{d \leq r}$. An equality would imply that the number of crystals per unit volume in any spherical sub-region of radius *r* is identical to the bulk crystal number density, while in real rocks that grow from a uniform precursor, these values are close but not identical. The *K*-function is somewhat unwieldy, so most workers, beginning with Ripley (1976), have used a normalized version, the *L*-function. For analysis in three dimensions, the *L*-function is related to the *K*-function by

$$L(r) = \sqrt[3]{\frac{3K(r)}{4\pi}}, \tag{1.4}$$

making the value of the *L*-function simply *r* for Poisson-distributed (spatially random) arrays. In the present work, there is a further normalization, here denoted *L'* (this normalization was included in the definition of *L(r)* given in Cressie, 1993),

$$L'(r) = L(r) - r, \tag{1.5}$$

performed so that the value of the function will be zero for a Poisson-distributed array.

For crystals that nucleated and grew by an interface-controlled mechanism, one would expect only a small degree of ordering at the smallest length scales, due solely to the "volume effect," the inability to nucleate a new crystal inside the volume of a pre-existing crystal. The volume effect would be expected to cause ordering on scales only up to approximately the mean crystal diameter. For crystals that nucleated and grew under diffusional controls, one would expect significant ordering (negative values of L') at scales over which diffusion was operating, typically up to about half the mean nearest-neighbor distance. Clustering of crystal centers, if present, should be reflected as positive values of the L'-function at the scale of the clustering.

The Pair Correlation Function

The Pair Correlation Function (PCF) is related to the L', L, and K-functions; it also measures the number of crystal centers relative to each crystal center. However, instead of counting centers that lie *within* a certain distance of each crystal, the PCF identifies centers that lie *at or near* a certain distance from each crystal. The mathematical selection of crystals that satisfy this criterion is performed using a kernel function, the bandwidth of which dictates the amount by which the separation of two crystals may differ from the test distance and still allow those crystals to be included in the calculation (Fig. 1.4). The summation is normalized by an appropriate factor such that the PCF will yield a value of unity for a Poisson-distributed array.

The Pair Correlation Function, $g(r)$, is related to the "product density function", $\rho^{(2)}(r)$, by

$$g(r) = \frac{\rho^{(2)}(r)}{\rho^2} \quad (r \geq 0). \tag{1.6}$$

Note that the "2" in $\rho^{(2)}(r)$ is not a power, but signifies the second-order product density. The product density function is essentially the probability that two crystal centers are separated by a distance r. In calculating the PCF, the product density function, $\rho^{(2)}(r)$, is first estimated by the quantity $\hat{\rho}(r)$ and this value is divided by the square of the crystal number density, estimated using

$$\hat{\rho}^2 = \frac{n(n-1)}{[\nu(W)]^2}, \tag{1.7}$$

where n is the number of crystal centers in the sample. This estimator is used in favor of $[n/V(W)]^2$ because this alternative is biased, while equation (1.7) is unbiased (Ripley, 1981, p. 159). The estimator $\hat{}(r)$ is calculated as

$$\hat{}(r) = \sum_{\substack{i=1 \\ }}^{n} \sum_{\substack{j=1 \\ (j \neq i)}}^{n} \frac{e_h\left(r - \|\bar{x}_i - \bar{x}_j\|\right)}{4\pi r^2}, \tag{1.8}$$

in which $e_h(t)$ is the Epanecnikov kernel function of bandwidth h, calculated as

$$e_h(t) = \begin{cases} \dfrac{3}{4h}\left(1 - \dfrac{t^2}{h^2}\right) & |t| \leq h \\ 0 & \text{otherwise} \end{cases}, \tag{1.9}$$

where t is the value of the function to which the kernel is being applied, and h is the bandwidth of the kernel function.

The Epanecnikov kernel function serves both to limit the calculation to those crystals present in a spherical shell around crystal i, and to allow smoothing of the function by including larger numbers of crystals in each calculation. Crystals whose centers lie near the middle of the two-bandwidth shell (*i.e.*, close to the actual test distance) are weighted more heavily than those near the edge of the shell. In the present work, increments of r are chosen so that the shells are overlapped by 50%, or one bandwidth, to allow all crystals to fall within the heavily-weighted region of the calculation for some value of r. Stoyan and Stoyan (1994, p. 285) suggest that the value h for the bandwidth of the kernel function should be $h = c\lambda^{-1/2}$, with c in the range 0.1 - 0.2. In the present work, the value for c has been set to 0.1, out of a desire for detail in the statistics. Larger values of c (and therefore, h) will produce smoother curves; smaller values will produce more irregular curves, because fewer crystals, over a smaller range of test distances, will be used in the calculation (Fig. 1.5).

For an interface-controlled case, one expects a small degree of ordering (PCF < 1) at scales on the order of the mean crystal diameter, due to the volume effect. For a diffusion-controlled case, one expects a significant degree of ordering at the scales over which nucleation is suppressed, roughly half the mean nearest-neighbor distance.

The L'-function and the PCF measure similar aspects of the data, but are differentially sensitive to certain elements of the data. The L'-function counts crystals within a solid sphere centered at each crystal, while the PCF counts those within a spherical shell of fixed thickness (twice the kernel bandwidth h). The L'-function is more sensitive to clustering effects in the data, because when examining a crystal near the center

1-8

of a spherical cluster with a test distance near the cluster radius, the L'-function will count all crystals within the cluster; the PCF will only count those crystals on the edge. This disparity will be increased if the crystal under consideration is offset by at least h from the cluster center, because the L'-function will still count most of the crystals in the cluster, while the PCF will now have half or more of its shell outside the cluster boundary. This effect will be maximized for spherical clusters, but should still apply for layered crystal arrays.

The Mark Correlation Function

The Mark Correlation Function (MCF) is closely related to the PCF, in that it similarly evaluates crystals within a certain bandwidth at a certain distance, but it weights its evaluation by some feature of the crystals, such as radius or volume. The MCF was calculated on selected samples first with crystal radius and then with crystal volume as the mark, and the difference in the MCF was found to be minor. Radius was chosen as the mark for consistency with previous work. Thus, as applied here, the MCF is a measure of the radii of crystals at a given separation. It will be less than unity if the radii of crystals separated by r have a geometric mean smaller than the mean radius of all the crystals in the sample.

It is worth noting one might choose two possible volumes (and therefore, radii) for a crystal that interpenetrates with another. One might imagine a plane separating the two crystals and assign the volume on each side of the plane to each crystal; alternatively, one might fit the best crystal shape (for garnets, we approximate this as a sphere) to each crystal and assign each the corresponding volume. By analogy to the terminology of Avrami (1940), we term the former the "actual volume" and we term the latter the "extended volume" (Carlson, 1989) as it will always be larger than the actual volume. The extended volume represents the size each crystal would have if growing in isolation, discounting diffusional growth-suppression effects. This choice of volumes will also affect the crystal center that is assigned, because that is calculated as the center of mass of the crystal. In the present work, we have chosen always to use the extended volume, as the crystal centers thus identified more closely correspond to the presumed nucleation location. Additionally, as the extended volume is independent of overlap, the crystal size distributions do not change upon rearrangement of locations in the production of null-hypothesis simulations, described below.

Other recent workers in the field have termed the Mark Correlation Function described here, or variations on it, the Mark Covariance Function, terminology that stems from Konig *et al*. (1991). This paper

adheres instead to the terminology of Stoyan and Stoyan (1994), who denote the Mark Correlation Function as $k_f(r)$ and define its estimator as:

$$\hat{k}_f(r) = \frac{\hat{c}_{mm}(r)}{c_{mm}(\infty)}, \quad r \geq 0, \tag{1.10}$$

where $c_{mm}(r)$ is estimated by

$$\hat{c}_{mm}(r) = \frac{\hat{\rho}_{mm}(r)}{\hat{\rho}(r)}. \tag{1.11}$$

In this equation, $\hat{\rho}_{mm}(r)$ is an estimator for the mark product density function and $\hat{\rho}(r)$ is the estimator given above for the product density function. Their ratio can be interpreted as the conditional mean of $m_i m_j$, given that there are two points separated by a distance r (Stoyan and Stoyan, 1994, p. 263). Here, m_i is the radius of the ith crystal. Note that in order to preserve consistency with the definition given by Stoyan and Stoyan (1994), r in equations (1.10) and (1.11) represents not the radius of a crystal, but the test distance. Also, in equation (1.10) the subscript "f" indicates a generalized mark function. In this discussion we use two mark functions: $f=mm$ indicates the product of the marks (which is then normalized to give the geometric mean of the marks); $f=\overline{m}$ indicates the arithmetic mean of the marks. The mark product density function is calculated in a manner similar to the product density function:

$$\hat{\rho}_{mm}(r) = \sum_{\substack{i=1 \\ }}^{n} \sum_{\substack{j=1 \\ (j \neq i)}}^{n} \frac{m_i m_j e_h \left(r - \|\vec{x}_i - \vec{x}_j\|\right)}{4\pi r^2}, \tag{1.12}$$

where m_i is the radius of the ith crystal. Stoyan and Stoyan (1994) also state that

$$c_{mm}(\infty) = \overline{m}^2 \tag{1.13}$$

where $\overline{m}$ is the arithmetic mean radius of all the crystals in the sample.

Because $\hat{\rho}(r)$ and $\hat{\rho}_{mm}(r)$ contain many of the same normalization factors, and the same kernel function, the MCF estimator reduces to:

$$\hat{k}_{mm}(r) = \frac{1}{n(n-1)} \sum_{\substack{i=1 \\ }}^{n} \sum_{\substack{j=1 \\ (j \neq i)}}^{n} \frac{m_i m_j}{\overline{m}^2} \cdot I\left(h, A, b\left(r - \|\vec{x}_i - \vec{x}_j\|\right)\right), \tag{1.14}$$

where the second factor inside the brackets is the same indicator function as in Equation (1.1), which serves simply to exclude crystals whose centers do not lie inside the bandwidth region.

The MCF does not measure departures from spatially random distributions of crystal centers (ordering and clustering) as do the L'-function and the PCF; instead it is sensitive to localized variations in crystal size, and thus relative growth. For an interface-controlled case, one expects at the smallest scales to have a slight reduction in the MCF value (MCF < 1) by virtue of the fact that at a given test distance r, it is unlikely to

have a crystal in the calculation whose radius is greater than *r*, for that would require one crystal to be located inside another. (Specific criteria for the maximum overlap of crystals in an interface-controlled sample are discussed below.) For the diffusion-controlled case, however, one would expect significant suppression of growth for closely spaced crystals due to competition for nutrients, giving a value for the MCF significantly below unity at those scales over which diffusion is retarding growth, again roughly half the mean nearest-neighbor distance.

The MCF as described above has a small inherent bias towards values less than unity, because for each summand it in effect compares the pairwise geometric mean radius $[(m_i m_j)^{1/2}]$ to the arithmetic mean radius $[0.5*(m_i + m_j)]$ for the sample. The geometric mean for a set of positive numbers is always less than or equal to the arithmetic mean, so in the average, the summands for the MCF will be smaller than unity. This can be illustrated with a rock made up of three crystals, whose radii are 3, 10, and 50 units. If the MCF shown above is calculated using all the crystals in any rock (i.e., they are all separated by the test distance *r*), the expected unbiased value is unity. However, doing the actual calculation, we find that:

$$\hat{k}_{mm}(r) = 3^{-1}2^{-1}441^{-1}(30 + 150 + 30 + 500 + 150 + 500) = 0.514. \tag{1.15}$$

This bias toward values less than unity is magnified with small numbers of crystals that have a large variance (as in this example); in less extreme cases, it will not strongly skew the results. However, in light of this bias, the following variant of the Mark Correlation Function is proposed, in which the arithmetic mean of each pair of crystals is substituted for the geometric mean:

$$\hat{k}_{\bar{m}}(r) = \frac{1}{n(n-1)} \sum_{\substack{i=1 \\ }}^{n} \sum_{\substack{j=1 \\ (j \neq i)}}^{n} \frac{m_i + m_j}{2\bar{m}} \ I\left(h, Abs\left(r - \|\bar{x}_i - \bar{x}_j\|\right)\right) \tag{1.16}$$

For the above example, this gives:

$$\hat{k}_{\bar{m}}(r) = 3^{-1}2^{-1}42^{-1}(13+53+13+60+53+60) = 1.0. \tag{1.17}$$

In tests that we have performed, this proposed variant of the MCF shows the same qualitative patterns as $\hat{k}_{mm}(r)$, and gives the expected results on simulations. Previous workers were led to prefer the geometric mean because the bias is small for most sets of data, and excursions from Poisson distributions are more easily recognized using the geometric mean. The proposed variant is therefore a more conservative approach, less prone to provide spurious indications of growth suppression. Throughout this article, we employ this variant based on the arithmetic mean.

Consistency with previous work

Raeburn (1996) and Daniel and Spear (1999) use somewhat different definitions for these correlation functions, drawn from Konig (1991). In the present work, we have carefully followed the nomenclature and definitions given in Stoyan and Stoyan (1994). Some differences are merely semantic (e.g., others have used the term "Mark Covariance Function," which is not found in Stoyan and Stoyan, 1994), but there is one substantive difference in the function definitions, which will affect the value obtained from the Pair Correlation Function.

In Raeburn (1996) and Daniel and Spear (1999), the Konig (1991) definition for the PCF is given:

$$\hat{g}^{(2)} = \sum_{i=1}^{n} \sum_{\substack{j=1 \\ j \neq i}}^{n} \frac{\mathbf{k}_h\left(r - \|p_i - p_j\|\right)}{4\pi \left(\|p_i - p_j\|\right)^2 \, \mathrm{Vol}\left\{W_{p_i} \cap W_{p_j}\right\}}. \tag{1.18}$$

In this equation, $\mathbf{k}_h(r)$ is the Epanecnikov kernel function of bandwidth h (denoted as $\mathbf{e}_h(r)$ in the present work), the Vol{} term represents the translation edge-correction method detailed below, r is the test distance, and $\|p_i - p_j\|$ is the distance between crystals i and j. This is in contrast with the definition from Stoyan and Stoyan (1994) given above, adding the same edge correction term:

$$\hat{g}(r) = \sum_{i=1}^{n} \sum_{\substack{j=1 \\ (j \neq i)}}^{n} \frac{\mathbf{e}_h\left(r - \|\bar{x}_i - \bar{x}_j\|\right)}{4\pi \, r^2 \, \mathrm{Vol}\left\{W_{\bar{x}_i} \cap W_{\bar{x}_j}\right\}}. \tag{1.19}$$

Comparing these equations, the difference is clear: while the Stoyan and Stoyan (1994) version uses the test distance in the denominator, the Raeburn (1996) version (also used by Daniel and Spear, 1999) substitutes in its place the distance between the two crystals under consideration. A number of comparison runs were performed to evaluate the effects of this difference, and the results of the analysis of a nearly completely random simulation are shown in Figure 1.6. The results show that the Raeburn version will tend to underestimate values for the PCF at small scales, but, because it similarly underestimates the PCF values for the interface-controlled envelope runs, the compensating errors will tend to leave the ultimate conclusions unchanged.

Edge effects

Each of these statistics can be adversely affected when the examination region (a sphere for the L'-function, a spherical shell for the PCF and MCF) intersects the sample boundary. The statistics therefore must be modified to account for these edge effects. Two methods are generally used for this: minus sampling, and window translation.

Minus-sampling method. Minus sampling prohibits calculation for any crystal for which the examination region would intersect the sample boundary (Stoyan and Stoyan, 1994, p. 280). This method can be conceptualized as installing a guard region inside the sample boundary whose thickness is that of the current test distance (Fig. 1.7). Crystals within this region will not have the examination region centered on them, but may still be counted if they fall within the examination region centered on another crystal not within the guard region. This method has the advantage of introducing the fewest artifacts into the calculation, but requires a large number of crystals, because many are excluded from the calculation, even at small test distances. Additionally, there is a maximum test distance allowable with this method, although in most cases of present interest, this maximum is greater than the typical test distances of interest for the statistic.

Translation method. The translation method attempts to correct each summand for those crystals missed outside the sample boundary. It divides the summand for each pair of crystals by a factor, $V(W_{Xi} \cap W_{Xj})$, that is the volume of the intersection of the sample boundary offset to two different points: first so that the origin is located at the center of crystal x_i, then so that the origin is located at the center of crystal x_j (Fig. 1.8a). This is equivalent to the volume of intersection of the sample boundary with a copy offset by the vector from x_i to x_j (Fig. 1.8b). Dividing each summand in this way causes the summand to increase for crystals that are more widely separated, which tends to compensate for the fraction of the examination region that lies outside the sample boundary. However, because the method does not take into account the degree to which the examination region *actually* lies outside the sample boundary for any particular pair, it is possible in concept for the method to introduce artifacts into the statistics. Nevertheless, as is shown below, the translation method of edge correction produced values very close to those from the minus-sampling method on a suite of crystal simulations, with the advantage of retaining larger numbers of crystals in the analysis.

PREVIOUSLY USED STATISTICS

Previously used statistical measures of ordering and clustering are described in Denison *et al.* (1997) and include the ordering index, clustering index and impingement index. The ordering index is derived from the nearest-neighbor test, which evaluates the mean distance to the nearest neighbor of each crystal; discounting volume effects, this index will be greater than unity for an ordered distribution and less than unity for a clustered distribution. The clustering index is derived from the random-point test, which evaluates the mean distance to the nearest crystal center from a random point in the sample; discounting volume effects,

this index will be greater than unity for a clustered distribution and less than unity for an ordered distribution. The impingement index is derived from a test that compares the overlap between spherically idealized crystal shapes and the amount of overlap expected in a random distribution; this index will be greater than unity for a clustered distribution and less than unity for an ordered distribution. All three statistics should have a value of unity for a perfectly random distribution of crystal centers. However, these statistics can be altered in complicated ways when applied to arrays of crystals, reflecting complexities introduced by combinations of clustering and ordering effects, volume fraction, and crystal number density, as discussed in Denison *et al*. (1997, p. 38, Fig. 8).

These complexities introduce considerable ambiguity because they can alter the predicted value of each statistic for a given distribution. This makes deductions as to ordering, randomness or clustering (and therefore interfacial or diffusional controls on nucleation and growth) uncertain for any particular value of a given statistic. To reach meaningful conclusions, it has been necessary to consider together all three indices, in combination with numerical simulations of crystallization that produce equivalent textures from known mechanisms.

To ameliorate this ambiguity, in the present work the value of each statistic is calculated for a large number of "envelope" simulations (described in detail below), and the mean and 95% confidence interval for each statistic is calculated. If the value of the statistic measured on the rock falls outside the confidence interval, then one must reject the randomness hypothesis in favor of either ordering or clustering. This idea is discussed in greater depth below.

EVALUATION OF CORRELATION FUNCTIONS

It is important when evaluating the utility of a statistical measure to examine its performance on simulations for which the expected value or behavior of the statistic is known. Furthermore, any specific computational implementation should be tested on simulations to prove its ability to produce the correct answers in controlled cases. Here we report such tests on two types of simulations: one type for which the expected results are better constrained, but of less geological relevance, and another type of greater geological relevance, but for which the expected results are less well constrained.

The first type of simulation is an idealization, produced not by modeling crystallization processes, but merely by placing crystals in specific locations, with the restriction that they may not overlap by more than a specific small amount. This allows processing of point arrays whose degrees of ordering and clustering are

known. The overlap restriction is designed to broadly mimic restrictions on crystal locations in a rock, although the overlap criterion is somewhat more complex for interface-controlled growth (discussed below) and still more involved for diffusion-controlled growth. The second type is an actual numerical simulation of nucleation and growth of porphyroblasts in a rock, given a specific temperature-time history, and specific rate laws for nucleation and diffusion.

Diagrams

Each data figure in this paper is made up of four diagrams: the L'-function, our proposed variant of the MCF (both calculated using the translation method of edge correction), the PCF calculated using the translation method of edge correction, and the PCF calculated using the minus-sampling method of edge correction. In each case, the horizontal axes represent the test distance, with the lower horizontal axis scaled to the mean radius of the crystals in the sample, and with the upper horizontal axis scaled to the test distance in centimeters; the vertical axis is the value of the statistic. These statistics have differing units, which are generally not included in the literature, as the units have no physical meaning; this convention will be followed here. Each diagram has a data curve (represented by a solid line and point markers) that is plotted along with a pink "envelope." The meaning of the envelope is discussed below, and the method of its calculation is given in Appendix 1A. Each diagram also shows a horizontal line that represents the value expected for a Poisson distribution of points (zero for the L'-function, unity for the other three). Finally, each diagram has a light blue vertical bar that indicates the range of nearest-neighbor distances for the sample – the center represents the mean, and the width of the bar represents one standard deviation on either side of the mean.

The range of test distances is calibrated to the sample under consideration; in all diagrams the maximum test distance is approximately 6 times the mean nearest-neighbor distance. This is intended to provide rapid calculation times by limiting the number of test distances required, while ensuring that the data points include the range of separations over which differing crystallization mechanisms are likely to produce discernable effects.

Many data figures are accompanied by three-dimensional renderings of the crystal array in whole or in part from which the data were obtained. These can be clicked to display an interactive 3-D representation using QuickTime for Macintosh or Windows.

Envelope simulations

Each of the various statistical measures mentioned above has a theoretically derived expected value for certain types of point arrays, such as a Poisson distribution. For point-type sample data, one can simply compare the value of the statistic to the expected value to discern trends towards ordering or clustering. However, crystal arrays do not have theoretically derived expected values, because crystals cannot nucleate and grow completely randomly – no crystal may nucleate within another crystal. Expected values of the statistics must accommodate geologically reasonable restrictions on the relative locations of crystal centers, and these restrictions must take into account such factors as nucleation times, growth rates, and the like.

In order to draw conclusions about ordering and clustering trends within a sample data set, we must therefore produce a crystal array that lacks such trends to which we can then compare the sample data set. In order to properly make the comparison, the crystal array should share as many features as possible with the sample data set, aside from the small-scale ordering features that are under examination. The number density of crystals, the size and shape of the sample volume, and the crystal size distribution should be identical in order to maximize confidence in the conclusions drawn from the comparison. Our analysis, presented below, reveals that very great care is required in order to obtain a crystal array to which the sample data can be rigorously compared (cf. Appendix 1A); previously published attempts at this (Raeburn, 1996; Daniel and Spear, 1999) appear to overlook features that may affect the comparison.

Once a correct crystal array lacking ordering and clustering trends is produced, this array becomes a null-hypothesis case of interface-controlled non-clustered nucleation and growth; if the value of the statistic measured on the sample data set deviates significantly from that measured on the array, then a deviation from the null hypothesis case has been demonstrated. But what constitutes a significant deviation? To answer this question, the Monte Carlo method is used: a large number of null-hypothesis arrays are manufactured, and each statistic is measured on each array. For each statistic, there is a distribution of null-hypothesis values, and one can determine if the sample data falls within a certain distance of the mean of those values. If they do not, one may justifiably conclude, with a corresponding confidence level, that the sample is significantly ordered or clustered relative to a non-clustered interface-controlled case. This is the conceptual basis for our analysis; the details of the production of null-hypothesis, or "envelope" simulations, are given in Appendix 1A.

The shaded regions on the diagrams presented below represent the 2- range or envelope for a set of 100 simulations. If the value of a statistic falls outside the 2- envelope, it can be concluded with 95% confidence that the statistic measures significant ordering or clustering relative to non-clustered interface-controlled nucleation and growth. However, if the values fall within the envelope, then no conclusion can be reached. If it were possible to create a diffusion-controlled envelope for each rock, then one could use that as a second null hypothesis, and test it in order to positively identify interfacial controls on nucleation and growth for data that fell outside that envelope. One published work (Daniel and Spear, 1999) includes an attempt at this, but, as discussed below, the simple simulation of diffusion-controlled nucleation and growth used in the production of the null-hypothesis envelope simulations fails to replicate many of the vital characteristics of the process, and is therefore suspect (cf. Appendix 1A). One key feature of diffusion-controlled nucleation and growth that the model in Daniel and Spear (1999) fails to replicate is the difference in diffusional domain sizes between crystals of the same size that nucleated at different times and whose diffusional domains impinge upon others at different stages in their growth. In fact, we found in this work that the production of rigorously defensible diffusion-controlled null-hypothesis envelope regions is computationally prohibitive at present.

It is important to note that geologic reasoning must govern the inferences drawn from these data. For example, trends that fall below the null-hypothesis region can only be considered diffusional at scales over which diffusion operates, up to about the mean nearest-neighbor distance. Trends that fall below the null-hypothesis region at scales greater than this must be due to some other cause: for example, the relative sparsity of crystals at scales greater than that of a cluster or layer.

Artificial arrangements of crystals

In order to understand the behavior of correlation functions, a number of simulations were produced and analyzed. The first type of simulation is a completely artificial array of crystal sizes and locations. These crystal arrays exhibited extreme tendencies towards ordering, spatial randomness, or combinations of clustering with ordering or randomness. They are fully detailed in Appendix 1B, and reveal patterns closely matching predictions based upon characteristics of the crystal arrays. Analysis of these simulations leads to two important results. On one hand, the statistics are quite robust in their ability to detect ordering that has been disturbed by random permutations. On the other hand, clustering of crystals can strongly obscure indicators of small-scale ordering that might be diagnostic of diffusion-controlled growth. The L' -function

and PCF are more susceptible to degradation of the diffusional signal than is the MCF, but as the scale of clustering effects approaches the scale of diffusional effects (roughly half the mean nearest-neighbor distance), all of these functions lose their ability to extract an underlying diffusional ordering signal from a clustered array of crystals.

Simulations of nucleation and growth

The second type of simulation is more sophisticated and is produced by numerical modeling of a nucleation-and-growth process, with time as an explicit variable (Carlson et al., 1995). A number of these types of simulations have been produced and analyzed. Four are described below: each is either interface-controlled or diffusion-controlled, with or without layering effects induced by a spatially sinusoidal probability of nucleation in one dimension with uniform nucleation probability in the other two dimensions, or clustering effects induced by spatially sinusoidal probability of nucleation in three dimensions.

Interface-controlled, uniform distribution. The interface-controlled case is the default distribution, and this was analyzed to ensure that the statistics can reproduce the expected values. An interface-controlled simulation was produced that includes an exponential increase in the rate of nucleation with time. There are 1739 crystals in a 1-cm^3 cube. As expected, the values for the correlation functions all fall within the interface-controlled envelope (Fig. 1.9).

Interface-controlled with layers. An interface-controlled simulation similar to that shown in Figure 1.9 was produced, except with layering on a scale of 0.5 cm. This would correspond to interface-controlled nucleation and growth in a layered sample. The simulation has three distinct layers in a 1-cm^3 cube. The results are shown in Figure 1.10 with a rendering of a sub-volume. As expected, the data show clustering up to about 10 mean radii (~0.2 cm), and fall below the envelope at greater length scales, reflecting the relative sparsity of crystals beyond the scale of layering. There is no evidence of growth suppression in the MCF data.

Interface-controlled with clustering. A more complex interface-controlled simulation was also produced (Fig. 1.11), except with clustering on a scale of about 1 cm. The clustering is achieved by imposing a sinusoidal probability of nucleation in three dimensions. The data show the effects of clustering in the L'-function and the PCF, almost completely obscuring the interface-controlled signature. However, the MCF shows the sample data fall within the null hypothesis region, as expected from the clustering algorithm, which only varies nucleation probability, and not growth rates.

Diffusion-controlled, uniform distribution. Previous work has shown regional-metamorphic samples from a range of rock types and localities to have grown in diffusion-controlled nucleation and growth environments (Carlson, 1989, 1991; Carlson and Denison, 1992; Carlson et al., 1995; Denison and Carlson, 1997). In order to demonstrate that the statistics give the correct results in such circumstances, a diffusion-controlled simulation was produced that includes an exponential increase in nucleation with time, together with diffusional suppression of nucleation and growth, using the simulation model of Carlson *et al*. (1995). The volume fraction of porphyroblasts is 0.1, and there are 1919 crystals in a 1-cm^3 cube. The results for this simulation are shown in Figure 1.12. As expected, at scales up to about the mean nearest-neighbor distance, the values for the correlation functions fall below the interface-controlled envelope. The MCF shows suppression of growth up to about twice the mean nearest-neighbor separation. The larger scale of growth suppression is consistent with expectation, because a crystal's growth is inhibited not only by its nearest neighbor (as is the case with its nucleation) but also by more distant neighbors with which its diffusional domain impinges over the course of its growth.

  Diffusion-controlled with layers. If the sample analyzed above were layered, as might be common for metasedimentary rocks, then the statistics should reveal ordering within clustering. In order to test this, a diffusion-controlled simulation was produced that includes an exponential increase in nucleation with time, together with diffusional suppression of nucleation and growth. The volume fraction of porphyroblast material is 0.1, and there are 3059 crystals in a 1-cm^3 cube. The model parameters are the same as the diffusion-controlled simulation above, save for an increased nucleation rate, an extended period of heating and a sinusoidal distribution of nucleation probability in which the sine curve has a wavelength of 0.33, producing three layers in the sample. The results for this simulation are given in Figure 1.13, together with a rendering of a sub-volume. The data show ordering at small scales, up to about the mean nearest-neighbor distance. Ordering is also present at scales greater than 0.15 cm or 0.20 cm, reflecting the periodicity of the layering (crystals are sparse at $x = 0$, $x = 0.5$, and $x = 1.0$, so the mean distance to a sparse region is about 0.18 cm). The MCF results for this simulation should be regarded skeptically, because the nature of the simulated layering is not geologically reasonable: it only involves an inhomogeneous distribution of nucleation sites, not nutrients, leading to abnormally large crystals at the border between the dense and sparse layers, as is evident from Figure 1.13a.

Tests of robustness of correlation functions

Denison *et al.* (1997, Appendix 1) described limitations on sample characteristics for three single-valued statistics: the ordering index, clustering index, and impingement index. They conclude that because of edge effects, a minimum of 1000 crystals is necessary to obtain reliable values for these statistics. A similar set of analyses was performed to evaluate appropriate sample sizes for application of correlation-function statistics. These results are described in Appendix 1C, and demonstrate that correlation functions are significantly more robust that single-valued statistics. The tests suggest that correlation functions may produce reliable results from data sets as small as a few hundred crystals, although greater numbers will greatly strengthen the confidence that can be placed in the inferences drawn.

APPLICATION TO NATURAL SAMPLES

Denison and Carlson (1997) raised the problem that the three single-valued statistics used by them are all interdependent, and so a single numerical boundary for each that would separate diffusional from interfacial control in a sample does not exist. To address this issue, correlation functions were used to reanalyze the rocks studied by Denison and Carlson (1997), comprising seven samples from three localities, representing a range of rock types and metamorphism-deformation relationships. The previously used statistics were also calculated for the samples and their interface-controlled envelopes. These samples are presented as an application for the correlation functions, and therefore are not described in detail here; for detailed descriptions, see Denison and Carlson (1997, p. 46).

Picuris Mountains suite

Two samples (PM1, PM2) from the Picuris Mountains of north-central New Mexico were re-analyzed, together with the diffusion- and interface-controlled simulations that were designed to model the crystallization of each sample. The rock samples and simulation parameters are described in detail in Denison and Carlson (1997). These samples are garnetiferous quartzites in which garnet growth was post-kinematic. Sample PM2 was originally scanned simultaneously with two other samples, resulting in only a small usable analysis volume (1772 crystals in 13.8 cm^3, with a large aspect ratio).

The data for Sample PM1 are shown in Figure 1.14. The data show excursions below the interface-controlled 2- envelope up to scales on the order of the mean nearest-neighbor distance for the L'-function and PCF, and up to about twice that distance for the MCF. This is to be expected, and is in good agreement with the conclusions from the single-valued statistics.

The results for the single-valued statistics were obtained in Denison and Carlson (1997), and are given in Table 1.1, together with the 2- bounds from the envelope simulations. This comparison confirms the results previously obtained with these statistics, in that the rock data, with only one exception, show either ordering or clustering. The time-explicit interface-controlled nucleation and growth simulations tend to fall between the 2- null-hypothesis values, but because many of these simulations incorporate explicit spatially varying probabilities for nucleation, they should not be expected to fall between the 2- values, just as the similar interface-controlled simulation of Figure 1.11 falls outside the envelope. Significantly, the values of the indices may fall on either the ordering or clustering side of the envelope, just as in Figure 1.11, the data fall above or below the envelope at different scales. The diffusion-controlled time-explicit nucleation and growth simulations, with only three exceptions, fall outside the null-hypothesis bounds. However, because these simulations generally incorporate explicit clustering of nucleation sites that are not shared by the null-hypothesis simulations, we can in a strict sense have no expectation as to whether the single-valued statistics will fall within, above, or below, the null-hypothesis range.

The data for sample PM2 are shown in Figure 1.15. They differ from sample PM1 in that the excursions below the interface-controlled envelope are not as pronounced for the location-based statistics, although the MCF still shows a strong growth-suppression signal. This confirms the diffusion-controlled conclusion, and suggests that diffusional control was operating during the crystallization of PM2, but that clustering of nucleation sites (probably due to inhomogeneities in the precursor) tends to obscure the ordering signal.

Mica Dam sample

Sample MD is from a locality near the dam along Mica Creek in British Columbia. It is a pelite in which garnet growth was syn-kinematic; it is also compositionally heterogeneous and has kyanite porphyroblasts in addition to the garnet. Functional values for sample MD are shown in Figure 1.16. The functions indicate diffusional control at scales up to about the mean nearest-neighbor distance, although the signal is again weak.

The data for this sample illustrate the different sensitivities of the MCF and the other correlation functions: the L'-function and the PCF show that the ordering of nucleation sites is barely discernable, presumably due to clustering of these sites as a result of initial inhomogeneities in the precursor. In contrast,

the MCF shows a strong signal below the envelope values, indicating significant suppression of growth as a result of diffusional competition for nutrients.

Whitt Ranch suite

A suite of four samples (WR1, WR2, WR3, WR4) from the Whitt Ranch near Babyhead in central Texas was also reanalyzed. These samples are of mafic composition and appear nearly homogeneous at hand-sample scale. In these rocks, the garnets are thought to have crystallized syn-kinematically, but in structural settings with limited penetrative deformation.

The data for samples WR1-WR4 are shown in Figures 1.17-1.20. All show diffusional suppression of nucleation at scales up to about the mean nearest-neighbor distance, and diffusional suppression of growth to about twice that distance. Samples WR3 and WR4 also show significant clustering at scales greater than about one mean nearest-neighbor distance.

CONCLUSIONS

Building upon prior work (Raeburn, 1996; Daniel and Spear, 1999), the analysis presented here identifies several improvements to methods that employ correlation functions for textural analysis. A corrected formulation of the Pair Correlation Function is presented in Equation (1.19). An unbiased Mark Correlation Function is presented in Equation (1.16), which provides a more conservative assessment of the significance of size-isolation correlations. These spatial correlation functions are seen to exhibit a range of comprehensible behaviors when applied to artificial crystal arrays, knowledge of which increases our ability to properly interpret features that arise when the functions are applied to natural samples. We advocate careful testing of any particular calculation scheme for these functions against a series of crystal arrays with predetermined textural characteristics, both artificial arrays that yield known outcomes and arrays produced by numerical simulations of crystallization processes. In particular, our results highlight the importance of constructing null-hypothesis envelopes with great rigor, as emphasized by: (a) the possibility of spurious indications of diffusional control when observability criteria are ignored (Fig. 1A.1); and (b) the failure of previous attempts at constructing diffusion-controlled null-hypothesis envelopes to encompass the characteristics of crystal arrays produced by numerical simulation of diffusion-controlled crystallization (Fig. 1A.2). While not disproving earlier analyses that omitted these refinements, these results suggest that data sets from earlier studies should be re-analyzed to include these improvements in technique.

When properly and carefully applied, correlation functions are a powerful adjunct to other statistical measures and methods of textural analysis. For analysis of small numbers of crystals and samples of high aspect ratio, they have the advantage of being more robust than the single-valued statistics used previously. They also have the ability in some cases to elucidate superposed ordering and clustering effects at different scales in a single sample. It is important to note, however, that even when these functions are used, clustering may obscure the underlying mechanistic signal. As this signal may be either ordered or random, clustered arrays may originate under either interfacial or diffusional control, and in such arrays the textural evidence that allows discrimination between the two possibilities may be obscured. For this reason, spatial correlation functions should be used in conjunction with other statistical measures, with chemical analysis of growth zoning, if preserved, and with models of nucleation and growth processes to discern the underlying controls on the crystallization of metamorphic porphyroblasts.

The results derived from this study corroborate those of Denison and Carlson (1997), who used single-valued statistics along with radius-rate data and diffusional-domain analysis to demonstrate diffusional control in a range of samples. Our careful use of correlation functions confirms their findings; this consistency highlights the utility and reliability of both types of statistics, and the agreement of inferences from both methods emphasizes the geological conclusion reached earlier – diffusional processes were the controlling factors in the nucleation and growth of the garnet porphyroblasts in these rocks. This finding suggests that prior identifications of interface-controlled crystallization (Raeburn, 1996; Daniel and Spear, 1999) or diffusion-controlled crystallization (Carlson, 1989, 1991; Carlson and Denison, 1992; Denison and Carlson, 1997; Denison et al., 1997) are not artifacts of the statistical methods used, but instead reveal genuine differences in environmental variables that control crystallization mechanisms for garnet.

ACKNOWLEDGEMENTS

REFERENCES CITED

Avrami, M., 1940. Kinetics of phase change. II: Transformation-time relations for random distribution of nuclei. *Journal of Chemical Physics*, **8**, 212-224.

Carlson, W. D., 1991. Competitive diffusion-controlled growth of porphyroblasts. *Mineralogical Magazine*, **55**, 317-330.

Carlson, W. D., 1989. The significance of intergranular diffusion to the mechanisms and kinetics of porphyroblast crystallization. *Contributions to Mineralogy and Petrology*, **103**, 1-24.

Carlson, W. D. and Denison, C., 1992. Mechanisms of porphyroblast crystallization: Results from high-resolution computed X-ray tomography. *Science*, **257**, 1236-1239.

Carlson, W. D., Denison, C. and Ketcham, R. A., 1995. Controls on the nucleation and growth of porphyroblasts; kinetics from natural textures and numerical models. *Geological Journal*, **30**, 207-225.

Carmichael, D. M., 1969. On the mechanism of prograde metamorphic reactions in quartz-bearing pelitic rocks. *Contributions to Mineralogy and Petrology*, **20**, 244-267.

Cressie, N. A. C., 1993. *Statistics for spatial data*. J. Wiley, New York, Pages.

Daniel, C. G. and Spear, F. S., 1999. The clustered nucleation and growth processes of garnet in regional metamorphic rocks from north-west Connecticut, USA. *Journal of Metamorphic Geology*, **17**, 503-520.

Denison, C. and Carlson, W. D., 1997. Three-dimensional quantitative textural analysis of metamorphic rocks using high-resolution computed X-ray tomography. Part II: Application to natural samples. *Journal of Metamorphic Geology*, **15**, 45-57.

Denison, C., Carlson, W. D. and Ketcham, R. A., 1997. Three-dimensional quantitative textural analysis of metamorphic rocks using high-resolution computed X-ray tomography. Part I: Methods and techniques. *Journal of Metamorphic Geology*, **15**, 29-44.

Fisher, G. W., 1978. Rate laws in metamorphism. *Geochimica et Cosmochimica Acta*, **42**, 1035-1050.

Hirsch, D. M. and Carlson, W. D., 1997. Correlation functions support diffusion-controlled garnet crystallization in a range of regional metamorphic samples. *GSA Abstracts with Programs*, **29**, A-338.

Joesten, R. L., 1991. Kinetics of coarsening and diffusion-controlled mineral growth. *Reviews in Mineralogy*, **26**, 507-582.

Kerrick, D. M., Lasaga, A. C. and Raeburn, S. P., 1991. Kinetics of heterogeneous reactions. *Reviews in Mineralogy*, **26**, 583-671.

Konig, D., Carvajal-Gonzalez, S., Downs, A. M., Vassy, J. and Rigaut, J. P., 1991. Modeling and analysis of 3-D arrangements of particles by point processes with examples of application to biological data obtained by confocal scanning light microscopy. *Journal of Microscopy*, **161**, 405-433.

Kretz, R., 1994. *Metamorphic crystallization*. J. Wiley, Chichester, Sussex, England; New York, Pages.

Kretz, R., 1974. Some models for the rate of crystallization of garnet in metamorphic rocks. *Lithos*, **7**, 123-131.

Kretz, R., 1973. Kinetics of the crystallization of garnet at two localities near Yellowknife. *Canadian Mineralogist*, **12**, 1-20.

Raeburn, S. P., 1996. New methods in quantitative metamorphic petrology. *Unpub. Ph.D. Thesis, Pennsylvania State University.*

Ridley, J. and Thompson, A. B., 1986. The role of mineral kinetics in the development of metamorphic microtextures. In: *Fluid-rock interactions during metamorphism* (eds Walther, J. V., Wood, B. J. and Saxena, S. K.), pp. 154-193, Springer-Verlag, New York.

Ripley, B. D., 1981. *Spatial statistics*. Wiley, New York, Pages.

Ripley, B. D., 1976. The second-order analysis of stationary point processes. *Journal of Applied Probability*, **13**, 255-266.

Rubie, D. C., 1998. Disequilibrium during metamorphism; the role of nucleation kinetics. In: *What drives metamorphism and metamorphic relations?* (eds Treloar, P. J. and O'Brien, P. J.), pp. 199-214, Geological Society, London.

Rubie, D. C. and Thompson, A. B., 1985. Kinetics of metamorphic reactions at elevated temperatures and pressures; an appraisal of available experimental data. In: *Metamorphic reactions; kinetics, textures, and deformation* (eds Thompson, A. B. and Rubie, D. C.), pp. 27-79, Springer-Verlag, New York.

Spry, A., 1969. *Metamorphic textures*. Pergamon Press, Oxford, Pages.

Stoyan, D. and Stoyan, H., 1994. *Fractals, random shapes, and point fields: methods of geometrical statistics*. Wiley, Chichester; New York, Pages.

Walther, J. V. and Wood, B. J., 1984. Rate and mechanism in prograde metamorphism. *Contributions to Mineralogy and Petrology*, **88**, 246-259.

TABLE 1.1. SINGLE-VALUED STATISTICS FOR SAMPLES AND SIMULATIONS

Single-valued statistical indices for studied samples and corresponding diffusion- and interface-controlled simulations, together with 2- confidence regions for 100 interface-controlled null-hypothesis runs, and conclusion of significant deviation from null-hypothesis (interfacial control). Values that exceed the 2- envelope bounds are ordered for the ordering and clustering indices, and clustered for the impingement index. Values that fall below the 2- envelope bounds are clustered for the ordering and clustering indices, and ordered for the impingement index. The values given here differ slightly from those in Denison and Carlson (1997) because these represent re-analysis using a sample sub-volume in the shape of a rectangular prism, in contrast to the convex hull used previously to make up the sample bounding box.

	Ordering Index				Clustering Index				Impingement Index			
		2- Env.				2- Env.				2- Env.		
Rock/Sim	Value	Min	Max	Result	Value	Min	Max	Result	Value	Min	Max	Result
PM1	1.25	1.07	1.09	O[1]	0.94	0.98	1.04	O	0.82	0.93	0.95	O
DC Sim.	1.13	1.05	1.10	O	1.10	0.99	1.08	C	0.90	0.75	0.75	C
IC Sim.	1.13	1.02	1.04	O	1.01	1.00	1.09		0.99	0.98	1.03	
PM2	1.06	0.98	1.02	O	1.14	1.05	1.14	C	0.97	0.98	0.99	O
DC Sim.	0.95	0.99	1.06	C	1.80	1.05	1.19	C	0.94	0.87	0.87	C
IC Sim.	0.99	0.98	1.03		1.80	1.04	1.15	C	1.09	0.98	1.02	C
WR1	1.12	1.00	1.05	O	1.03	1.04	1.17	O	0.90	0.95	0.98	O
DC Sim.	1.11	1.00	1.07	O	1.16	1.05	1.21		0.92	0.86	0.86	C
IC Sim.	1.00	1.01	1.04	C	1.25	1.01	1.08	C	1.04	0.98	1.02	C
WR2	1.24	1.06	1.09	O	0.91	0.97	1.03	O	0.79	0.92	0.94	O
DC Sim.	1.16	1.01	1.10	O	1.00	1.02	1.19	O	0.87	0.75	0.77	C
IC Sim.	1.03	1.03	1.05		1.01	0.99	1.04		0.99	0.97	1.01	
WR3	1.24	1.04	1.06	O	0.91	1.00	1.06	O	0.87	0.95	0.96	O
DC Sim.	1.15	1.03	1.07	O	1.00	0.99	1.06		0.91	0.85	0.85	C
IC Sim.	1.03	1.02	1.04		1.01	0.99	1.05		1.00	0.98	1.01	
WR4	1.21	1.04	1.05	O	0.99	0.99	1.05	O	0.87	0.95	0.96	O
DC Sim.	1.06	1.01	1.05	O	0.85	1.01	1.10	O	0.94	0.88	0.88	C
IC Sim.	1.02	1.01	1.03		1.02	1.00	1.04		0.99	0.98	1.00	
MD	1.03	0.91	1.01	O	1.21	1.06	1.33		0.96	0.98	1.00	O
DC Sim.	1.04	0.92	1.02	O	1.30	1.09	1.31		0.97	0.96	0.96	C
IC Sim.	1.01	0.96	1.01	O	1.22	1.07	1.22	C	0.99	0.98	1.02	

[1]O = ordered, C = clustered
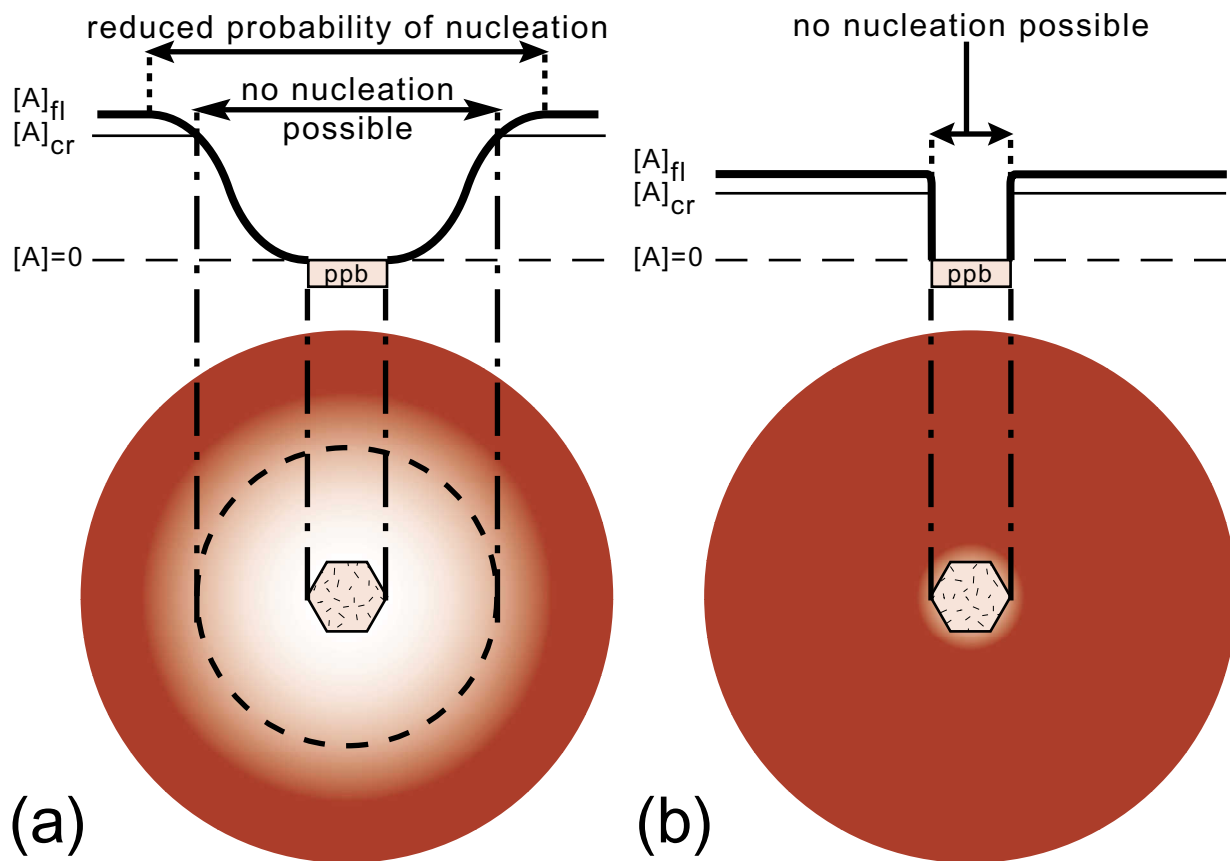
Figure 1.1. Schematic 2-D illustration of diffusion-controlled suppression of nucleation in the vicinity of a growing porphyroblast ("ppb"), after Carlson (1989). (a) If diffusion is sluggish relative to interfacial reaction, then near a growing porphyroblast slow diffusion produces gradients in the chemical affinity for the crystallization reaction in the intergranular fluid $[A]_{fl}$. This results in zones of zero probability of nucleation where the intergranular chemical affinity is less than the critical value required to overcome the activation energy for nucleation $[A]_{cr}$. These zones are surrounded by zones of reduced probability of nucleation where the chemical affinity is less than the value in regions unaffected by diffusion, but greater than the critical value. (b) If diffusion is rapid, then the only significant effect is the prevention of nucleation within the volume of a pre-existing porphyroblast.
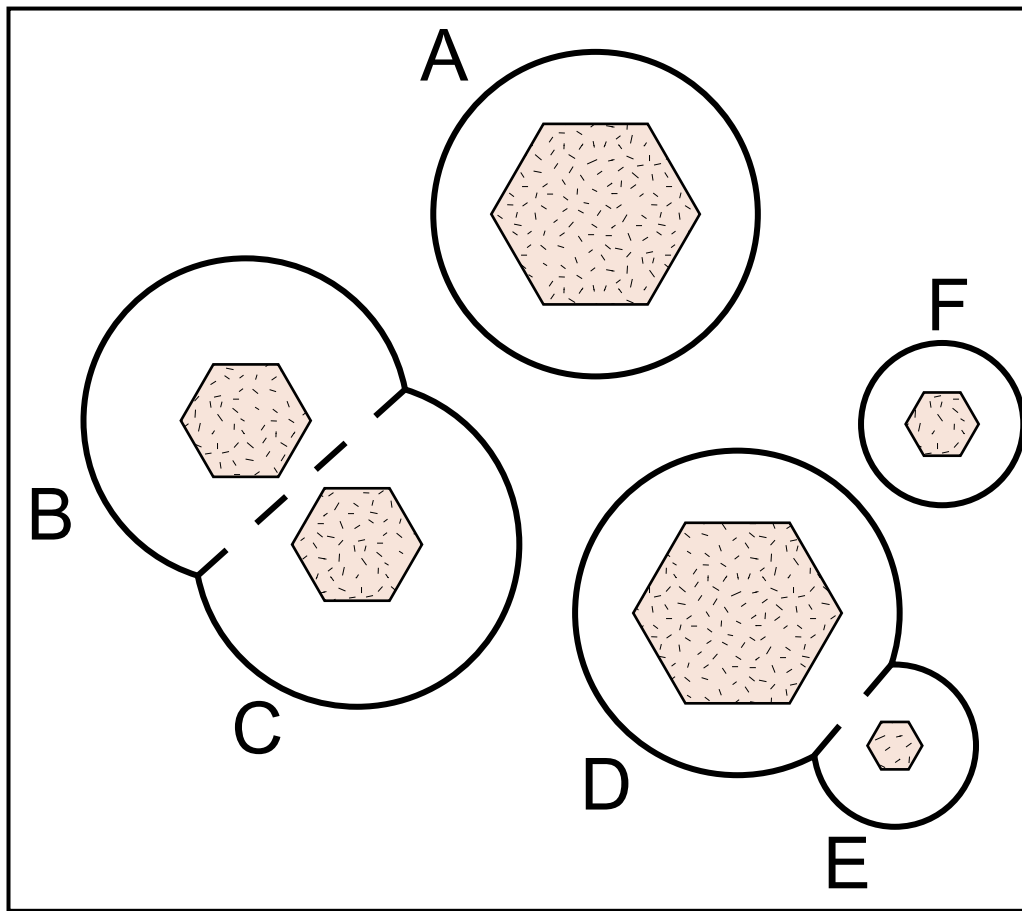
Figure 1.2. Schematic 2-D illustration of diffusion-controlled retardation of growth in the vicinity of a growing porphyroblast, after Carlson (1991). Competition for nutrients among closely-spaced porphyroblasts reduces the growth rates for crystals in close proximity to each other (B and C) relative to that for an isolated crystal (A) that nucleated at the same time. A crystal (E) that nucleates near the edge of the diffusionally-depleted zone of a pre-existing crystal (D) will initially have minor effects on the growth rate of the pre-existing crystal, but will itself grow more slowly than an isolated crystal that nucleated at the same time (F). Surfaces of impingement between adjacent depleted zones are the boundaries of diffusional domains; their approximate locations are marked by broken lines.
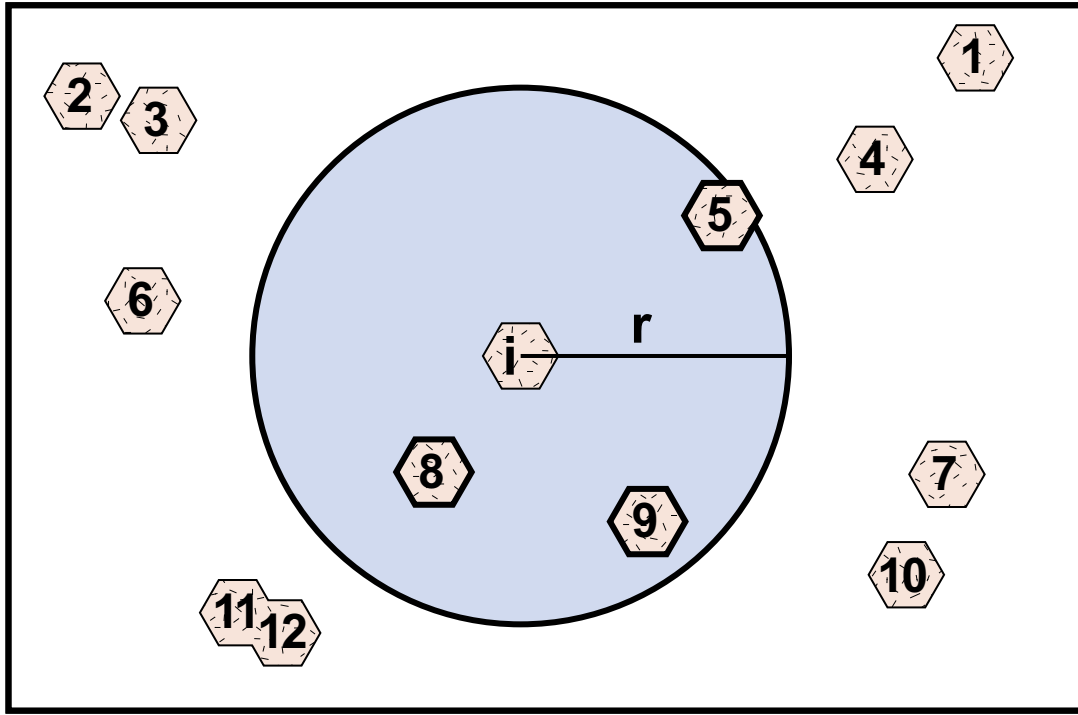
Figure 1.3. Schematic 2-D illustration of measurement regions for the *K*, *L*, and *L'* functions. For each crystal *i* in the sample, each other crystal *j* whose center lies within a sphere of radius *r* (shaded circle) centered at crystal *i* is counted. In this illustration, the crystals outlined in bold (*j*=5, *j*=8, and *j*=9) will be counted in the summand for crystal *i*; the others will not.
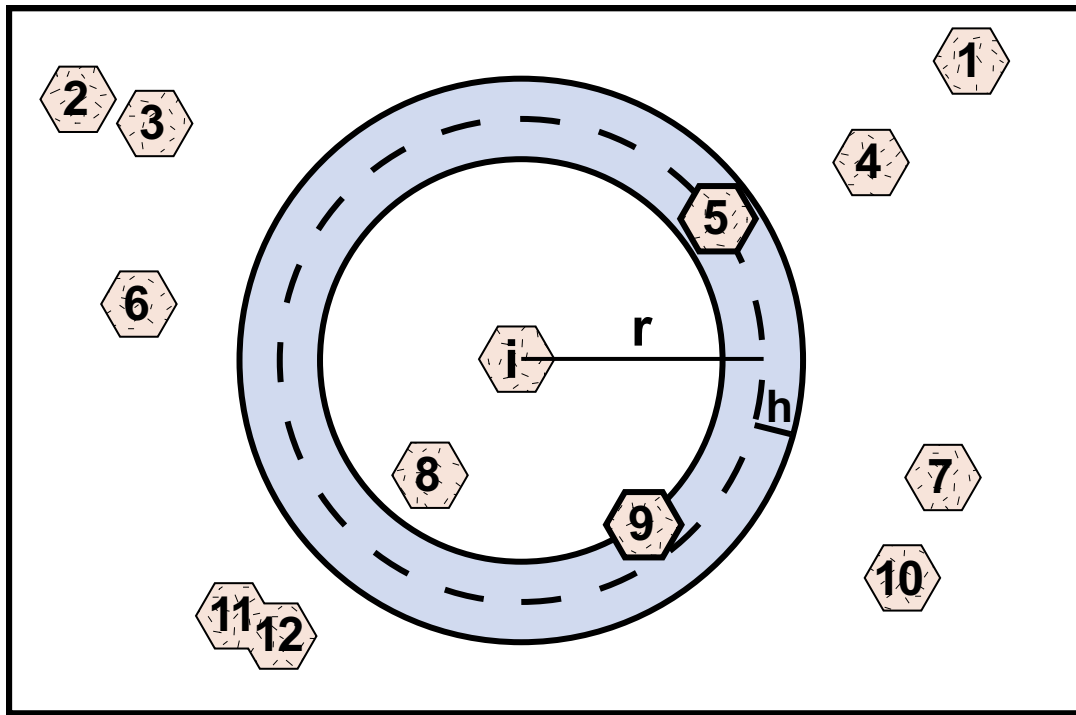
Figure 1.4. Schematic 2-D illustration of measurement regions for the Pair Correlation and Mark Correlation Functions. For each crystal i in the sample, each other crystal j whose center lies within a spherical annulus (shaded ring) of thickness $2h$ and radius r centered at crystal i is counted. In this illustration, the crystals outlined in bold ($j=5$, and $j=9$) will be counted in the summand for crystal i; the others will not.
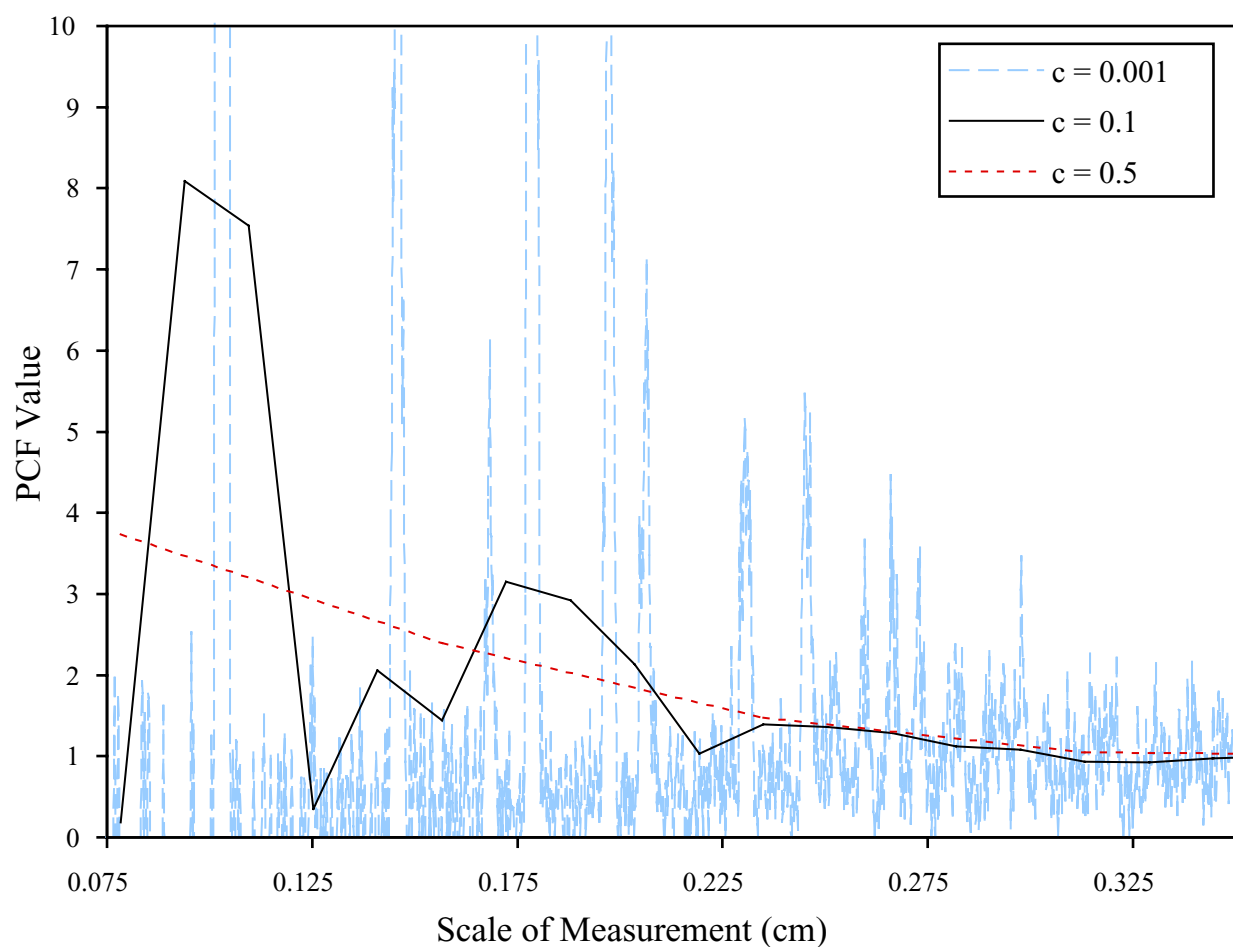
Figure 1.5. Illustration of the effect of varying bandwidth in the Epanecnikov kernel function on the Pair Correlation Function curve. Each of the four curves represents a re-analysis of the same data set (also analyzed in Figure 1B.7), varying only the value of c in order to alter the bandwidth. Larger values of the bandwidth $h = c\,\lambda^{-1/2}$ produce smoother curves; excessive smoothing from too large a bandwidth results in a loss of textural information. At small values of the bandwidth h, there are scales of measurement for which the calculation does not include any crystals.
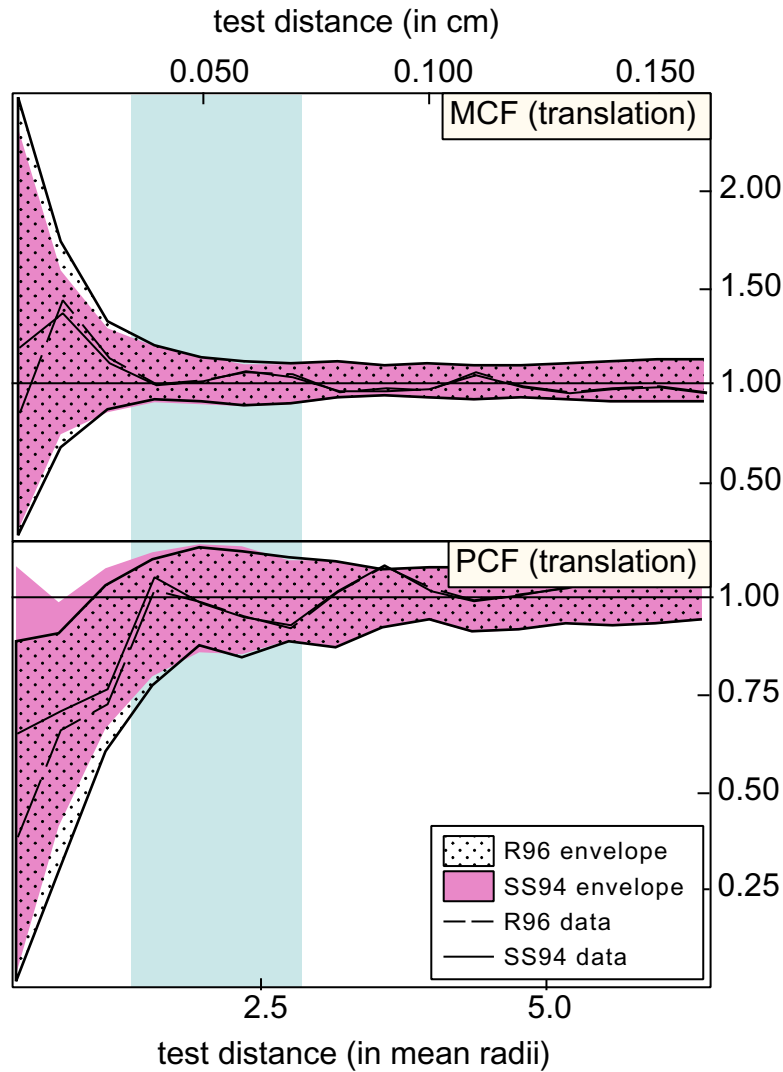
Figure 1.6. Comparison between the present versions of the MCF and PCF (taken from Stoyan and Stoyan, 1994, "SS94") and those proposed by Raeburn (1996), "R96", performed on the random simulation given in Figure 1.9. The Raeburn statistic is systematically slightly lower than the present version, particularly at small test distances, but because it is also used to measure the envelopes, compensating errors may leave the conclusion unchanged.
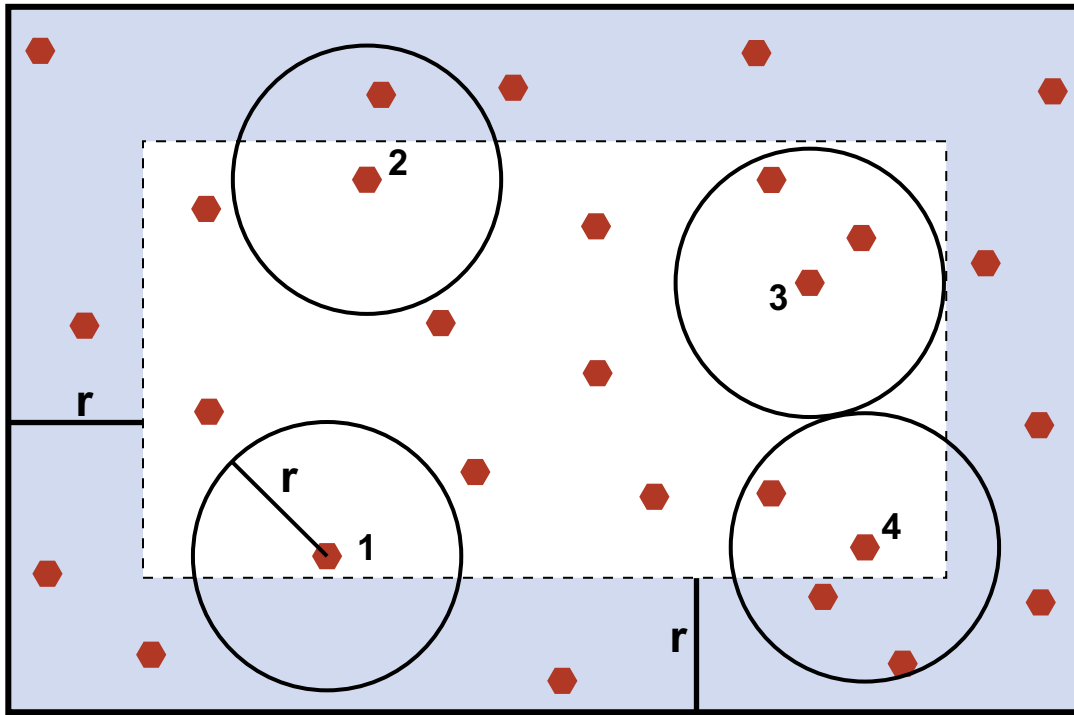
Figure 1.7. Schematic 2-D illustration of "minus-sampling" edge-correction method. A guard region (wide shaded border region) of the same thickness as the test distance, r, is placed inside the sample boundary. The iteration over crystals i (placement of measurement region) is prohibited from this region, although they may be counted as crystals j within measurement regions. This effectively prohibits the measurement regions from ever intersecting the sample boundary. Four allowable measurement regions are shown as solid circles.
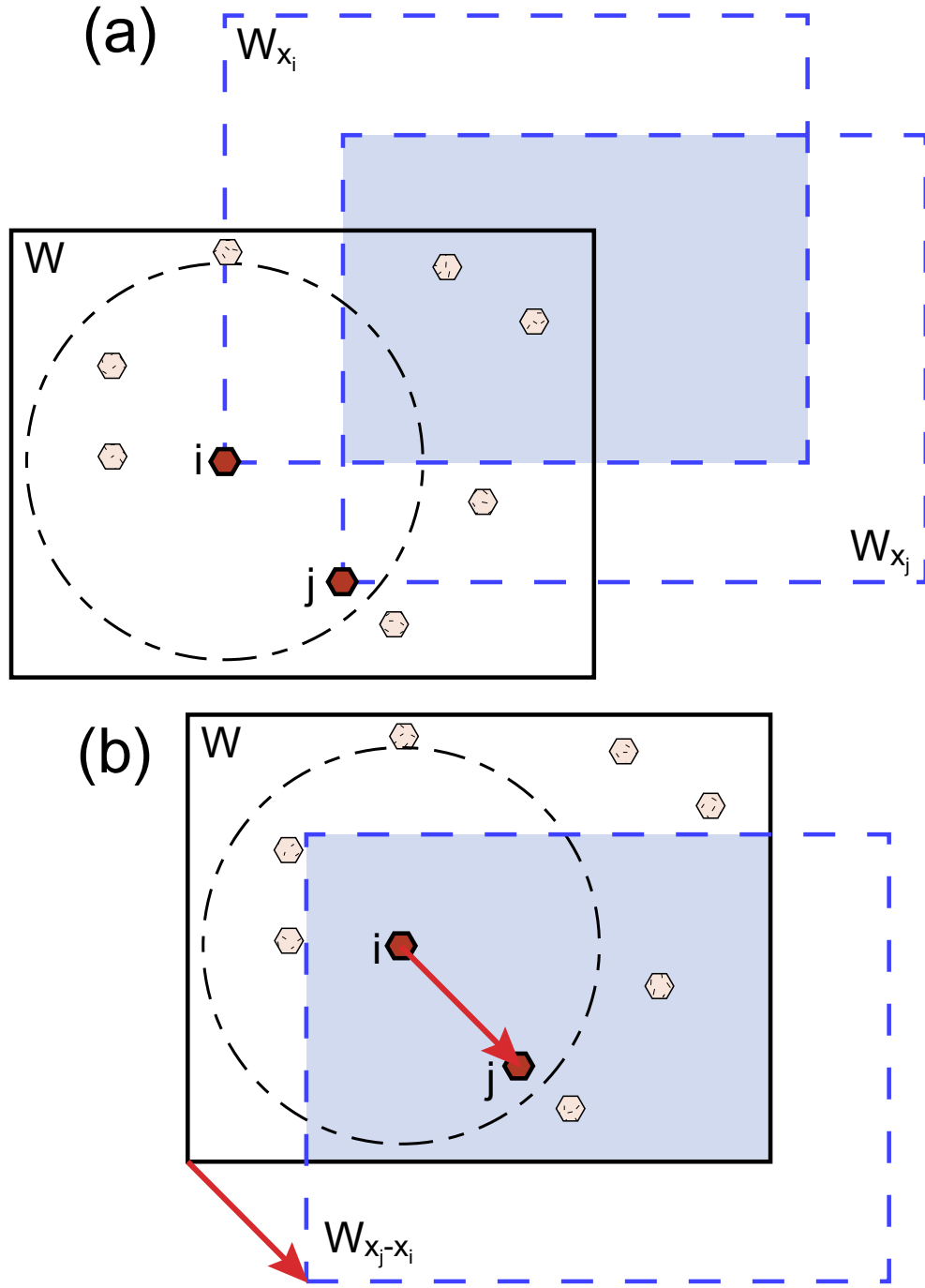
Figure 1.8. Schematic 2-D illustration of translation edge-correction method. For the pair of crystals in bold, i and j, the summand is divided by the volume of the shaded region. (a) As defined in Stoyan and Stoyan (1994), this region is $W_{x_i} \cap W_{x_j}$, the intersection of the sample region W offset to each of the crystals in the pair. (b) This volume is equivalent to $W \cap W_{x_j-x_i}$, the intersection of the sample region W and that region offset by the vector from the center of crystal i to the center of crystal j. The value of the summand is normalized by this intersection volume for each pair counted.
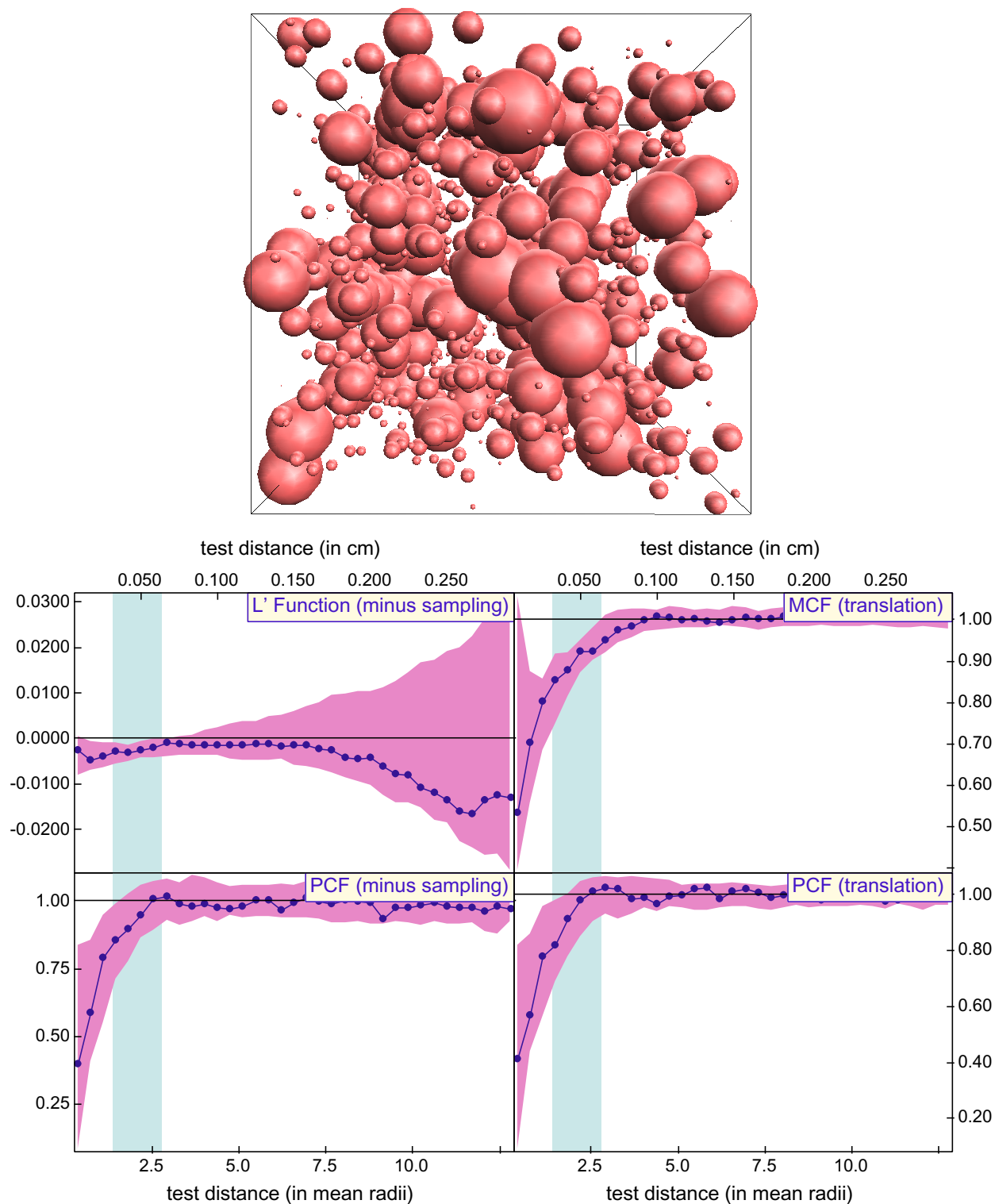
Figure 1.9. (a) Rendering of sub-volume of simulation IC-2, a thermally accelerated interface-controlled nucleation and growth simulation of 1739 crystals. (b) Correlation functions measured on this simulation; data fall within the 2-σ envelope, as expected.
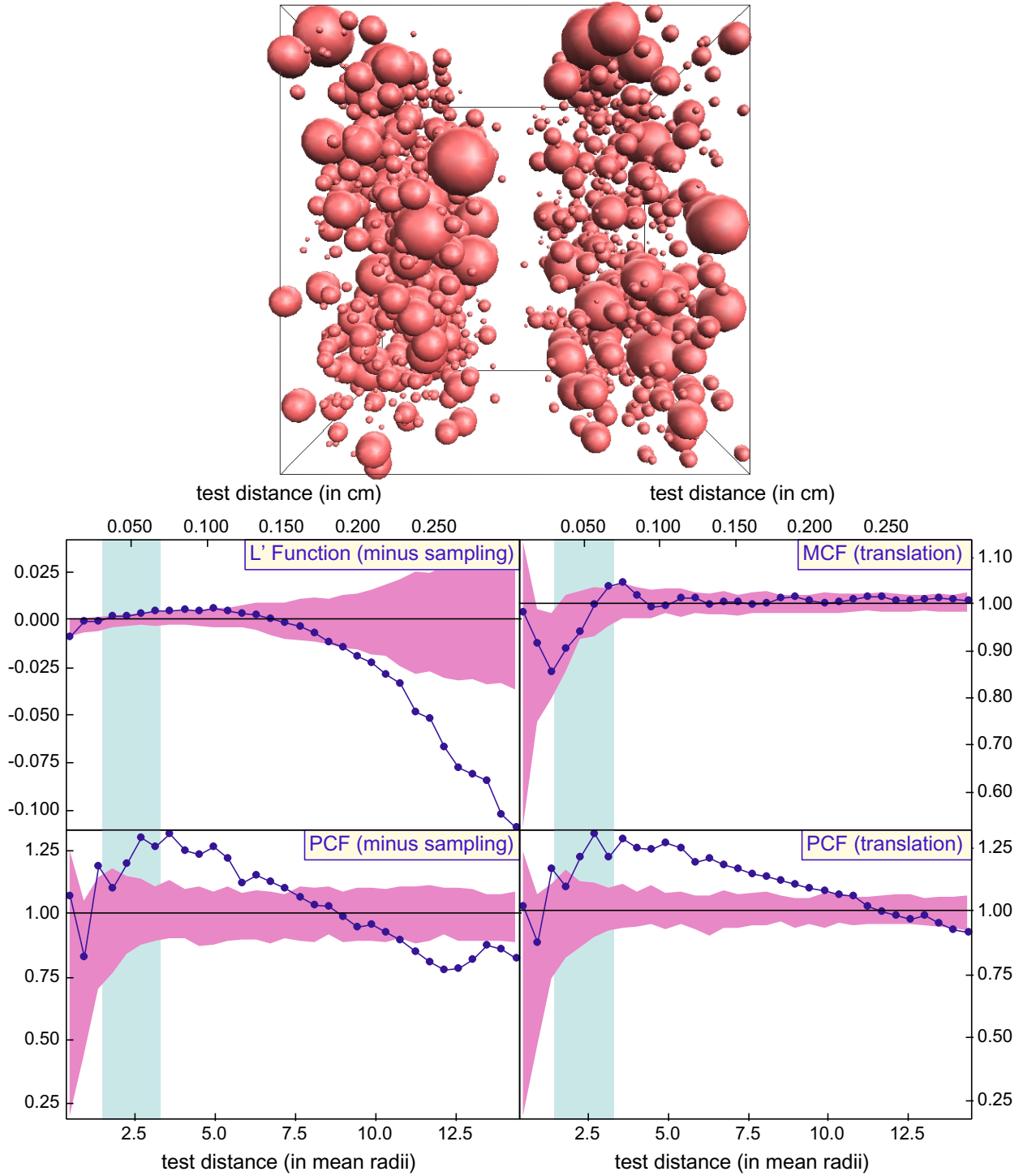
Figure 1.10. (a) Rendering of sub-volume of layered simulation IC-L2, in which layering is induced by a sinusoidal nucleation probability in one dimension imposed on a simulation of thermally accelerated interface-controlled nucleation and growth. (b) Results of correlation functions measured on this layered array of 1172 crystals. Data show clustering up to about 10 mean radii (~0.2 cm), and fall below the 2-σ envelope at greater length scales, reflecting the relative sparsity of crystals beyond the scale of layering; the MCF data show no growth suppression, as expected from input parameters of simulation IC-L2.
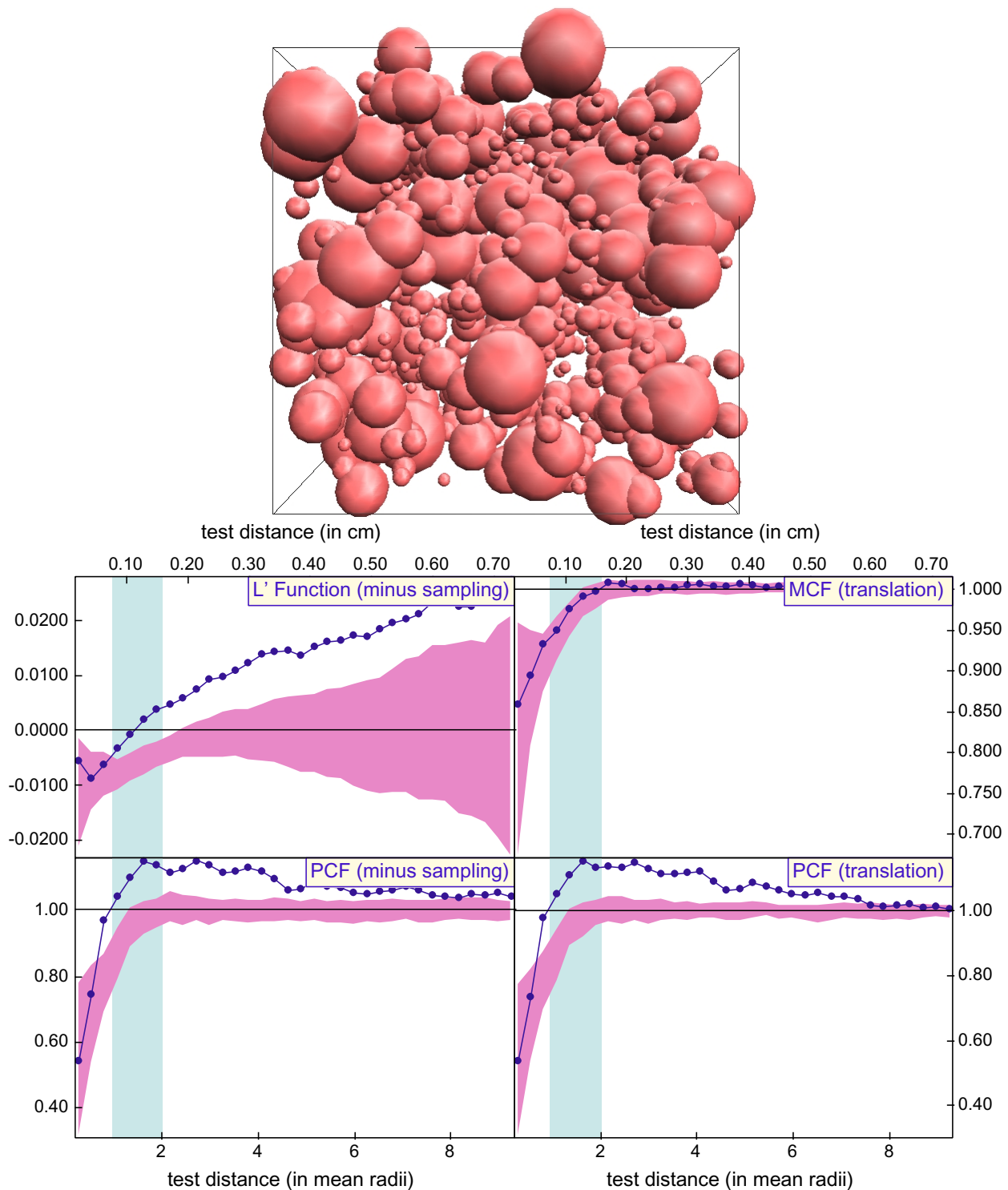
Figure 1.11. (a) Rendering of simulation IC-WR1, a thermally accelerated interface-controlled nucleation and growth simulation of 5096 crystals with clustering induced by sinusoidal nucleation probability in each dimension. (b) Correlation functions measured on this simulation. The data fall above the 2-σ envelope at all scales but the smallest, reflecting the clustering of the simulation; the MCF data show no growth suppression, however.
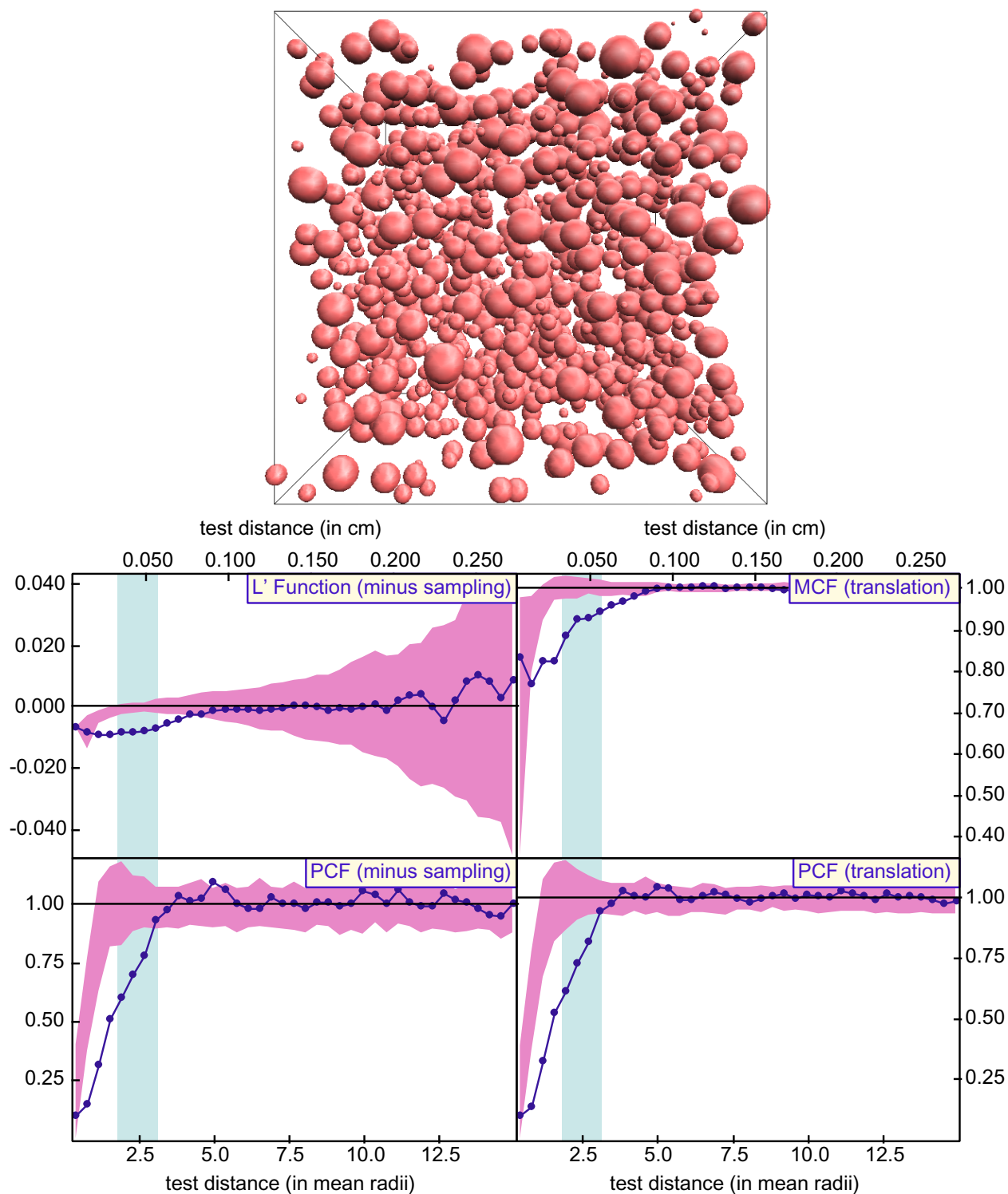
Figure 1.12. (a) Rendering of simulation DC-1, a thermally accelerated diffusion-controlled nucleation and growth simulation of 2971 crystals. (b) Correlation functions measured on this simulation. Data fall below the 2-σ envelope at scales up to the mean nearest-neighbor distance, as expected, and the MCF shows a correlation between separation and size, indicating growth suppression at small separations.
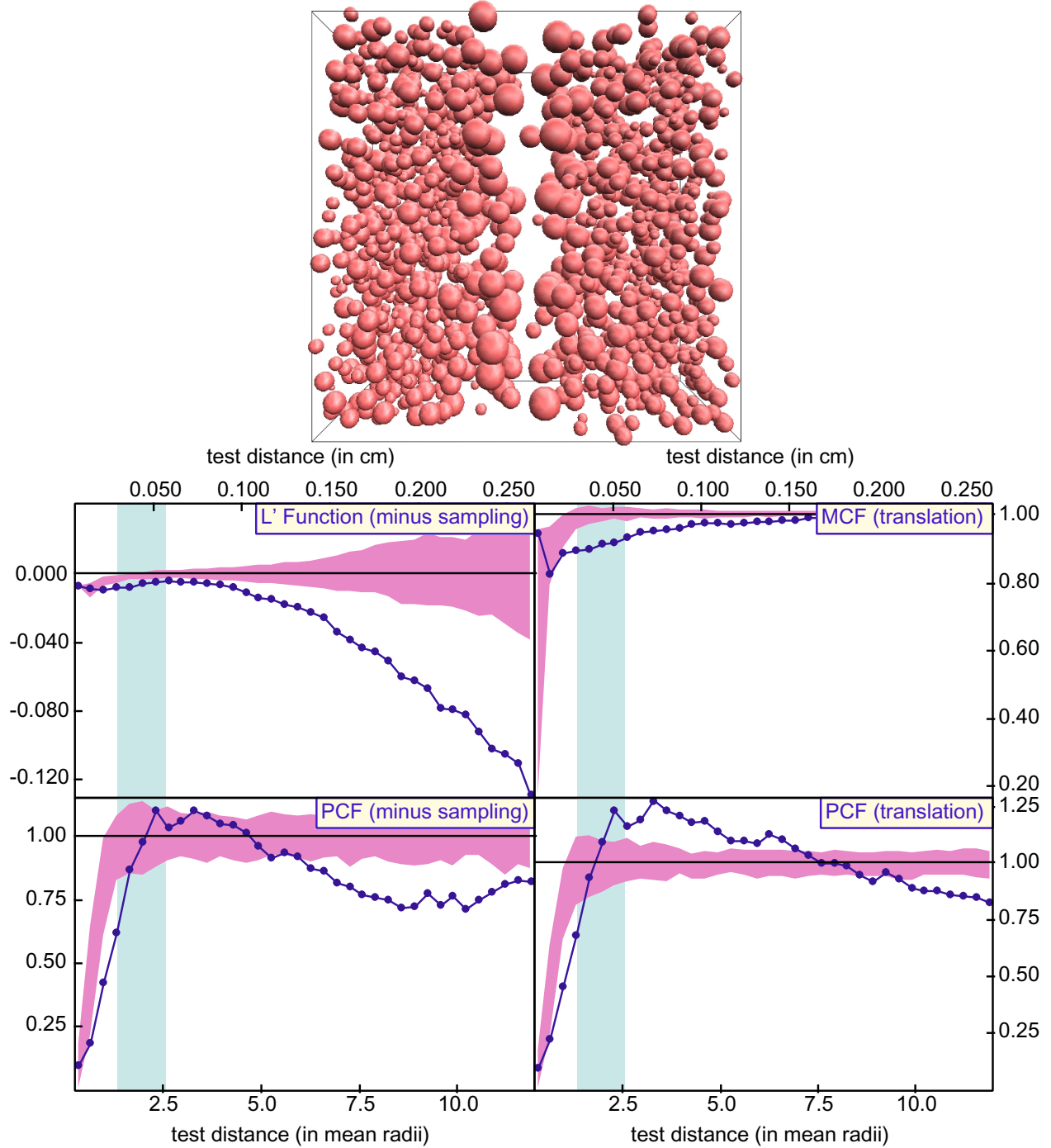
Figure 1.13. (a) Rendering of sub-volume of layered simulation DC-L4, in which layering is induced by a sinusoidal nucleation probability in one dimension imposed on a simulation of thermally accelerated diffusion-controlled nucleation and growth. (b) Correlation functions measured on this layered array of 1185 crystals. Envelope simulations incorporate nucleation probability distributions identical to DC-L4. Data fall below the 2-σ envelope at small scales, show clustering at larger scales, and then ordering at the scale of the layering, as expected. The MCF data are suspect because the simulation algorithm leads to large crystals bordering the sparse regions.

1-40
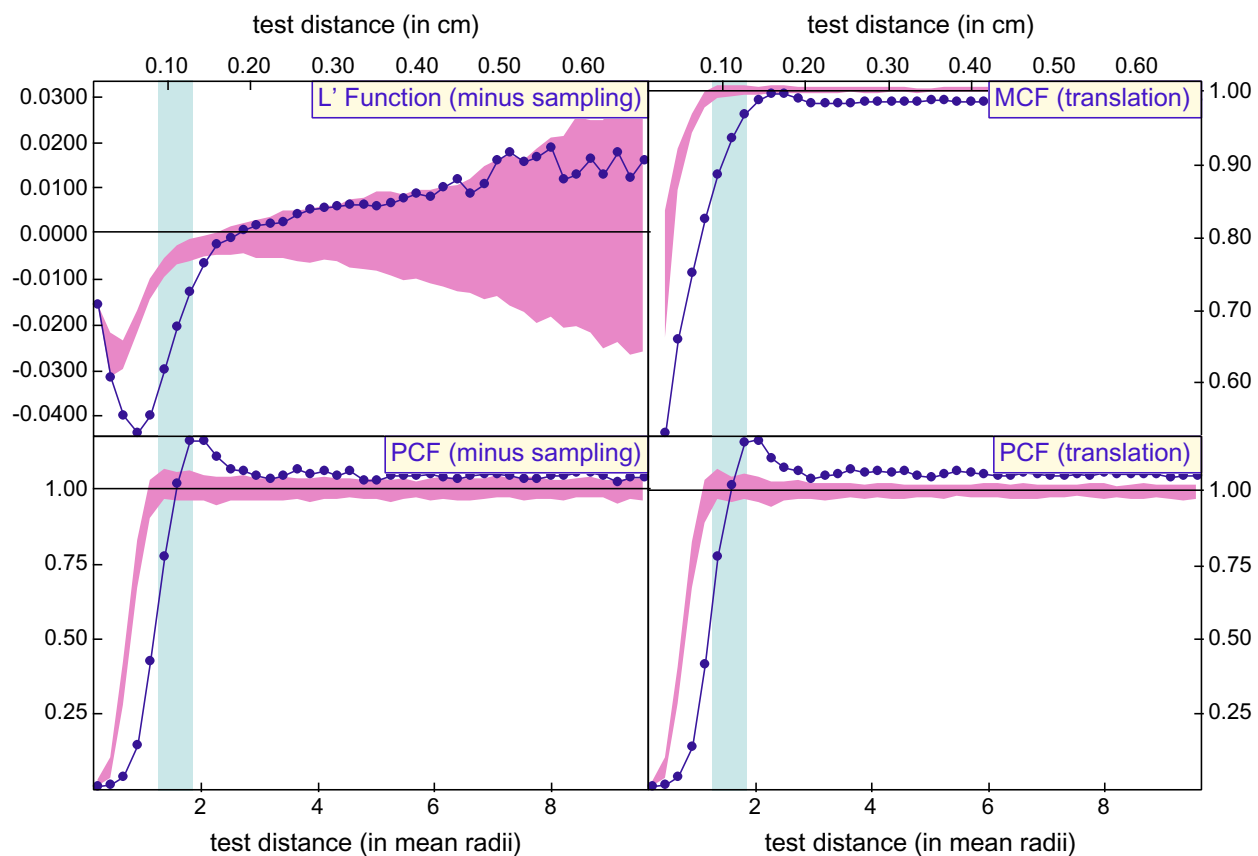
Figure 1.14. Correlation function data for sample PM1. The data show the result expected from the single-valued statistics: both ordering and growth suppression up to about the mean nearest-neighbor distance.
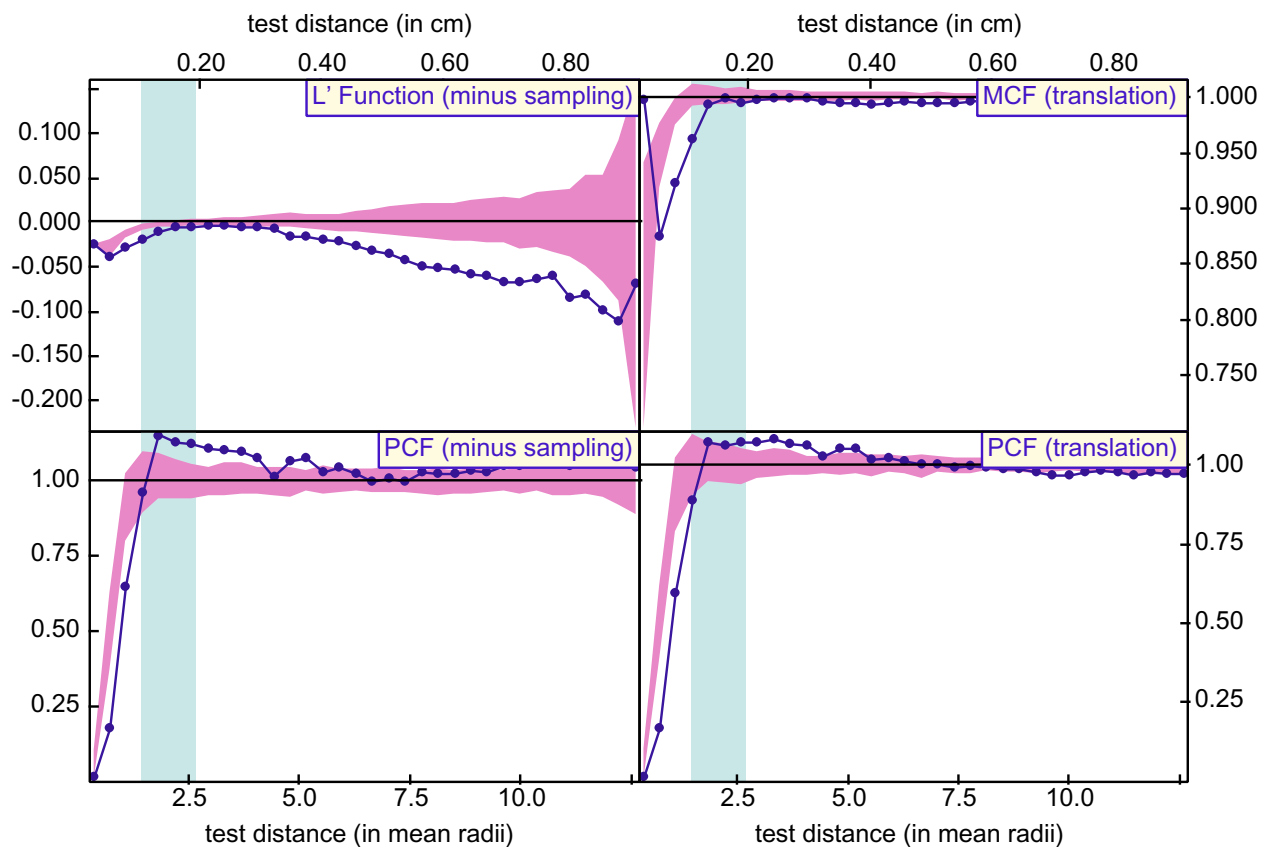
Figure 1.15. Correlation function data for sample PM2. The data show ordering of crystal centers and suppression of growth, in agreement with the single-valued statistics.
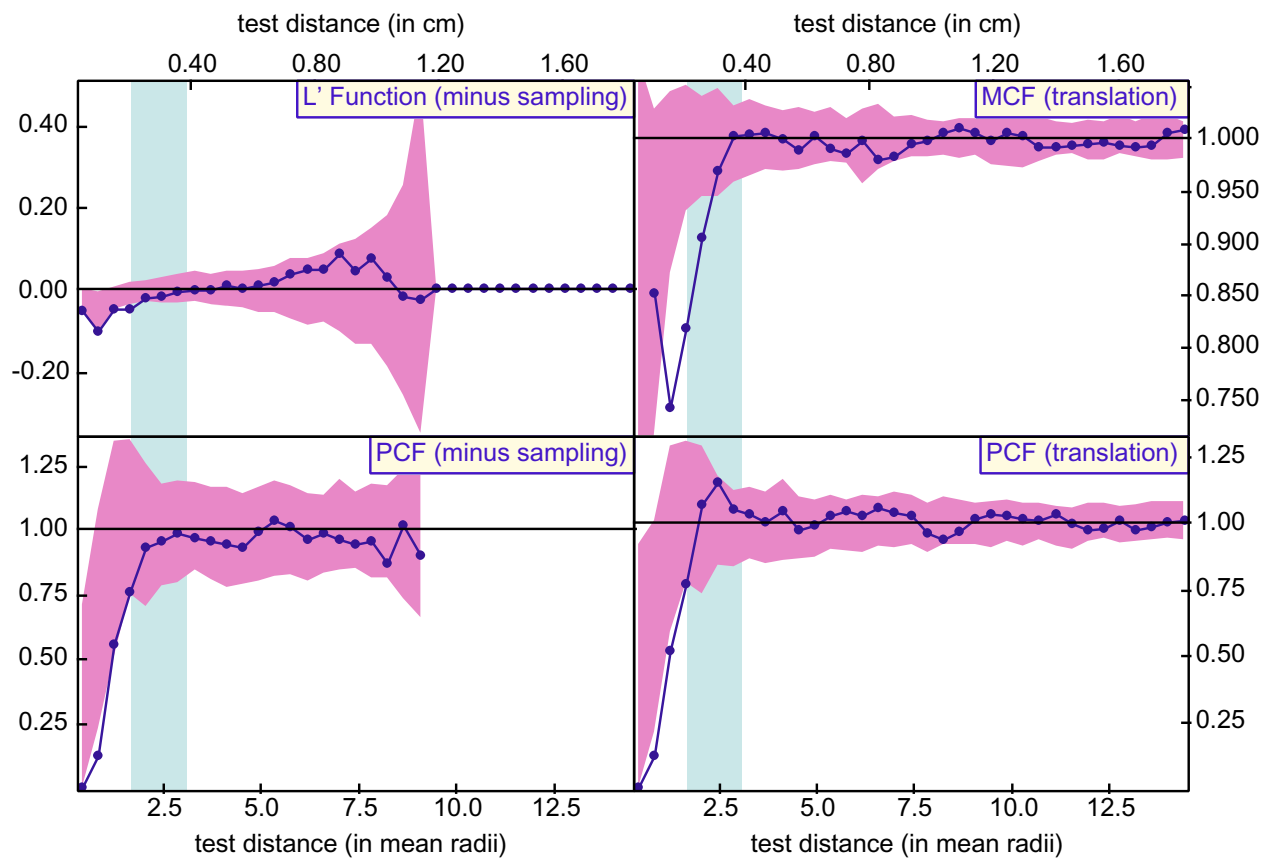
Figure 1.16. Correlation function data for sample MD. The data show slight negative excursions below the null-hypothesis region for the *L'* function and PCF, indicating barely significant ordering of crystal centers, and a strong excursion below the envelope for the MCF, indicating growth suppression for closely spaced crystals.
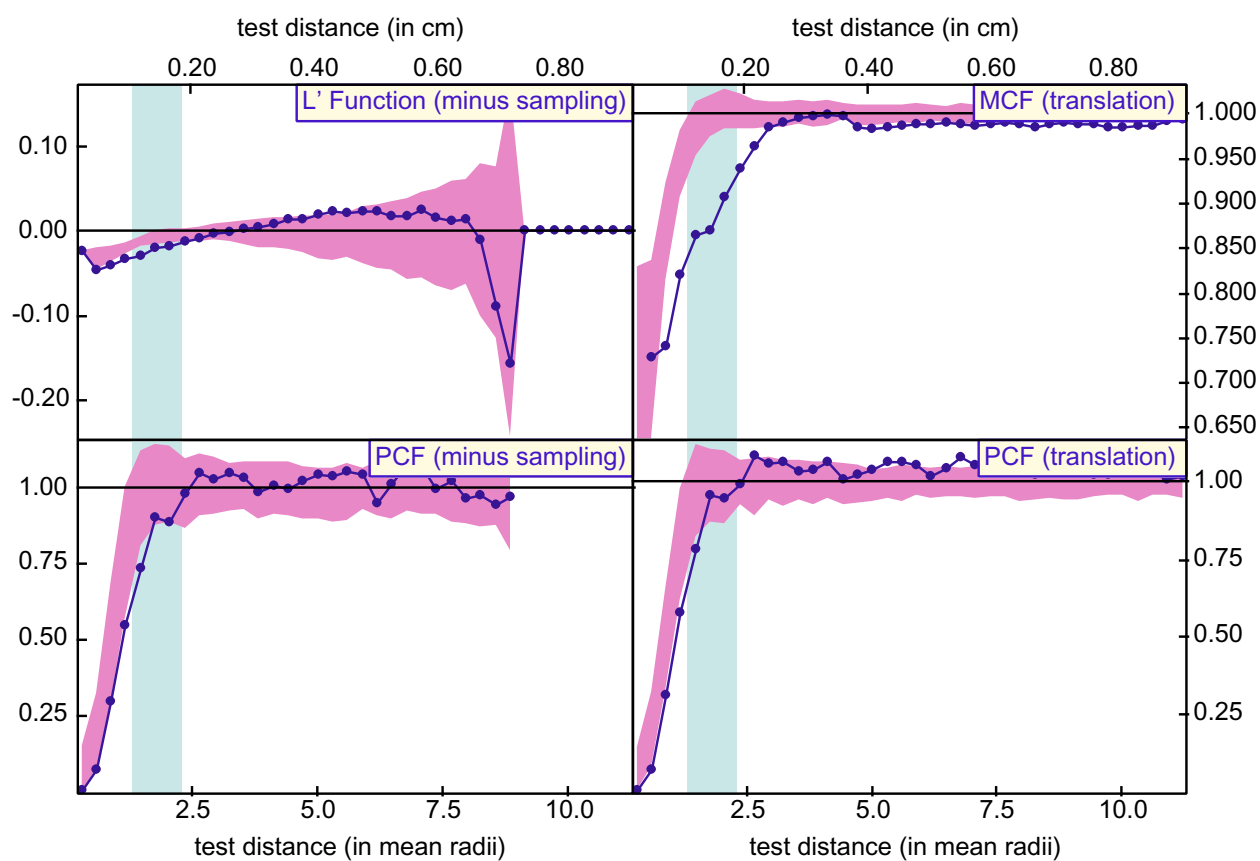
Figure 1.17. Correlation function data for sample WR1. The data show ordering of crystal centers and suppression of growth, in agreement with the single-valued statistics.
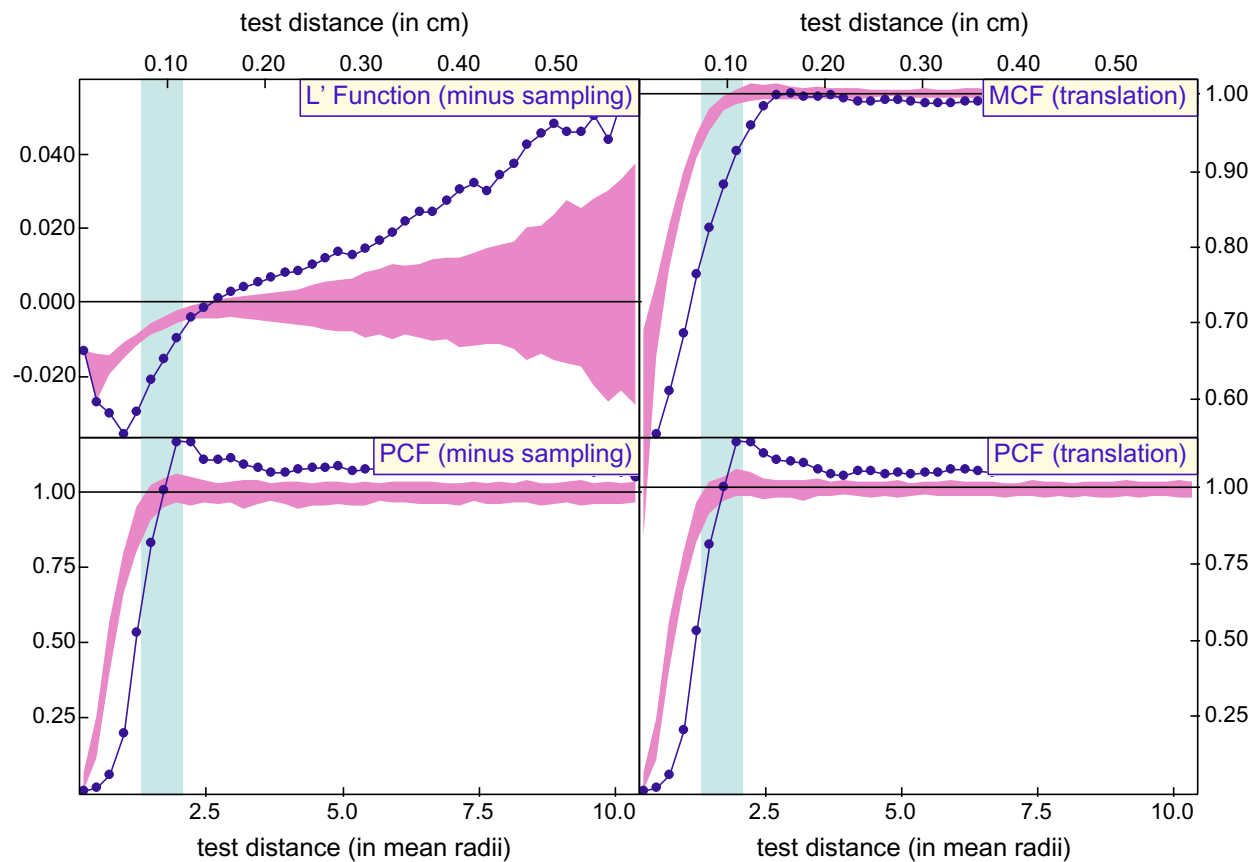
Figure 1.18. Correlation function data for sample WR2. The data show ordering of crystal centers and suppression of growth, in agreement with the single-valued statistics.
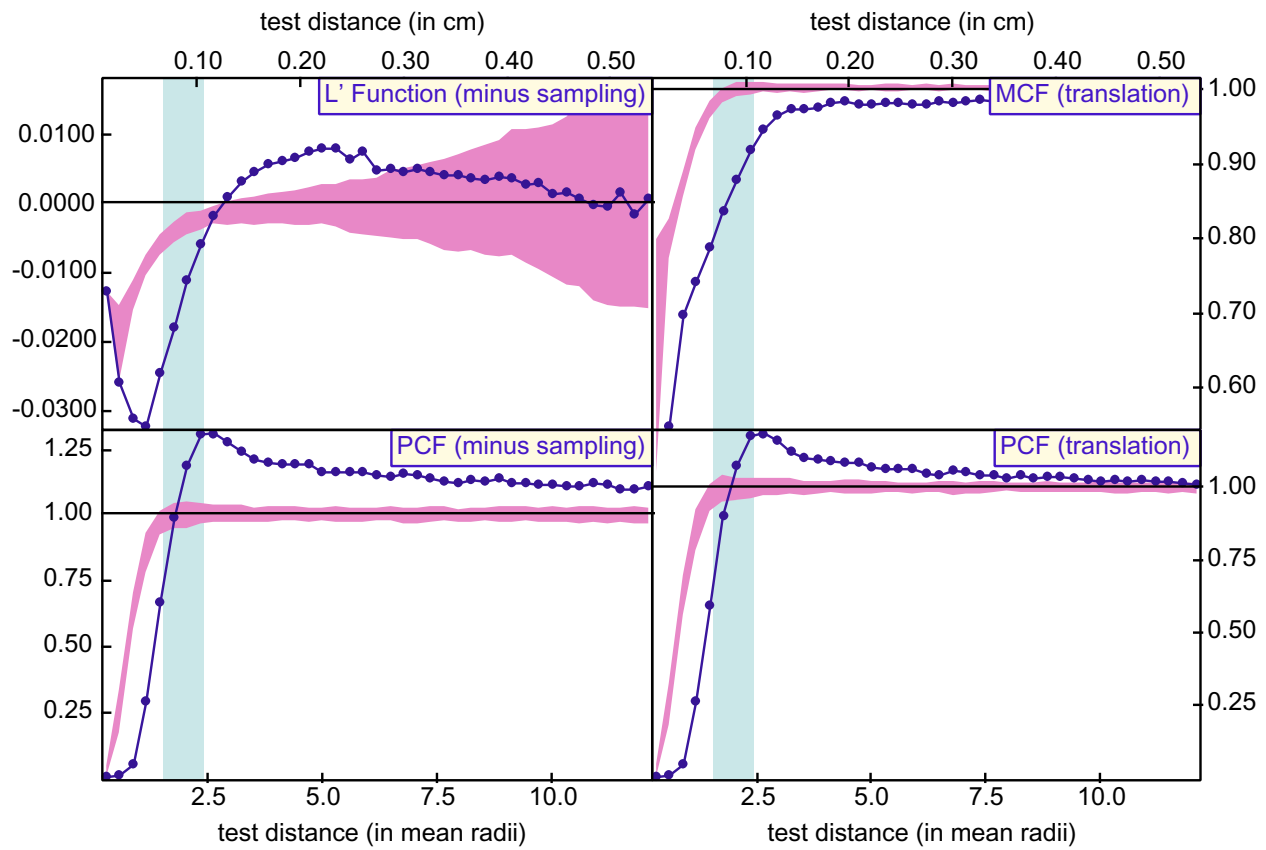
Figure 1.19. Correlation function data for sample WR3. The data show ordering of crystal centers and suppression of growth, in agreement with the single-valued statistics.
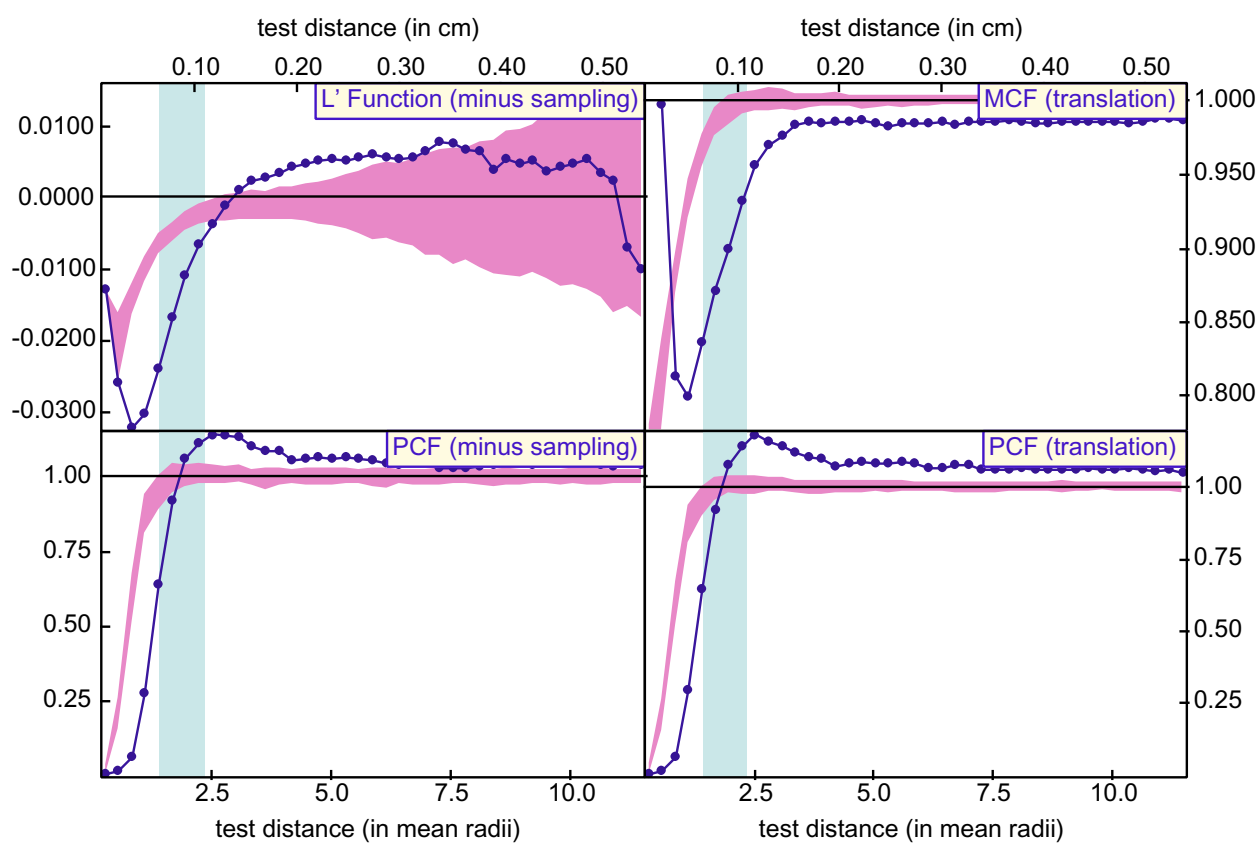
Figure 1.20. Correlation function data for sample WR4. The data show ordering of crystal centers and suppression of growth, in agreement with the single-valued statistics.

APPENDIX 1A. CORRECT PRODUCTION OF NULL-HYPOTHESIS ENVELOPES

Importance

One conclusion of this study that deserves special emphasis concerns the production of correct envelope simulations, which produce the interface-controlled null-hypothesis regions to which each rock's statistics may be compared. Errors in the production of envelopes may produce nonsensical results, which are easily detected, or may produce results that, while not obviously wrong, are nonetheless incorrect, and lead to incorrect conclusions.

The shape of the sample must be replicated in the envelope simulations. If this is omitted, then the edge-correction methods will have differing effects in the sample as compared to the envelope simulations.

The set of crystals, including the radius of each, must be replicated in the envelope simulations.

The envelope simulations must reflect any limitations on crystal observability that are present in the natural data. The observability criterion must be tuned for the data-collection measures used to obtain the spatial data from the rock sample. If this is not performed, then the statistical measures of the rock may show reduced or excess ordering relative to the envelope simulations, and diffusional control may be mistakenly concluded or mistakenly rejected (Fig. 1A.1). Observability criteria are discussed in detail below.

The crystals in the envelope simulations must be placed with the restrictions enforced by the interface-controlled growth rate. If this is omitted, then, depending on the placing method used, the simulations may show either excess ordering or excess clustering relative to the rock, and conclusions drawn will then be incorrect.

Calculation

The production of null-hypothesis regions for each statistic is vital, and is quite exacting. Great care must be taken in their calculation, for testing has shown that even moderately sophisticated envelope-production methods can produce erroneous conclusions. The method used in the present work to produce correct envelope simulations is detailed below; it has been extensively tested against a large database of controlled simulations of both interface-controlled and diffusion-controlled nucleation and growth produced by time-explicit methods.

Crystal placement. Each envelope simulation is an artificial array of crystals designed to model the statistical characteristics of a rock with a given crystal size distribution that formed in an interface-controlled

episode of nucleation and growth. By this it is meant that as many parameters as possible for the rock under analysis are mirrored in the envelope simulation. This is accomplished by creating a set of crystals whose sizes match those of the crystals in the rock under analysis and placing those crystals in a bounding box of identical size and shape to the rock, from largest to smallest, in random locations (as expected in an interface-controlled nucleation environment). The volume effect – that is, the impossibility of a crystal nucleating inside a pre-existing crystal – is taken into account as follows. If any crystal, when randomly placed, is found to overlap a previous crystal, a test is performed to check whether the later-placed crystal could have nucleated in that location relative to the earlier one, or whether that nucleation site would have been within the pre-existing crystal. Because for interface-controlled growth, radii are proportional to the elapsed time since nucleation, this check is easily performed by removing from both crystals the radius of the smaller one, and testing whether the nucleation point lies within the body of the earlier-nucleated crystal as it existed at the nucleation time of the later crystal. This requirement is expressed mathematically as follows:

$$d \quad r_L - r_S , \tag{1A.1}$$

where d is the center-to-center distance between the two crystals, and r_L and r_S are the radii of the larger and smaller crystals, respectively. This requirement stems from the linear relation between radius and time elapsed since nucleation under an interface-controlled growth law. If this inequality is true, then the location is allowed; if not, a new random location is selected.

Volume Fraction. The possibility of matching the volume fraction between the sample and the envelope simulations was explored. One would have to compromise between a precise match to crystal sizes and a precise match to volume fraction, unless the degree of overall impingement of crystals were also matched. However, as degree of impingement is strongly linked to the short-range ordering features of the sample, doing so would always produce an envelope with ordering features matching the data set. This would invariably lead to the erroneous conclusion of interface control in every case.

A number of test runs were performed using various simulations, both interface- and diffusion-controlled, and the difference was minimal between matching volume fraction moderately closely, and not matching volume fraction at all. Attempting to match volume fraction between the sample and the null-hypothesis simulations was judged to be less than rigorous, insofar as it produced envelopes whose crystal size distributions did not precisely match those of the sample data sets; the additional computation time required is a further disadvantage to this approach.

Observability. Another key issue to consider is observability. In an interface-controlled nucleation and growth regime, highly interpenetrating pairs (and clusters) of crystals may exist. These highly overlapped crystals are generated in time-explicit interface-controlled nucleation and growth simulations, and are permitted by the interface-controlled placement criterion given in equation (1A.1). In natural samples, however, they might not be observed if the interpenetration produces shapes for the compound crystals that cannot be resolved as clusters and separated into individual crystals. This observability problem will arise during the analysis of sample data collected by many techniques, including the serial sectioning and optical scanning technique (Raeburn, 1996; Daniel and Spear, 1999) and the technique of computed X-ray tomography we have used.

Pairs of highly intergrown crystals in a rock may sometimes be misidentified as single, larger crystals. When this occurs, the data set extracted from the rock will contain too few crystals; those crystals will have exaggerated sizes and the mean nearest-neighbor distance will be too long. These errors will invalidate comparisons made to envelope simulations in which all crystals are regarded as separately observable, regardless of how close to one another they may be. To remedy this problem, the following observability criterion is employed in the envelope simulation runs applied to natural data sets.

The observability criterion is has two parts: the pair must satisfy both parts in order to be considered separately observable. The first part of the criterion is

$$d \quad (0.85)\, d_I \,, \tag{1A.2}$$

where d is the center-to-center distance between the two crystals, and d_I is the distance from the center of the larger crystal to the plane that contains the circle of intersection of the (spherical) crystal surfaces. The second part of the criterion is

$$l \quad 3\, r_S \,, \tag{1A.3}$$

where l is the total length of the pair of crystals and r_S is the radius of the smaller crystal. If the pair fails either of these tests, then it is concluded that the two crystals cannot be distinguished as separate from one another, and the later-placed crystal is repositioned randomly.

The values of the numerical constants in these tests were obtained by a tuning process that subjected actual data sets obtained from both CT imagery and time-explicit nucleation and growth simulations to the observability criterion. The numerical values were varied in order that the number of crystal pairs classed as "inseparable on observation" is maximized in the simulations and minimized in the CT-derived data sets.

1-50

This is clearly appropriate because all the crystals in the CT-derived data sets were, in fact, separately observed and must therefore be clearly distinct from their neighbors.

This filter typically rejects a large proportion of attempted crystal placings as inseparable on observation, although this proportion is dependent on volume fraction. The mean percentage of rejections based on each criterion made in producing envelope simulations for each rock sample is given in Table 1A.1.

After all crystals have been placed, the simulation is the best estimate for what the rock under analysis would look like if it had originated in an interface-controlled process. In this way, the set of envelope runs becomes the null-hypothesis result of interface-controlled nucleation and growth to which one can legitimately compare the results for the rock under analysis.

Diffusion-controlled envelopes

Although, as stated in the text, we believe that the production of statistically rigorous null-hypothesis regions representing diffusion-control is at present computationally prohibitive, it is appropriate to discuss instances of these regions presented in the literature (Raeburn, 1996; Daniel and Spear, 1999). We believe that the algorithm used to produce these diffusion-controlled simulations is oversimplified, and fails to take into account important factors in the diffusion-controlled nucleation and growth process, such as impinging diffusional domains, and radial growth rates that vary with time.

The production of these regions is very similar to the production of the interface-controlled regions detailed above, but the placing criterion is adjusted to attempt to account for the expanded volume around each growing crystal in which nucleation is prohibited in a diffusion-controlled nucleation and growth regime. The adjusted placement criterion is:

$$d \quad (R_{dpl} / R) (r_L - r_S), \qquad\qquad (1A.4)$$

where R_{dpl} is the radius of the depleted zone around a garnet at the conclusion of growth, R is the radius of the garnet, and other variables are the same as those in equation (1A.1). The ratio (R_{dpl}/R) is related to the volume fraction by:

$$(R_{dpl} / R) = (VF)^{-1/3}, \qquad\qquad (1A.5)$$

where VF is the volume fraction of porphyroblast material in the sample. Note that in Daniel and Spear (1999), they use a volume fraction in this calculation modified from that given in their Table 1 to account for the portion of the sample volume occupied by quartz veins (Daniel, 1999, pers. comm.).

In order to test this method of production of "diffusion-controlled" envelope simulations, we subjected a simulation produced by a thermally accelerated, diffusion-controlled nucleation and growth algorithm to statistical analysis, but using equations (1A.4) and (1A.5) for production of the null-hypothesis region. As is clear from Figure 1A.2, the envelopes differ significantly from the simulated data set, known to be diffusion-controlled, suggesting that the method of calculation of these "diffusion-controlled" null-hypothesis regions is incorrect. Although in Figure 1A.2 the functional values for the known diffusion-controlled simulation fall below the envelopes calculated in this way, it is not clear that this will always be the case; the difference between the two may depend on factors such as crystal number density, volume fraction, the relative rates of nucleation and diffusion, and perhaps heating rate.

Tables

TABLE 1A.1. OBSERVABILITY CRITERIA STATISTICS

Percent of crystal placings required by observability criteria to be repeated during production of envelope simulations.

Rock	Volume fraction	Percent re-placings	
		Criterion 1	Criterion 2
PM1	0.380	7.4	15.8
PM2	0.108	0.4	1.1
WR1	0.245	1.7	1.3
WR2	0.420	10.9	6.1
WR3	0.269	7.5	6.9
WR4	0.264	2.4	1.1
MD	0.076	6.4	19.5
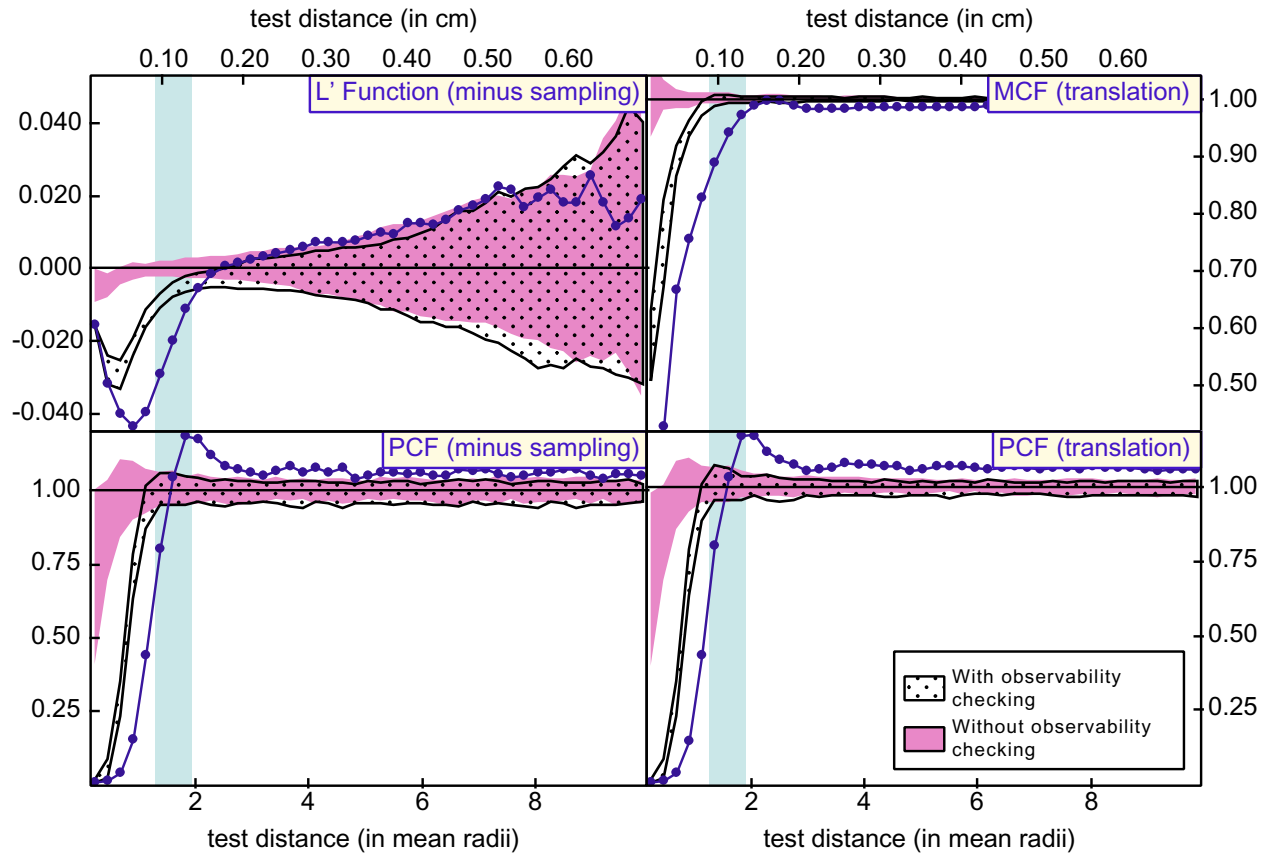
Figure 1A.1. Correlation functions measured on sample PM-1 both with and without ensuring that the envelope simulations have the same observability criteria as the sample. The envelopes that incorporate observability criteria show significantly lower statistical values than those without. This indicates that the observability criteria produce more conservative conclusions, i.e., they are less prone to provide spurious indications of ordering.
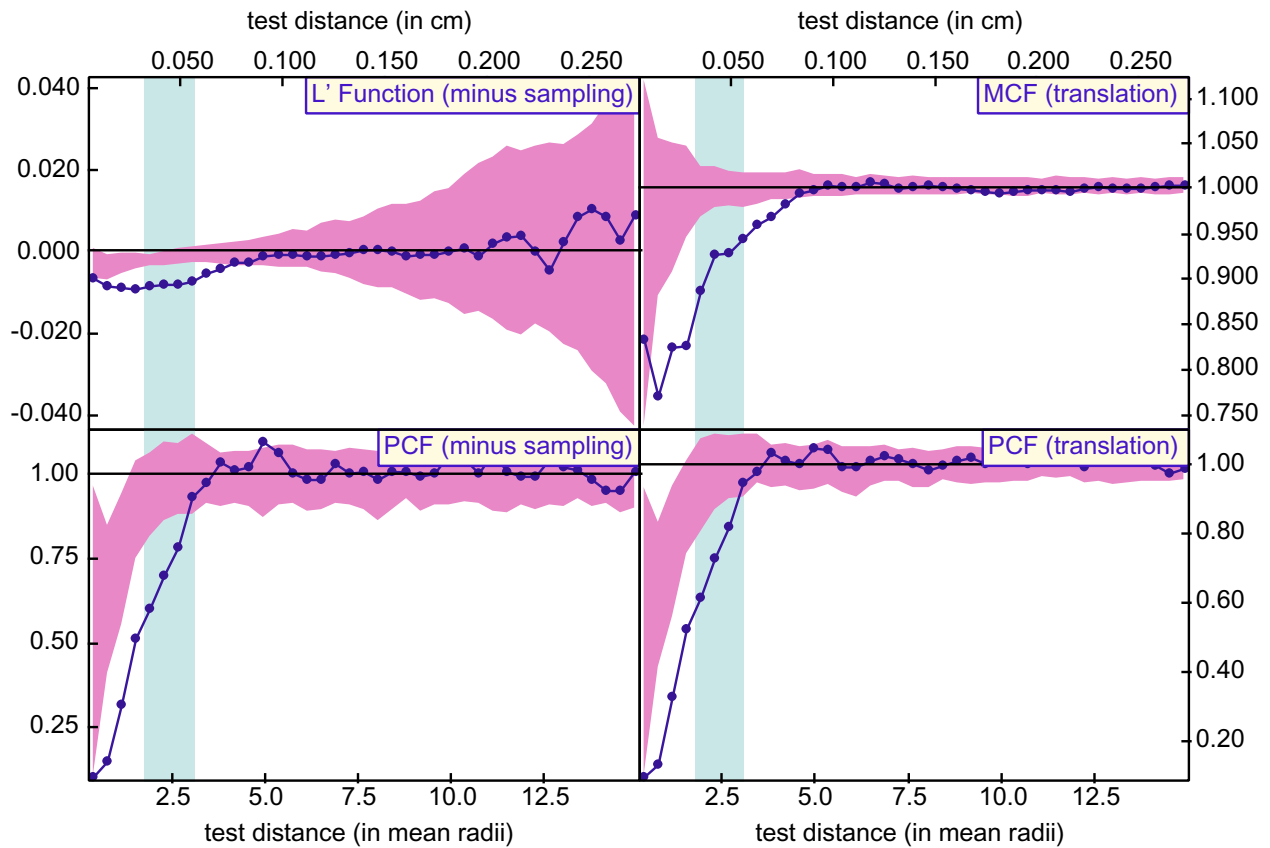
Figure 1A.2. Correlation functions measured on thermally-accelerated nucleation and growth simulation DC-1, also shown in Figure 1.12. Here the shaded envelope is produced not by making a large number of interface-controlled simulations, but by the method given in Daniel and Spear (1999) for their "diffusion-controlled" null-hypothesis envelope. The disparity between the statistical values measured on a known diffusion-controlled simulation and those measured on the envelope cast doubt on the validity of this method for calculating a diffusion-controlled envelope.

Case I: Random simulation.

The default case that the statistics must reproduce is a random array of points, but because that has no geological relevance, we test the distribution most similar to that: an array of randomly-placed crystals with limited overlap. A random simulation was made of 1000 crystals in a 1-cm^3 cube, with random radii up to 0.05 cm and with later-placed crystals allowed to overlap earlier-placed crystals by an amount dictated by the interface-controlled growth criterion, that is, no crystal can have nucleated inside the volume of a pre-existing crystal (see Appendix 1A for a complete description). The results for this simulation are given in Figure 1B.1. As expected, for both edge-correction methods, the L'-function is near the Poisson-distribution value of zero, and the PCF and MCF are near unity. The data fall within the 2- interface-controlled envelope, as one would expect, as this simulation is very nearly the same as those used in the envelope calculation. Just as one would expect based on the 2- criterion, few points fall outside the null-hypothesis envelopes. The minus-sampling edge-correction method has an increasing amount of noise relative to the translation method as the test distance increases, as it is being calculated with decreasing numbers of crystals.

Case IIa: Ordered simulation, no noise.

To confirm that the statistics can reveal ordering trends in the data, an array of hexagonal-closest-packed crystal centers was tested, the most ordered array possible. An ordered simulation of 938 crystals in a 1-cm^3 cube was produced in which crystal centers are located in a hexagonal-close-packed array with a 0.001 cm offset in a random direction (for computational purposes), giving an inter-crystal distance of ~0.11 cm. As above, the radii are random up to 0.05 cm. The results for this simulation are given in Figure 1B.2. Because these simulations are nearly perfectly ordered, they produce results atypical of natural samples. At small test distances, there are no crystals in the calculation. The L' function gives $-r$ for this region, and the PCF is undefined (here shown as a value of zero). These regions represent extreme ordering. The values for the L'-function and the PCF are high when the examination region first includes the twelve neighbors nearest to each crystal, and are periodic as the test distance increases, causing the examination region to encounter each "shell" of crystals followed by the empty region surrounding that shell. The low or undefined values at small r, together with periodic nature of the functions, distinguish these ordered simulations from the interface-controlled envelope simulations shown in Figure 1B.1. Because the radii are random, the MCF

gives a nearly constant and uninformative value; the positive excursion at ~7 mean radii is random noise accentuated by the sparsity of crystals at that separation.

Case IIb: Ordered simulation with random "noise".

To examine the sensitivity of the statistics to ordering effects, a number of simulations were performed using the above parameters, but displacing the crystals by an increasingly large vector in a random direction. The crystals were prevented from overlapping too much as dictated by the interface-controlled growth criterion (see Appendix 1A). As can be seen in Figure 1B.3, the ordering trends in the data can be observed even after perturbing all the crystals by about half the original mean nearest-neighbor distance, 0.06 cm (this is also near the value of the mean nearest-neighbor distance in the perturbed array).

Cases IIIa-e: Clustered simulations.

One of the strengths of correlation-function statistics is their ability to identify ordering and clustering that occur together but at different scales. Geologically, this might correspond to clustering at large scales induced by compositional layering (or other heterogeneities that affect the locations of potential nucleation sites), on which is superimposed shorter-range ordering induced by diffusional controls on crystallization. In order to determine the reliability and sensitivity of the correlation functions in such circumstances, simulations that combine clusters, ordering and randomness have been produced and analyzed. (Here and in the discussion below, clustering is discussed in the context of compositional layering, although the clustering in the simulations and figures is spherical for mathematical tractability. Because the examination regions are spherical and the imposed clustering is spherical, the trends observed in the data are likely to be more pronounced than those observed for layered samples. Still, the conclusions drawn from the data do not strictly rely on the spherical nature of the clusters, and will also apply to porphyroblasts that occur in layers or other kinds of clusters.)

Case IIIa: Ordered clusters, random within.

A simulation of ordered clusters made up of randomly disposed crystals was analyzed (Fig. 1B.4). This might correspond to interface-controlled growth in a highly layered sample, in which the layering was periodic. Although the distribution is random at small scales (within the clusters), the crystal number density within each cluster is greater than would be found if the complete distribution were random, and therefore at scales smaller than the clustering, the L'-function and PCF encounter more crystals than in the interface-controlled envelope simulations. Thus the values of these function lie above the interface-controlled

envelopes. At test distances near the cluster radius (= 5.5 mean crystal radii), we begin to observe in the PCF the effects of ordering in the locations of the clusters.

Case IIIb: Random clusters, random within.

Functional values for a simulation of randomly disposed clusters, each of which is made up of randomly disposed crystals, are given in Figure 1B.5. This might correspond to interface-controlled growth in a highly layered sample, in which the layering was random. As expected, the data show the strong clustering present in the simulation. The ordering signal at distances greater than about ten mean radii is due to the relative sparsity of crystals at scales greater than that of a cluster; because the statistics are normalized to the bulk crystal number density, then just as within a cluster the local crystal number density is higher than the bulk value, leading to a positive excursion outside the envelope, so outside clusters the local crystal number density is lower than the bulk value, leading to a negative excursion outside the envelope.

Case IIIc: Ordered clusters, ordered within.

Figure 1B.6 presents functional values for a simulation of ordered clusters made up of ordered crystals. This might correspond to diffusion-controlled growth in a highly layered sample, in which the layering was periodic. At small test distances, up to that of the nearest-neighbor separation, ordering effects are observed. In this region, the functions take on their minimum values, zero for the PCF and $-r$ for the L'-function, because they encounter zero crystals separated by these distances. At intermediate distances, the clustering is observed in the data, shown most strongly by the L'-function. At scales near half the inter-cluster separation, ordering is again observed in the PCF, reflecting the larger-scale ordering in the data. As the scale of measurement expands to include the neighboring cluster, clustering is again observed in the data. Thus we observe in this crystal array different types of distribution at three different scales.

Case IIId: Random clusters, ordered within.

Functional values for a simulation of randomly disposed clusters made up of ordered crystals are plotted in Figure 1B.7. This might correspond to diffusion-controlled growth in a highly layered sample, in which the layering was random. At the smallest test distances, smaller than the nearest-neighbor separation, we find ordering, as expected. At the nearest-neighbor separation, the positive excursion reflects the incorporation of the first nearest neighbors, and the periodicity that is present at greater test distances reflects the successive "shells" of neighbors at greater separations. The clustering effects are partially obscured by the existence of multiple clusters in contact, as can be observed in Figure 1B.7a, but are evident in the L'

1-58

function, whose gradual decline from about 0.20 cm to the mean nearest cluster neighbor distance at about 0.32 cm displays the clustering signature.

Case IIIe: Random clusters, ordered within, random "noise".

To examine the sensitivity of the statistics to ordering and clustering effects, a number of simulations were performed, displacing the crystals in the simulation with the parameters listed in the preceding paragraph by increasingly large vectors in a random direction. As can be seen in Figure 1B.8, the ordering trends in the data can still be detected after displacing the crystals by about 10 percent of the original nearest-neighbor distance. This is much smaller than the perturbation allowed in the similar case lacking clustering, case IIa above, emphasizing the negative effects inflicted by clustering on the ability to extract useful statistical conclusions from samples.
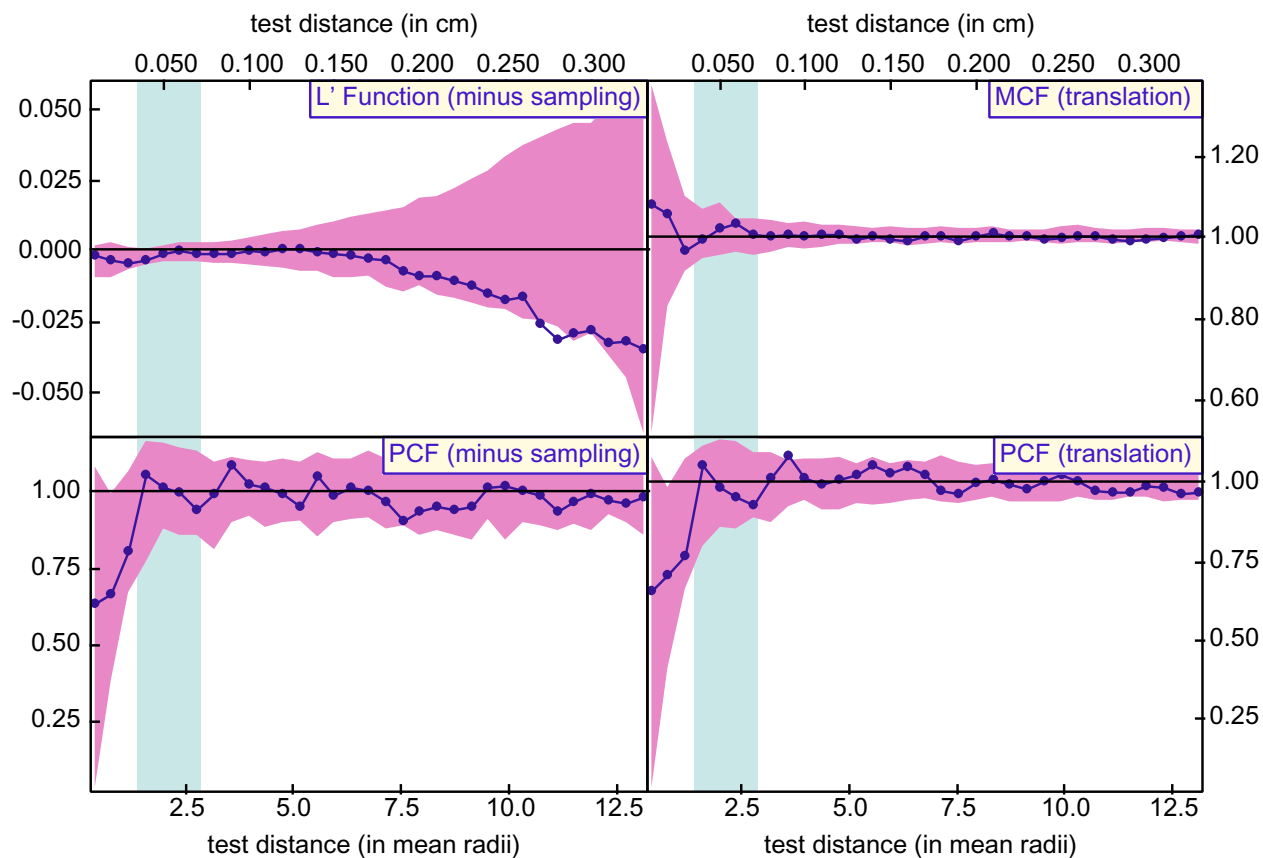
Figure 1B.1. Correlation functions measured on a random array of 1000 crystals. Maximum overlap between crystals is given by the interface-controlled growth criterion. Radii are random over the interval [0, 0.05 cm]. Sample volume is 1 cm^3. The data fall within the 2-σ envelope, as expected.
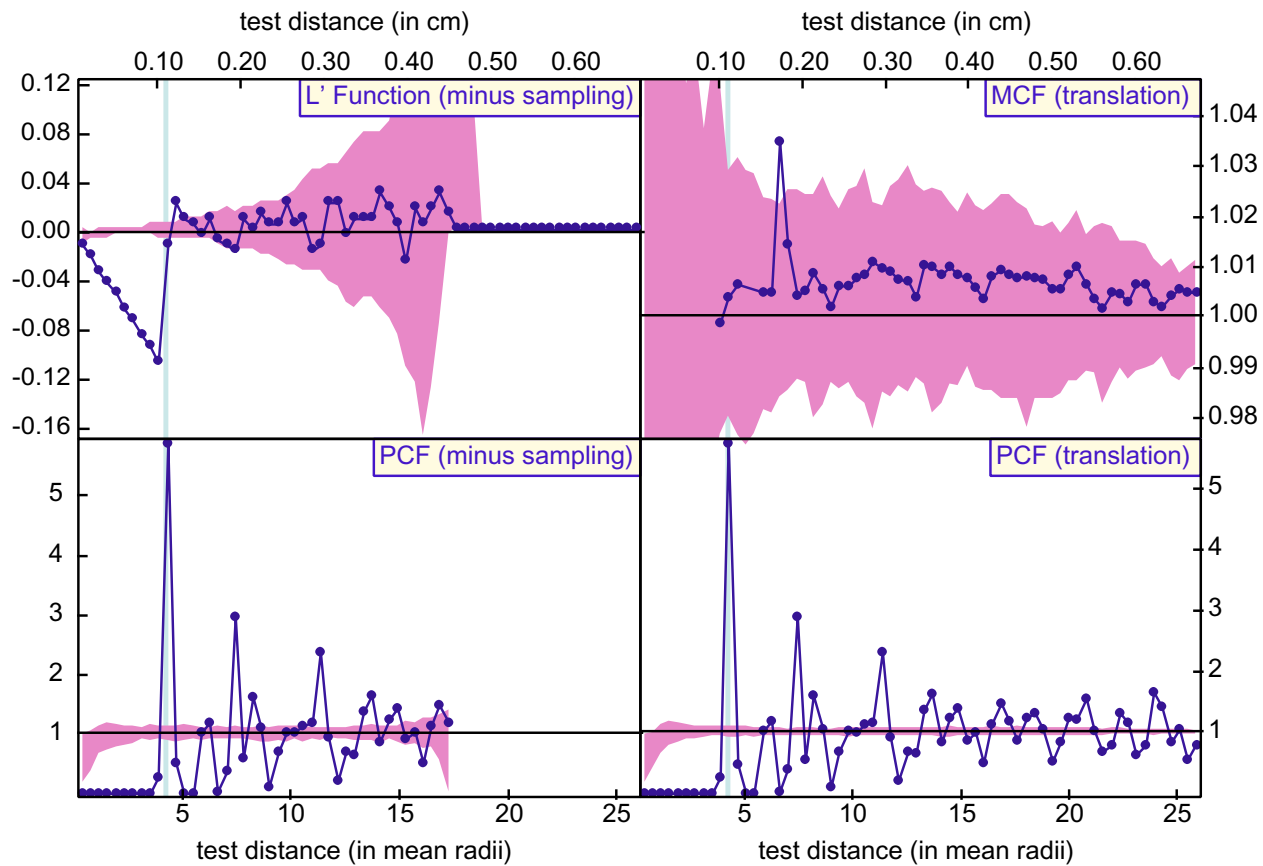
Figure 1B.2. Correlation functions measured on an ordered array of 938 crystals. Crystal locations are dictated by hexagonal closest packing, with random offsets of 0.001 cm. Maximum overlap between crystals is given by the interface-controlled growth criterion. Radii are random over the interval [0, 0.05 cm]. Sample volume is 1 cm^3. The data show strong negative excursions outside the 2-σ envelopes, except at scales of the first, second, . . . , nth nearest neighbors.
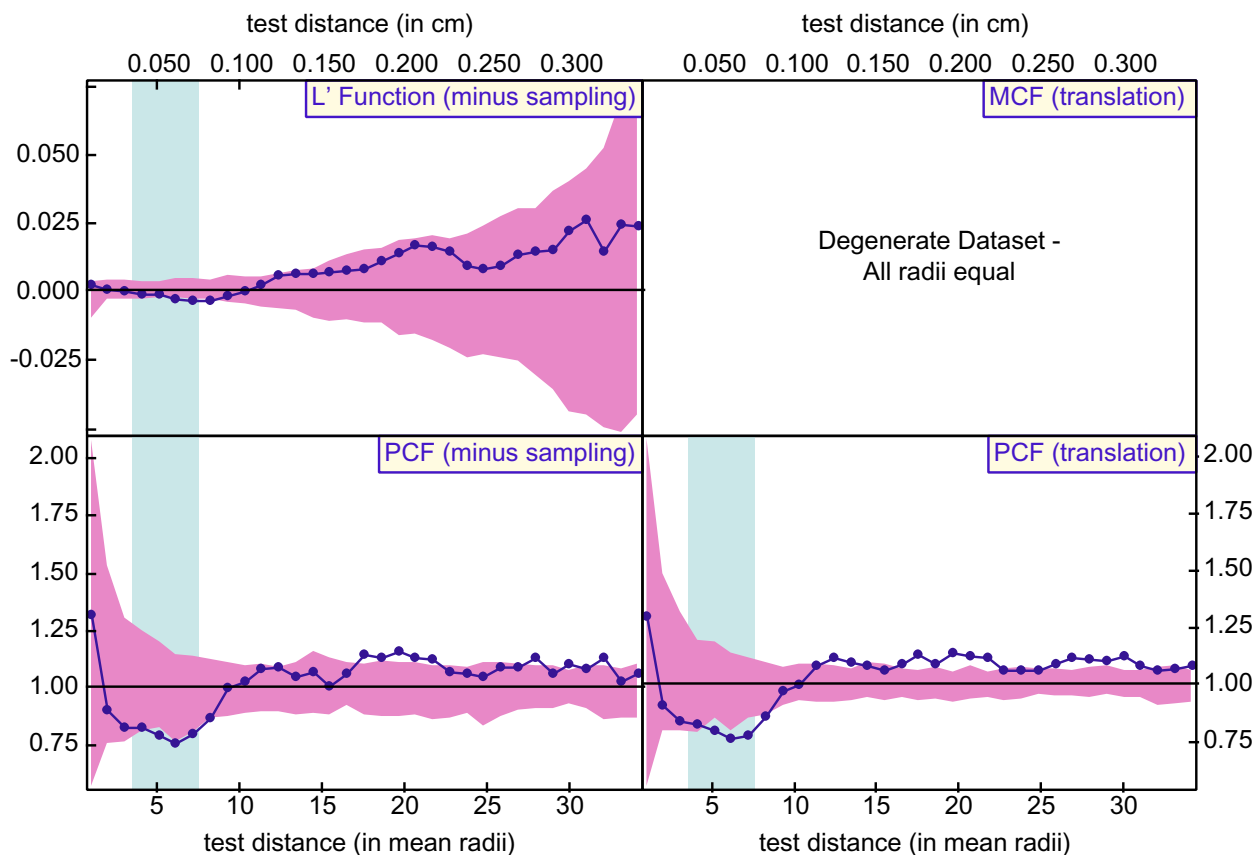
Figure 1B.3. Correlation functions measured on the crystal array of Figure 1B.2, but with each crystal displaced by a distance of 0.06 cm in a random direction in order to obscure the ordering signal, continue to show ordering effects at the scale of about the mean nearest-neighbor distance. In this model, all crystals have the same radius, so the MCF is degenerate.
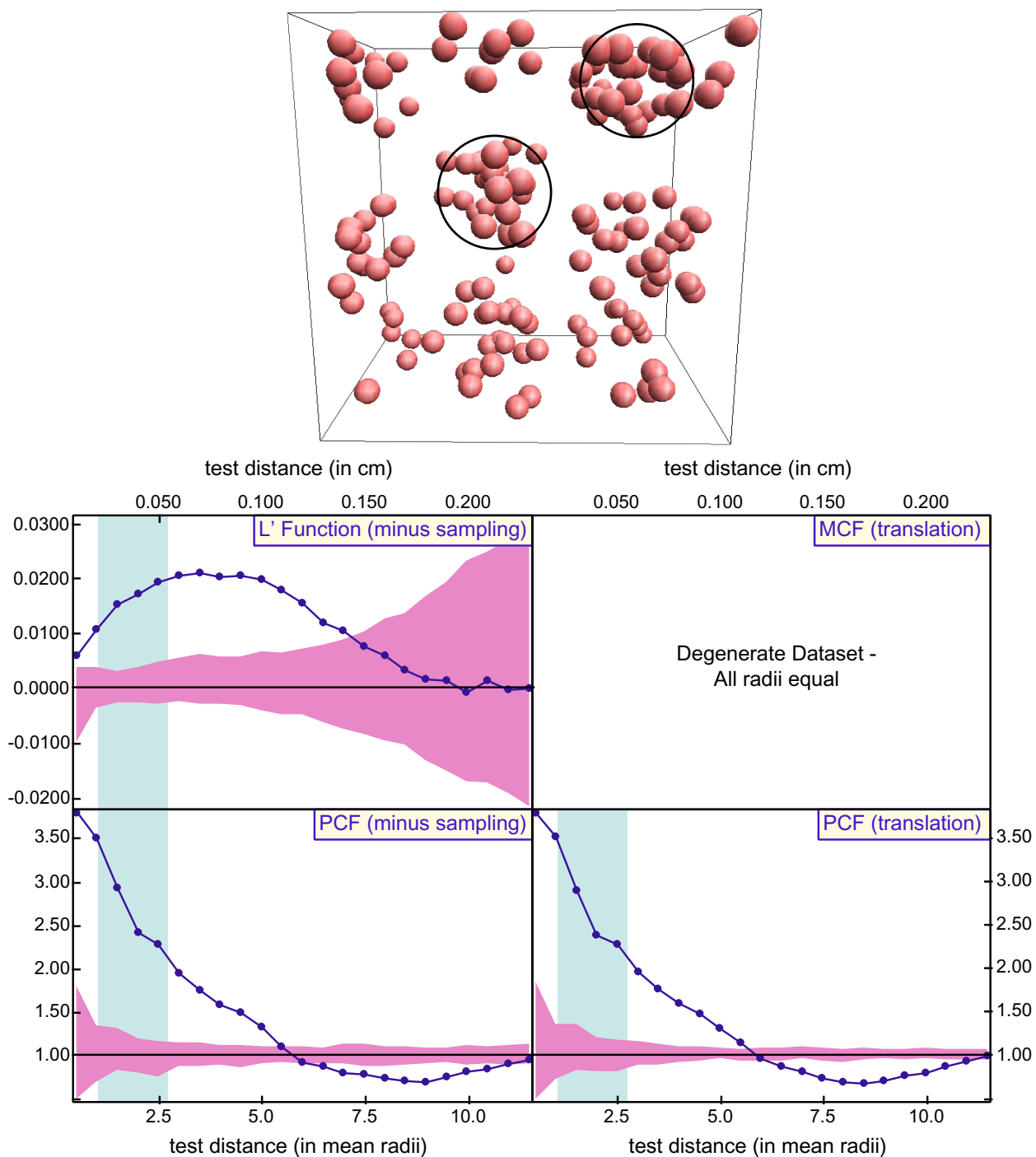
Figure 1B.4. (a) Rendering of sub-volume of clustered simulation in which cluster centers are ordered using hexagonal closest packing, and crystal locations are random within each cluster; two clusters are circled. Cluster radii are 0.11 cm, with a center-to-center separation of 0.3 cm. There are 20 crystals per cluster. Crystal radii are all 0.02 cm (making the MCF degenerate). Sample volume is 1 cm^3. (b) Correlation functions measured on a clustered array of 980 crystals. Strong positive excursions outside the envelopes reflect the clustering of the crystals in the array, with the PCF showing ordering near the scale of the cluster radius (5.5 mean radii).
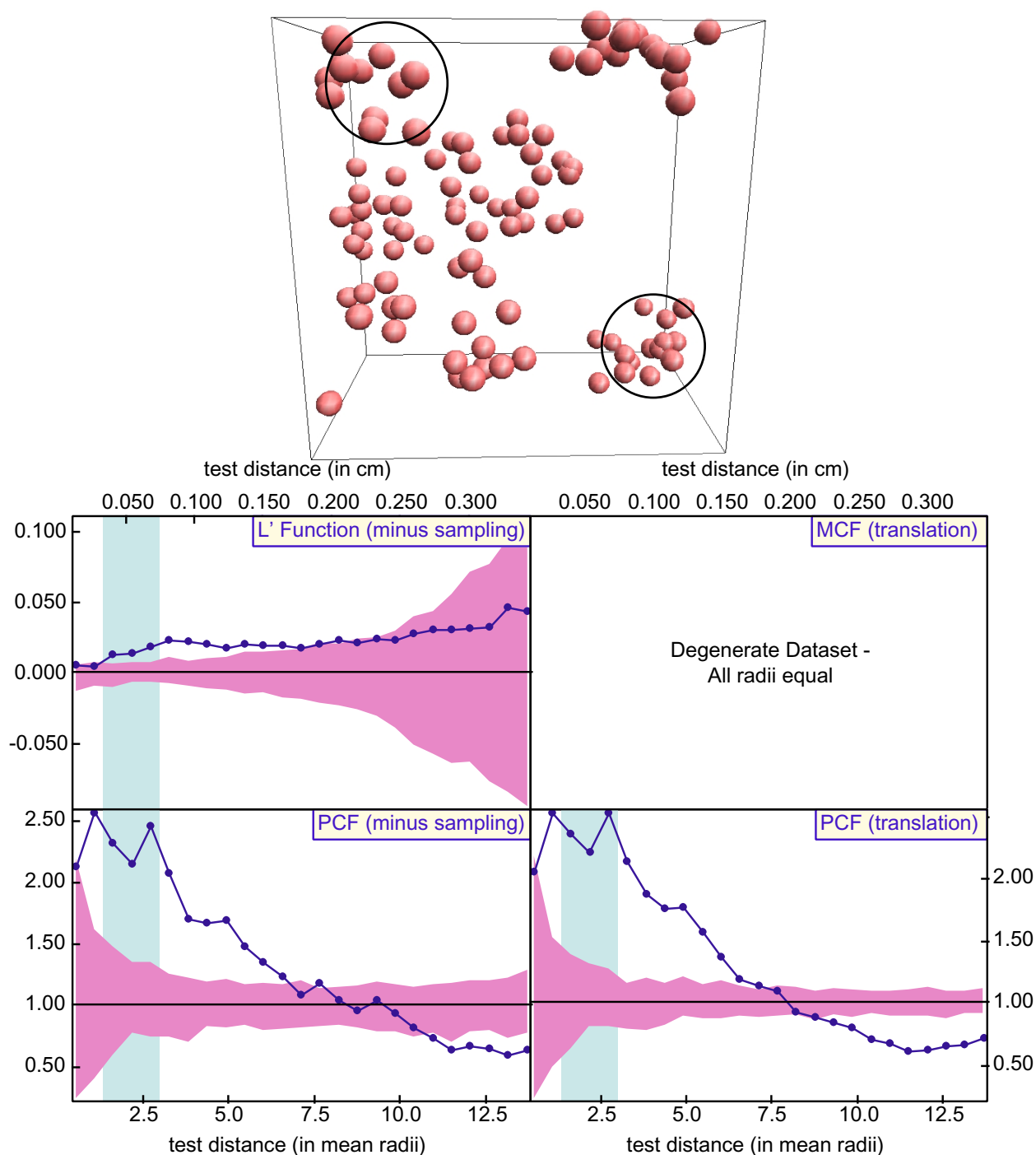
Figure 1B.5. (a) Rendering of sub-volume of clustered simulation in which cluster centers are randomly disposed, as are crystal locations within each cluster; two clusters are circled. Cluster radii are 0.18 cm, and there are 20 clusters and 30 crystals per cluster. Crystal radii are all 0.025 cm (making the MCF degenerate). Sample volume is 1 cm^3. (b) Correlation functions measured on a clustered array of 388 crystals. Strong positive excursions outside the envelopes reflect the clustering of the crystals in the array, and the negative excursion in the PCF at large test distances reflects the sparsity of crystals outside a cluster relative to the mean crystal density.
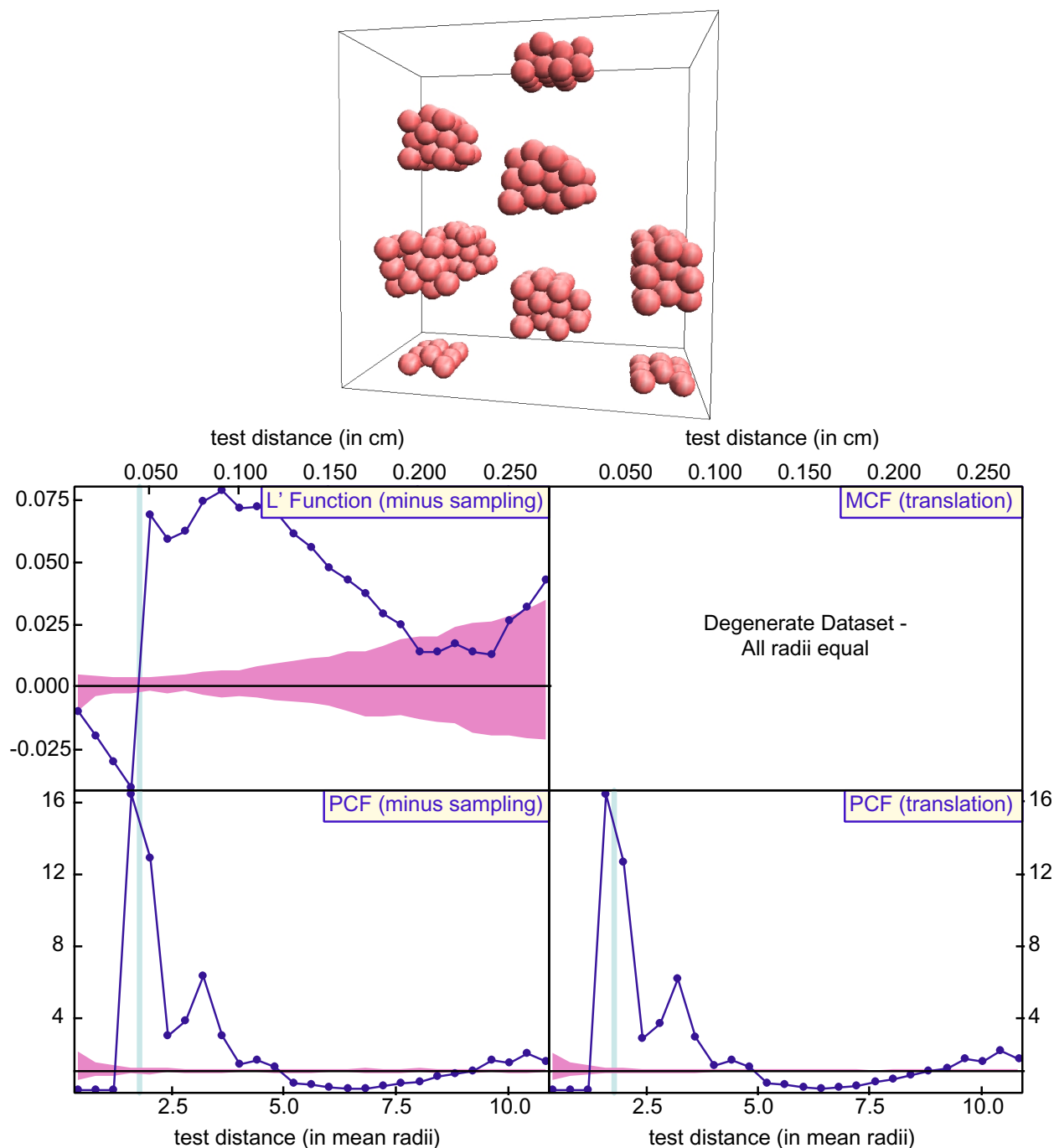
Figure 1B.6. (a) Rendering of sub-volume of clustered simulation in which cluster centers are ordered using hexagonal closest packing, as are crystal locations within each cluster; there are 30 crystals per cluster. Cluster radii are 0.08 cm and center-to-center separation is 0.3 cm. Crystal radii are all 0.025 cm (making the MCF degenerate). Sample volume is 1 cm^3. (b) Correlation functions measured on a clustered array of 987 crystals. The data show alternating excursions below and above the 2-σ envelope; at the smallest scales of measurement, the excursion is below the envelope. This pattern reflects first the small-scale ordering within the clusters (below), then the clustering (above), then the space between the clusters (below) then the nearest neighboring cluster (above), and so on.
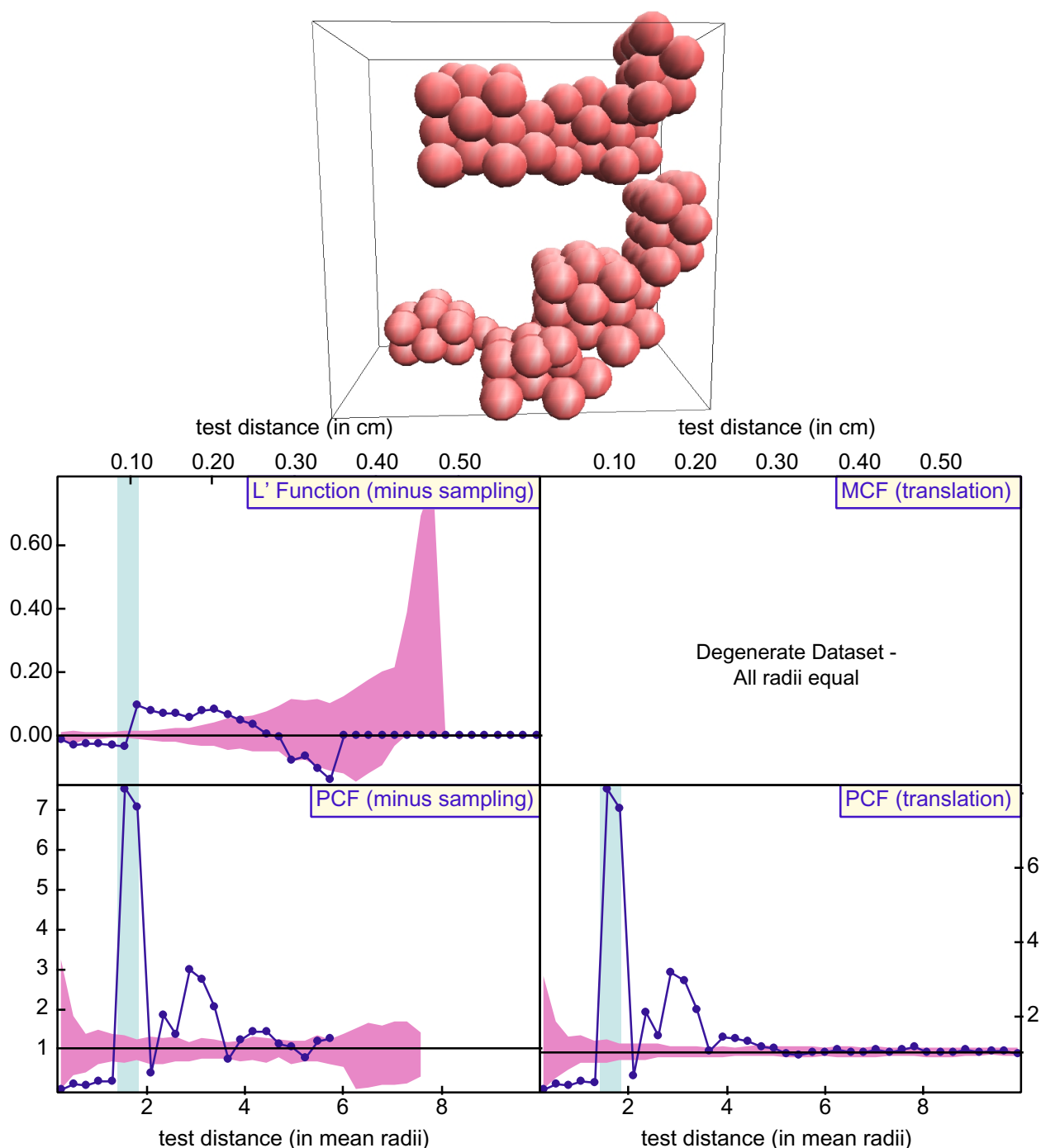
Figure 1B.7. (a) Rendering of sub-volume of clustered simulation in which cluster centers are randomly disposed, and crystal locations are ordered within each cluster using hexagonal closest packing; there are 12 clusters, and 30 crystals per cluster. Cluster radii are 0.18 cm, and crystal radii are all 0.06 cm (making the MCF degenerate). Sample volume is 1 cm^3. (b) Results of correlation functions measured on a clustered array of 260 crystals. The strong positive excursion in the PCF reflects the inclusion of the first nearest neighbor in the calculation, the negative excursion reflects the absence of crystals separated by distances slightly greater than the nearest neighbor distance, the next positive excursion reflects the second nearest neighbor, and so on.
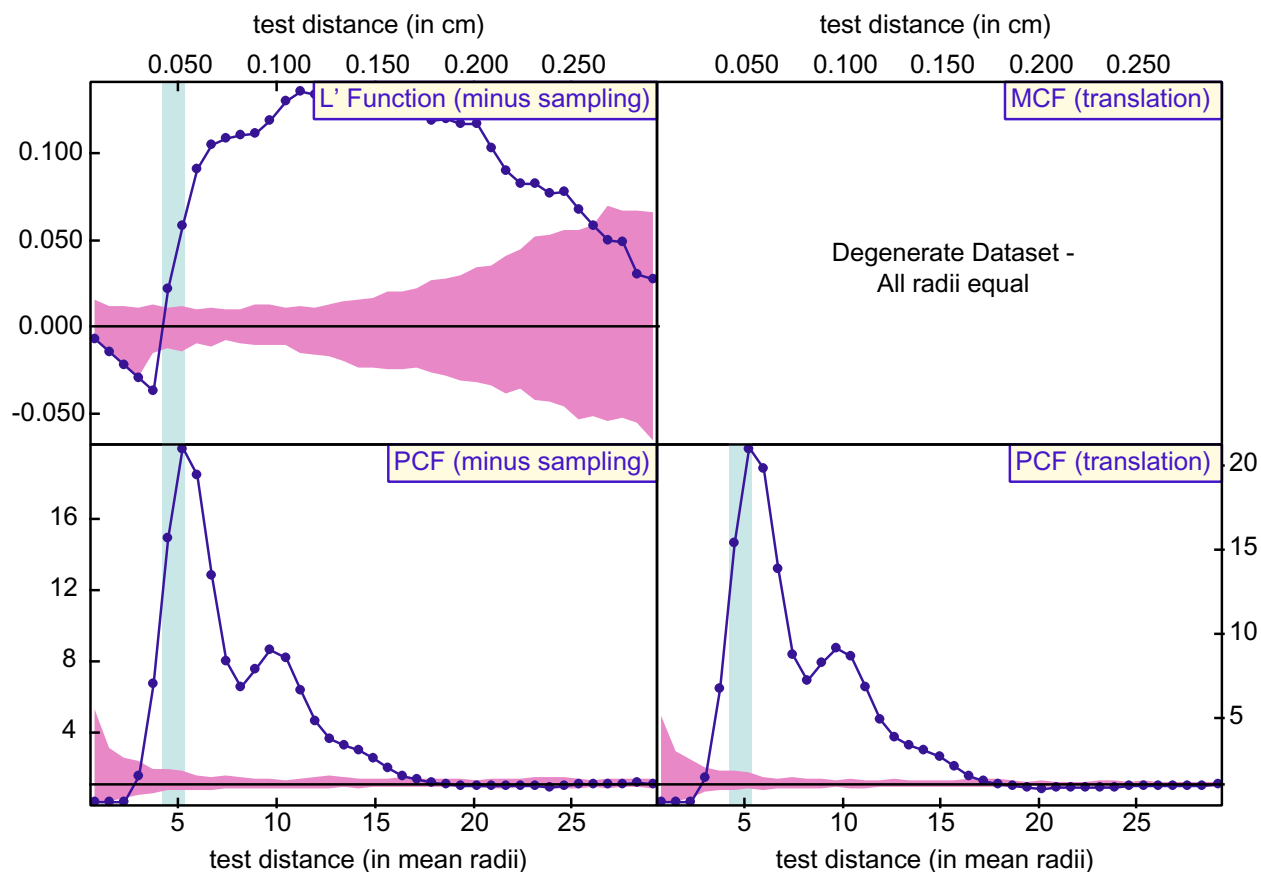
Figure 1B.8. Correlation functions measured on the crystal array of Figure 1B.7, but with each crystal displaced by 0.01 cm in order to obscure the ordering/clustering signal. The data continue to show the same basic pattern, with small-scale ordering within larger-scale clustering. The small-scale ordering is demonstrated not only by the single point in the L' -function that falls below the envelope, but also by the fact that at the smallest scales, both the L' -function and the PCF take on theit smallest possible values, indicating that there were no crystals observed at that separation.

APPENDIX 1C. TESTS OF ROBUSTNESS OF CORRELATION FUNCTIONS

Denison *et al*. (1997, Appendix 1) describe limitations on sample characteristics for three single-valued statistics: the ordering index, clustering index, and impingement index. They conclude that because of edge effects, a minimum of 1000 crystals is necessary to obtain reliable values for these statistics. A similar set of analyses was performed to evaluate appropriate sample sizes for application of correlation-function statistics.

Numbers of crystals

In order to determine the sensitivity of correlation functions to low crystal numbers, outer portions of the diffusion-controlled simulation shown in Figure 1.12 were progressively removed, and the resulting data repeatedly analyzed to determine at what amount of reduction the diffusional effects were no longer reliably observable. Because the locations and sizes of the crystals in the interior are controlled by the same factors as those near the edges that were removed, the value of the statistics would be expected to remain constant, although the noise should increase.

The results for this type of analysis are shown in Figure 1C.1. They show that the arrays may be reduced to a small fraction of the original number of crystals without changing the conclusion reached by the statistical analysis using correlation functions. In the results shown, the number of crystals is reduced from 2971 to 184 without loss of the diffusion-control signal. Further reduction in the number of crystals leads to a different conclusion, or the data degenerates too far to be usable. This finding suggests that reliable results may be obtained from data sets as small as a few hundred crystals, although greater crystal numbers will greatly strengthen the confidence that can be placed in the inferences drawn.

Aspect ratios

A similar set of analyses was performed to examine the sensitivity to sample aspect ratio, which determines the magnitude of the edge effects: in this case, rather than the outer 10% of the sample being removed, only the top 10% was removed in successive calculations.

The results from this analysis (Fig. 1C.2) are also encouraging: for the results shown, the number of crystals is reduced from 2971 to 310, and the sample aspect ratio increased from 1:1:1 to 1:10:10 without loss of the diffusion-control signal. Further reduction in the number of crystals, or increase in the aspect ratio, leads to a different conclusion, or the data degenerates too far to be usable.

It is important to note that these results are obtained with simulations, which have no complicating factors that may be found in real rocks, such as inhomogeneity of nucleation sites or nutrients for crystal growth. These factors may introduce enough noise into the data that at small numbers of crystals or large aspect ratios, any diffusion-controlled signal that may be present will be obscured.
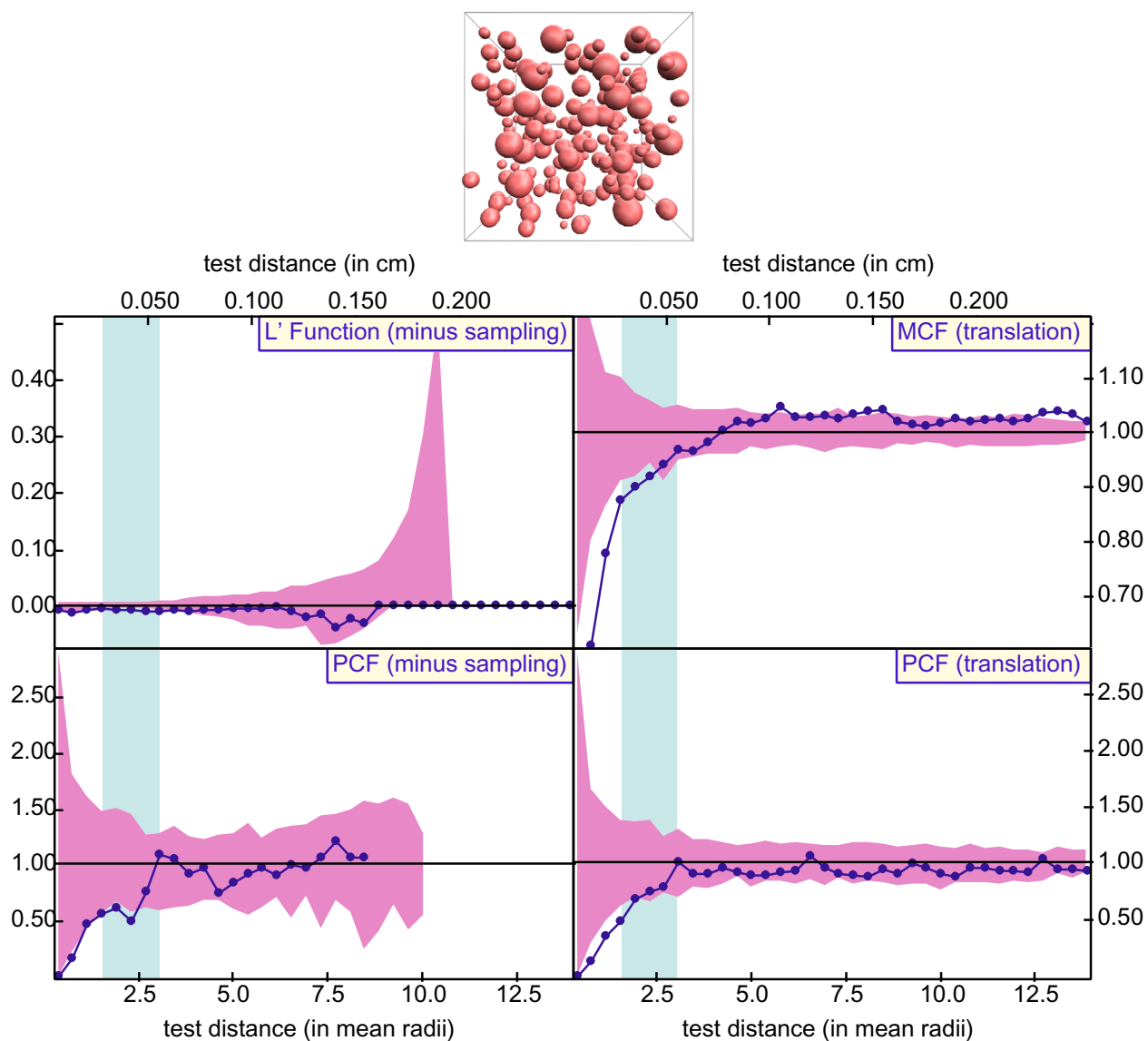
Figure 1C.1. (a) Rendering of final remaining volume in DC-1; cube edge is 0.4 cm. (b) Correlation functions measured on remaining volume after removing outer crystals. DC-1 has 184 crystals remaining, yet the diffusional-control conclusion is still clear from the data.
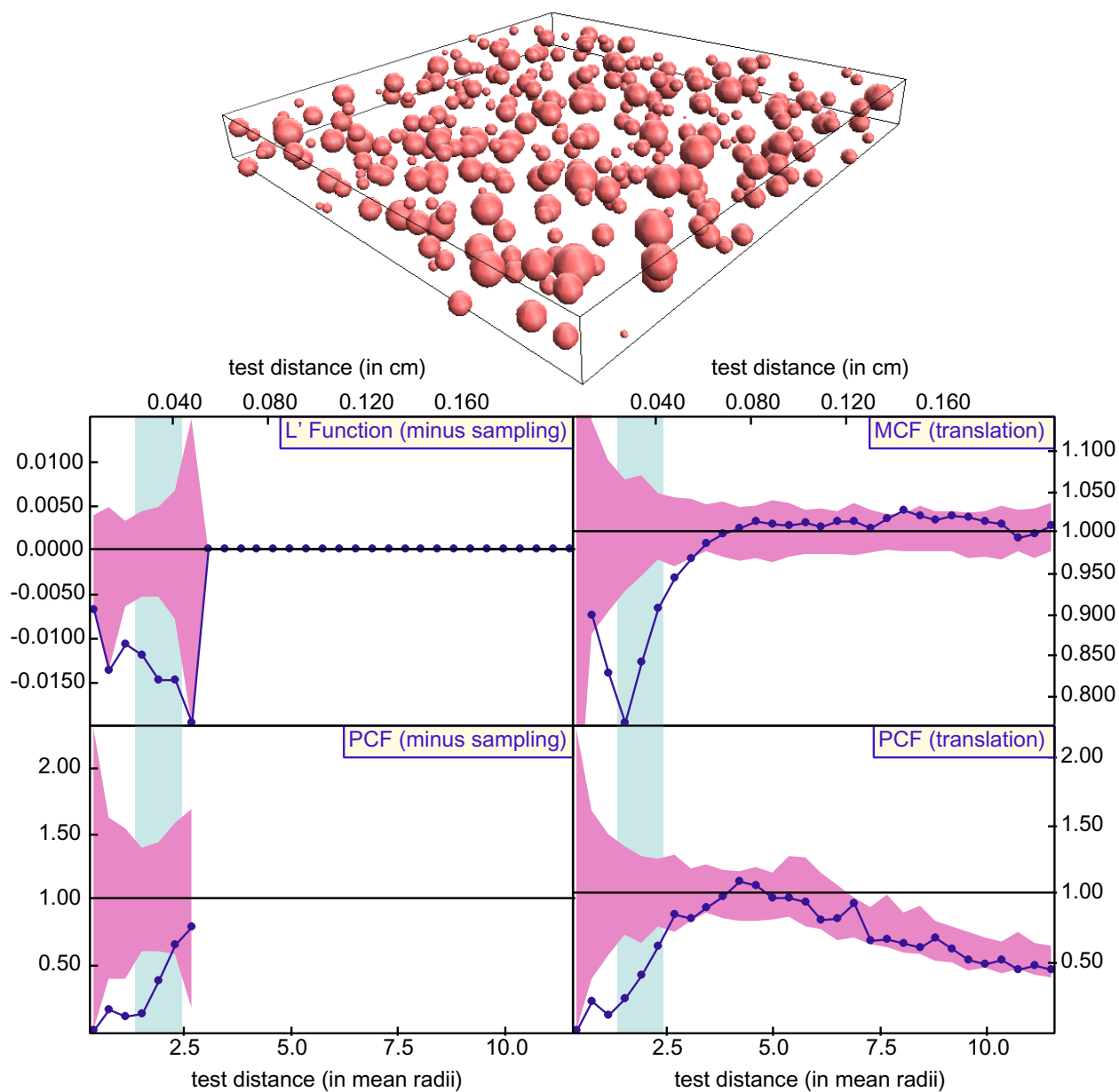
Figure 1C.2. (a) Rendering of remaining volume in simulation DC-1. Vertical dimension is 0.1 cm while both horizontal dimensions are 1.0 cm. (b) Correlation functions measured on remaining volume after removing crystals from the top of simulation DC-1. DC-1 has 310 crystals remaining, yet the diffusional-control conclusion is still clear from the data.

Chapter 2. Refutation of the Multiple Nucleation Hypothesis for Garnet Growth using Electron Beam Techniques

ABSTRACT

Orientation contrast imaging (OCI) and quantitative crystallographic orientation measurements from electron backscatter patterns (EBSP) have provided a rigorous test of a recently published model for the nucleation and growth of garnet crystals from Harpswell Neck, Maine that requires multiple nucleation and coalescence for each crystal. OCI reveals only two crystallographic misorientations within the eight garnet porphyroblasts that were examined. In one of these, the misorientation is less than 1°, and is interpreted as the result of subgrain formation. In the other instance of misorientation, a significant angular difference exists between the orientations of the two domains within the crystal, and EBSP data show that the two domains in that sample share a crystallographic axis. This suggests the domains are crystallographically related, probably by a twin operation. The misorientation boundaries are both sector-shaped in outline.

The crystallographic data do not support the model of multiple nucleation and coalescence previously suggested on the basis of dispersed high-Mn regions within garnet porphyroblasts. An alternative explanation invokes a model for the disequilibrium growth of garnet, in which phases rich in Mn are overgrown, incorporating their Mn locally into the garnet structure. Although this model requires previously undocumented disequilibrium for Fe, Mg, and Mn during the early stages of garnet growth, that inference is consistent with the very low temperatures of garnet nucleation in these rocks, and with the compositional evidence for increasingly large scales of equilibrium as reaction progressed.

INTRODUCTION

Garnet compositional zoning patterns have been studied for over thirty years, with important early work by Hollister (1966). Later work has expanded our knowledge and understanding of these zoning patterns, and presented models to explain their development during growth and possible subsequent modification (Loomis, 1975; Tracy et al., 1976; Trzcienski, 1977; Woodsworth, 1977; Yardley, 1977; Tracy, 1982; Spear et al., 1990; Chernoff and Carlson, 1997, 1999). The typical garnet zoning pattern found in pelitic schists metamorphosed to peak temperatures of 450-550°C is, from core to rim, decreasing Mn and Ca and increasing Mg and Fe. These compositional variations are believed to reflect a combination of changing availability of these elements to the surface of the growing garnet, and changing partitioning of elements among the phases in the rock. Element availability is controlled by cumulative garnet growth, and partitioning is controlled by intensive factors such as temperature and pressure. This growth zoning model requires the matrix to be in chemical equilibrium with the garnet surface, with the composition of precursor minerals altering to remain in equilibrium as the garnet draws out Mn and Ca, and leaves the rock enriched in Mg and Fe.

Daniel and Spear (1998) and Spear and Daniel (1998) documented zoning patterns within spessartine-rich garnet-zone garnet from Harpswell Neck, Maine, U.S.A that were more complex than those described above. These garnets were notable in that three-dimensional maps of divalent cation distribution revealed irregularly zoned cores with isolated regions of high spessartine content. Daniel and Spear (1998) interpreted the isolated Mn-highs to represent early nuclei that subsequently coalesced to form a single garnet porphyroblast. This model makes the testable prediction that the early-formed separated nuclei should bear no crystallographic relationship to one another, so that the garnet porphyroblast should be composed of random crystallographic domains whose boundaries coincide with low-Mn surfaces.

To test this model of garnet growth, samples were collected by W. Carlson from the locality of Lang and Dunn (1990) given in Daniel and Spear (1998), and two were sent to Dr. David Prior at the University of Liverpool for crystallographic analysis. He applied two complementary electron beam techniques, Orientation Contrast Imaging (OCI) and Electron Backscatter Pattern (EBSP) data, to examine the garnets for crystallographic boundaries and to measure any angular misorientations across the boundaries. We present data for eight garnet crystals from two samples.

Two techniques were used to obtain information on crystallographic orientation in sections through garnet crystals: Orientation Contrast Imaging (OCI), which permits the identification of boundaries between crystallographic domains having angular differences of as small as 1° or less, and Electron Backscatter Pattern (EBSP) data, which allows measurement of the crystallographic orientation of the part of the garnet crystal under the electron beam. These techniques both rely upon the phenomenon of electron channeling and have been fully described in Lloyd (1987), Randle (1992), and Prior *et al.* (1996).

The Orientation Contrast and Electron Backscatter Pattern images were obtained by Dr. David Prior at the University of Liverpool Department of Geology using a Phillips SEM with operating conditions of 20kV and ~0.8 nA on an uncoated surface. Although they were tilt-corrected using software in the Phillips operating system, some distortion remains in the OC images.

Sample preparation for these techniques is quite important. Following production of a standard probe-polished thin section, a final chemical-mechanical polishing with Syton fluid on a polyurethane lap is performed in order to remove any structural damage produced during the main polishing from the surface of the garnet. This is necessary, as the electron-lattice interaction that produces the OC and EBSP data requires undisturbed crystal lattice at the surface, rather than the semi-amorphous material normally present in the surface layers following mechanical polishing.

Orientation contrast imaging (OCI)

Although the number of electrons backscattered from an incoming beam of electrons is primarily linked to the mean atomic number of the material under the beam, a small fraction may be lost or "channeled" into the crystal lattice (Lloyd, 1987). This fraction will be linked to the angle between the beam and the lattice planes, and so, if the variation in this portion of the signal can be detected, angular differences in the lattice can be discerned and imaged. This fraction in a standard-configuration SEM is difficult to detect and is overwhelmed by the atomic number signal, but a novel beam-sample-detector arrangement (Figs. 2.1 and 2.2) has allowed the acquisition of images in which the electron-channeling signal is of approximately the same strength as the atomic-number signal (Prior et al., 1996).

The orientation contrast images display variations in grayscale linked to angular variations, but not in a systematic way. Angular variations as small as 1° or less may be detected, but grayscale variations are also sensitive to the relative positions of sample, beam, and detector. In any particular combination of positions,

some misorientation boundaries will be missed, and so it may require as many as six OC images, each collected under a different geometry, to detect most of the misorientation boundaries present in a sample (Prior et al., 1996).

Electron backscatter patterns (EBSP)

Identification of the crystallographic orientation of the garnet material under the electron beam is performed using the electron backscatter technique (Lloyd, 1987). This method uses a beam that "rocks" about a point on the sample, changing its angle of incidence to produce what has been variously termed an electron-channeling pattern, electron-backscatter pattern, or Kikuchi pattern. Figure 2.2 shows the configuration of beam, sample, and EBSP camera for this technique. The camera records the EBSP on its phosphor screen and the image is then digitized for further processing. Two electron channeling patterns with different orientations are shown in Figure 2.3. This technique can generally resolve angular differences as small as approximately 1°.

X-ray compositional maps and image processing

Compositional data were collected by D. Hirsch, with a JEOL 733 Superprobe located in the Department of Geological Sciences, The University of Texas at Austin. Data were collected at 15 kV accelerating voltage; sample current on brass varied among the maps between 300 – 700 nA, as did the dwell time, which ranged between 20 – 40 ms/pixel. Pixel resolution varies from 2 μm x 2 μm to 4 μm x 4 μm. All X-ray maps were processed with a 3 x 3 averaging kernel that incorporates edge detection to eliminate the averaging of non-garnet pixels.[1]

RESULTS

Compositional zoning maps

Almandine (Alm), pyrope (Prp), spessartine (Sps), and grossular (Grs) zoning patterns for nine garnet crystals taken from two samples are shown in Figures 2.4 through 2.7. In the crystals shown, the contours of Alm and Pyp generally increase from core to rim, while Sps and Grs decrease from core to rim. In detail,

---

[1] This method is not necessarily free from artifacts related to inclusion density. Although pixels that are wholly analyses of inclusions will be excluded from the analysis, many pixels will be analyses whose excitation volumes are partially garnet and partially inclusion, especially for inclusions whose sizes are smaller than the pixel size. In this case, these pixels will tend to have lower grayscale values. For dispersed inclusions smaller than the pixel size, the effect in a Mn compositional X-ray map will be a region of low Mn composition, as is frequently observed in our data in zones of high inclusion density. This effect can be observed in sample HN98-1-4, Garnet D, in which two high-Mn regions are separated by an inclusion-rich low-Mn region. It is unclear whether this intervening region actually has lower values of the spessartine component, or whether this is an artifact induced by a very high inclusion density.

however, those patterns do not hold for Alm, Pyp, and Sps, which tend to be irregular in the cores rather than varying smoothly from core to rim. In particular, there are regions of relatively high X_{Sps} that are separated by regions of lower X_{Sps}.

In the garnets shown, Ca zoning tends to be more concentric and shows a narrow increase near the rim and then continues to decrease at the rim. In the garnet cores, Grs contours are discordant from Alm, Prp, and Sps, but become more concordant near the rim.

OCI & EBSP data and interpretations

Orientation contrast images for sample HN98-1-3 reveal that, of the three garnets examined, one (garnet B) shows no crystallographic variation, one (garnet C) is clearly the result of impingement of two large garnets, and one (garnet A) shows two crystallographic domains in a single garnet. The OCI and EBSP data for garnet B provide no information, and are here omitted. Results from the crystallographic analysis of garnet A are more interesting (Fig. 2.4); this crystal has two domains, labeled "A" and "B," with the boundary between them displaying a roughly sector morphology. Five ESBP analyses were obtained across this boundary (Fig. 2.4c). These EBSP data show that the two domains share an (001) axis and are misoriented by 44°.

Crystallographic data for garnet C from sample HN98-1-3 (Fig. 2.5) reveals a significant misorientation boundary within a low-Mn region, just as the multiple nucleation hypothesis predicts. However, this misorientation boundary overlays a grain boundary clearly visible in BSE view, presented in Fig. 2.5c. Figure 2.5d presents EBSP data showing that the domains bear no crystallographic relationship to each other, and are misoriented by ~33°.

In sample HN98-1-4, six garnets were examined, five of which (garnets C-G) revealed no crystallographic variations. The single garnet that shows an angular misorientation is garnet B (Fig. 2.6); two crystallographic domains can be identified in the OC images, again showing a marked sector morphology, with sub-radial boundaries forming an angle of roughly 120°. The EBSP analyses performed on these domains (Fig 2.6c) reveal that the misorientation is very small – on the order of 1°. Although the location of this boundary is near the low-Mn region shown in the compositional map (Fig. 2.6a), as would be expected for the coalescence hypothesis of Daniel and Spear (1998) and Spear and Daniel (1998), other dispersed high-Mn regions do not correspond to crystallographic boundaries.

DISCUSSION

No significant correlation exists between the crystals' zoning patterns and large misorientation boundaries observed in the crystallographic data. For garnet A, sample HN–98–1–3 (Fig. 2.4), the sharing by two domains of a common crystallographic axis strongly implies that they are related by a crystallographic operator. These angular relationships have been observed in sector-twinned garnets, and are likely a growth feature (D. Prior, pers. comm). We thus interpret this misorientation as a twin boundary.

Crystallographic data for garnet C from sample HN98-1-3 (Fig. 2.5) can also shed light on the multiple nucleation hypothesis, by showing what type of results impinged garnets should provide. Although this boundary does correspond to a low-X_{Sps} region, and the domains are randomly oriented with respect to each other, coalescence preserves a visible grain boundary between the two crystals. A garnet made up of multiple nuclei, we conclude, would be likely to retain traces of internal grain boundaries.

Although in garnet B, sample HN98-1-4 (Fig. 2.6) the low-Mn region is near the boundary between the two crystallographic domains, as predicted by the multiple nucleation and coalescence hypothesis, this is likely a coincidence. If these domains represented separate nuclei, one would expect them to have random crystallographic orientations; instead, they have nearly identical crystallographic orientations. This is very unlikely to have occurred by chance if the domains had nucleated separately and impinged. The small angular difference ($< 1°$) across a narrow boundary is very similar to textures observed as in other minerals that are interpreted to be the result of recovery processes, such as tilt walls in quartz that produce discontinuous undulatory extinction. Thus, it is probable that this is a tilt wall (plane of high dislocation density), and the low-Mn region simply happens to occur nearby.

In the HN98-1-4B data, as with other data, the crystallographic domain boundaries tend to be coincident with high densities of inclusions. This would be likely if at least some of the domains are incipient subgrains, bounded by tilt walls, because the dislocations would tend to migrate through the garnet, but be pinned in regions with a high inclusion density that would limit dislocation climb ability. This would tend to favor the development of tilt walls, and therefore crystallographic domain boundaries, in regions of high inclusion density.

PROPOSED GARNET GROWTH MODEL

The results above contrast sharply with those predicted by Daniel and Spear (1998) and Spear and Daniel (1998), and are at odds with the hypothesis of multiple nucleation and coalescence. How, then can these unusual zoning patterns be explained?

The model we propose is one of concentric, disequilibrium growth (Fig. 2.8), in which garnet growth occurred by the addition of radially symmetric shells around the nucleus. It requires that the garnet rim composition (at any given instant in time) will vary depending upon the local bulk composition in contact with that portion of the rim and the relative transport rate of material to and away from the growth surface. For example, a Mn-rich precursor phase that is adjacent to the growing garnet would lead to a high-Mn region within the garnet as the "chemical discontinuity" is incorporated into the crystal structure. This model requires significant disequilibrium at the garnet rim for all elements during garnet growth. In this model the crystallographic misorientations propagate outward during growth from some earlier discontinuity, or are related to recovery processes.

The levels of disequilibrium for Fe, Mg, and Mn during growth of garnet that this model requires have not been observed previously. However, the very low temperatures of this garnet growth (made possible due to the high spessartine content) may provide an explanation. Garnet rim temperatures were between 450-470 °C (Spear and Daniel, 1998), and this should represent the last increment of garnet growth – the onset of garnet growth was likely to have been at significantly lower temperatures. Growth at such low temperatures would rely upon very slow rates of diffusional transport through the intergranular medium, increasing the likelihood of disequilibrium garnet growth.

In fact, the details of the Fe, Mg, and Mn cation maps may support this hypothesis of disequilibrium during low-temperature garnet growth, and may provide evidence for a progressive lengthening of the scale of equilibration over the course of garnet growth. In Figures 2.4 to 2.7, the zoning patterns in the garnet cores are distinctly different from those near the garnet rims. In the cores, the zoning patterns are irregular, and (under this model) record the precursor distribution of Mn-rich phases (possibly chlorite), in accord with a model of growth at a very low temperature leading to a very small scale of equilibration (Fig. 2.8a). Near the rims, garnet was growing later, after the temperature had risen to the point where the scale of equilibration may have been on the order of the dimensions of a single garnet, largely removing evidence of the distribution of precursor phases, forming smoother zoning patterns (Fig. 2.8b). There is also evidence that

during the latest part of garnet growth, equilibration may have reached the hand-sample scale, as the three garnets from sample HN98-1-4 (Fig 2.7 b,c) show the same composition at their rims (Fig. 2.8c).

REFERENCES CITED

Chernoff, C. B. and Carlson, W. D., 1999. Trace element zoning as a record of chemical disequilibrium during garnet growth. *Geology*, **27**, 555-558.

Chernoff, C. B. and Carlson, W. D., 1997. Disequilibrium for Ca during growth of pelitic garnet. *Journal of Metamorphic Geology*, **15**, 421-438.

Daniel, C. G. and Spear, F. S., 1998. Three-dimensional patterns of garnet nucleation and growth. *Geology*, **26**, 503-506.

Hollister, L. S., 1966. Garnet zoning: an interpretation based on the Rayleigh fractionation model. *Science*, **154**, 1647-1651.

Lang, H. M. and Dunn, G. R., 1990. Sequential porphyroblast growth during deformation in a low pressure metamorphic terrain, Orrs Island-Harpswell Neck, Maine. *Journal of Metamorphic Geology*, **8**, 199-216.

Lloyd, G. E., 1987. Atomic number and crystallographic contrast images with the SEM: a review of backscattered electron techniques. *Mineralogical Magazine*, **51**, 3-19.

Loomis, T. P., 1975. Reaction zoning of garnet. *Contributions to Mineralogy and Petrology*, **52**, 285-305.

Prior, D. J., Trimby, P. W., Weber, U. D. and Dingley, D. J., 1996. Orientation contrast imaging of microstructures in rocks using forescatter detectors in the scanning electron microscope. *Mineralogical Magazine*, **60**, 859-869.

Randle, V., 1992. *Microtexture determination and its applications*. The Institute of Materials, London, Pages.

Spear, F. S. and Daniel, C. G., 1998. Three-dimensional imaging of garnet porphyroblast sizes and chemical zoning: Nucleation and growth history in the garnet zone. *Geological Materials Research*, **1**, 1-44.

Spear, F. S., Kohn, M. J., Florence, F. P. and Menard, T., 1990. A model for garnet and plagioclase growth in pelitic schists; implications for thermobarometry and P-T path determinations. *Journal of Metamorphic Geology*, **8**, 683-696.

Tracy, R. J., 1982. Compositional zoning and inclusions in metamorphic minerals. *Reviews in Mineralogy*, **10**, 355-397.

Tracy, R. J., Robinson, P. and Thompson, A. B., 1976. Garnet composition and zoning in the determination of temperature and pressure of metamorphism, central Massachusetts. *American Mineralogist*, **61**, 762-775.

Trzcienski, W. E. J., 1977. Garnet zoning - product of continuous reaction. *Canadian Mineralogist*, **15**, 250-256.

Woodsworth, G. J., 1977. Homogenization of zoned garnets from pelitic schists. *Canadian Mineralogist*, **15**, 230-242.

Yardley, B. W. D., 1977. An empirical study of diffusion in garnet. *American Mineralogist*, **62**, 793-800.
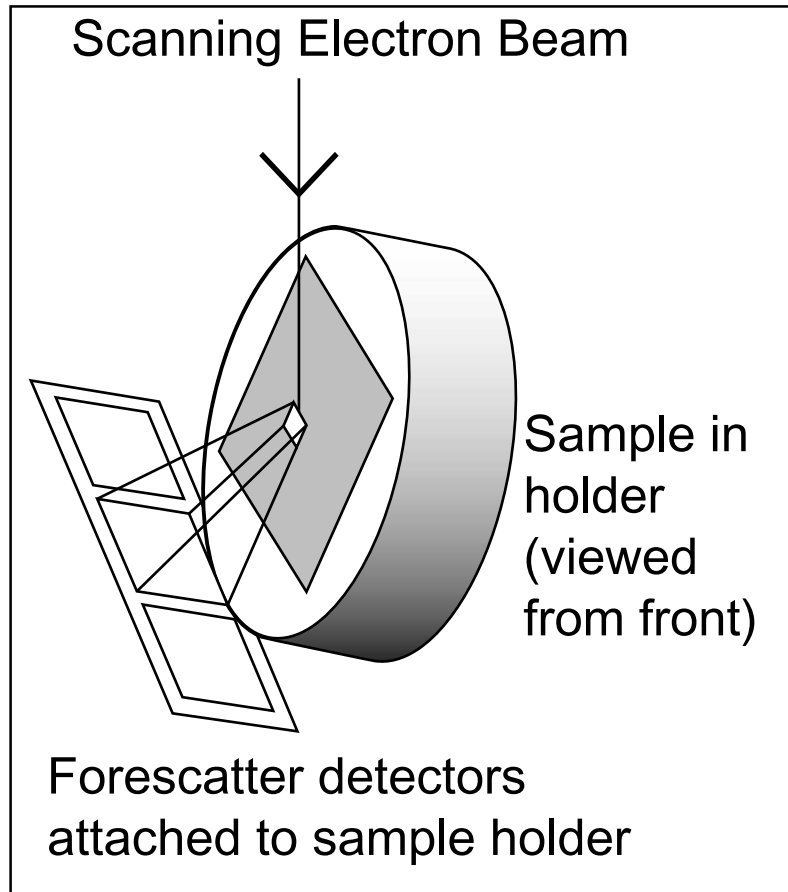
Figure 2.1. Unlike conventional BSE imaging, where the sample is normal to the electron beam, in OC imaging the sample is tilted ~70° from the horizontal. The solid-state detectors are mounted in front, and below the sample, and are generally referred to as forescatter detectors (modified from Prior et al., 1996).
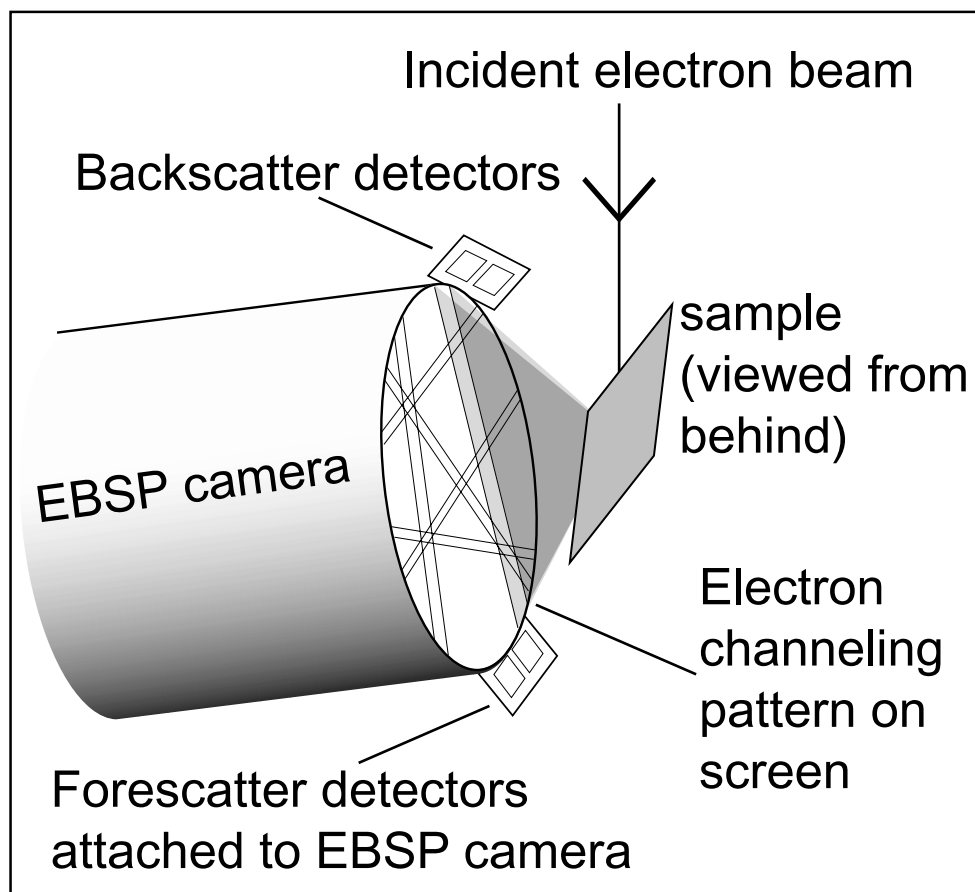
Figure 2.2. The pattern of lines on the phosphor screen is the electron diffraction pattern. Note also the forescatter detector and backscatter detectors mounted below and above the camera, respectively (modified from Prior et al., 1996).
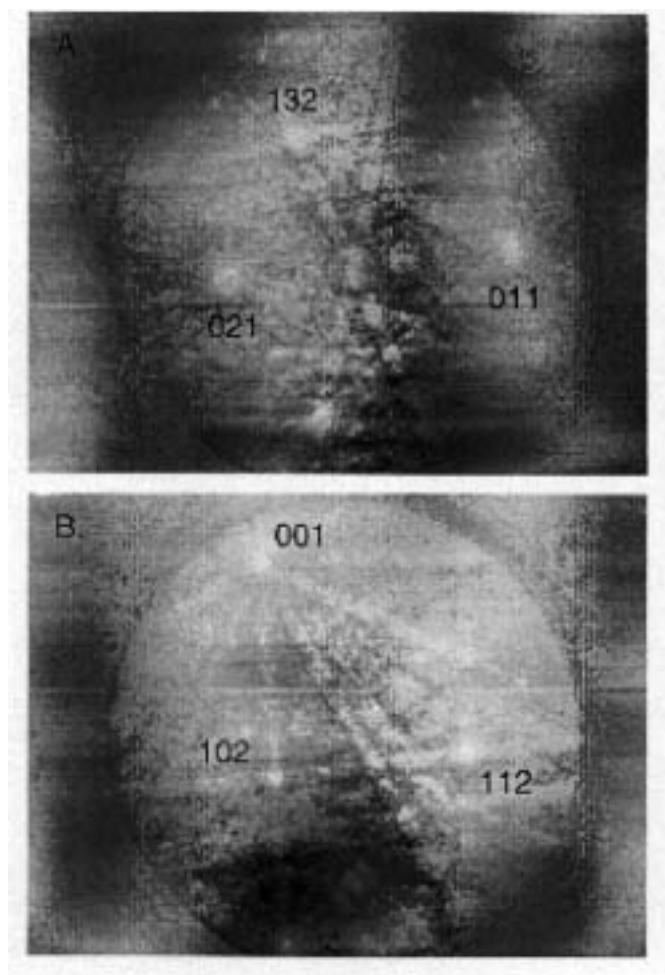
Figure 2.3.   Each set of parallel lines represent electrons diffracted from a set of crystallographic planes in a single orientation. Note the four-fold symmetry of the pattern near the top of Fig. 2.3b. This represents an [001] axis of the garnet.
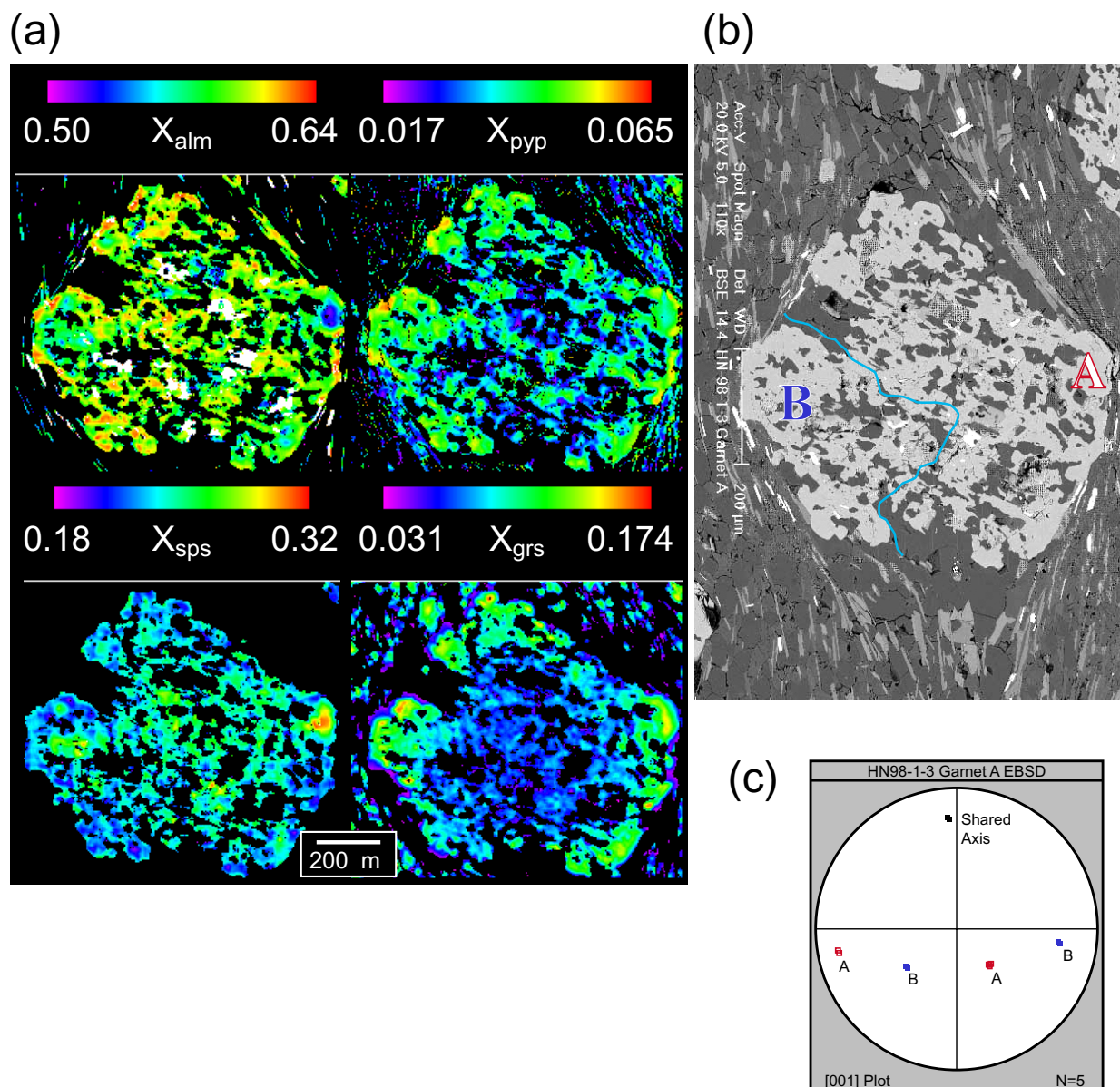
Figure 2.4. (a) Compositional zoning patterns for X_{Alm}, X_{Prp}, X_{Sps} and X_{Grs} in garnet porphyroblast A, sample HN-98-1-3. Note the isolated areas of high X_{Sps} and correspondingly low X_{Alm} and X_{Prp}. (b) Backscattered electron image on which is traced the location of a crystallographic misorientation boundary between domains A and B. (Boundary location is based on OCI and EBSP data.) Note lack of congruence between regions of low X_{Sps} and misorientation boundary. (c) EBSP pole plot summarizing five EBSP analyses on either side of the boundary. Points correspond to the three [001] directions on a stereographic projection; the data show that the angular difference between the domains is ~44°, and the two domains share an [001] axis; this leads to the interpretation of the crystallographic boundary as a sector twin.
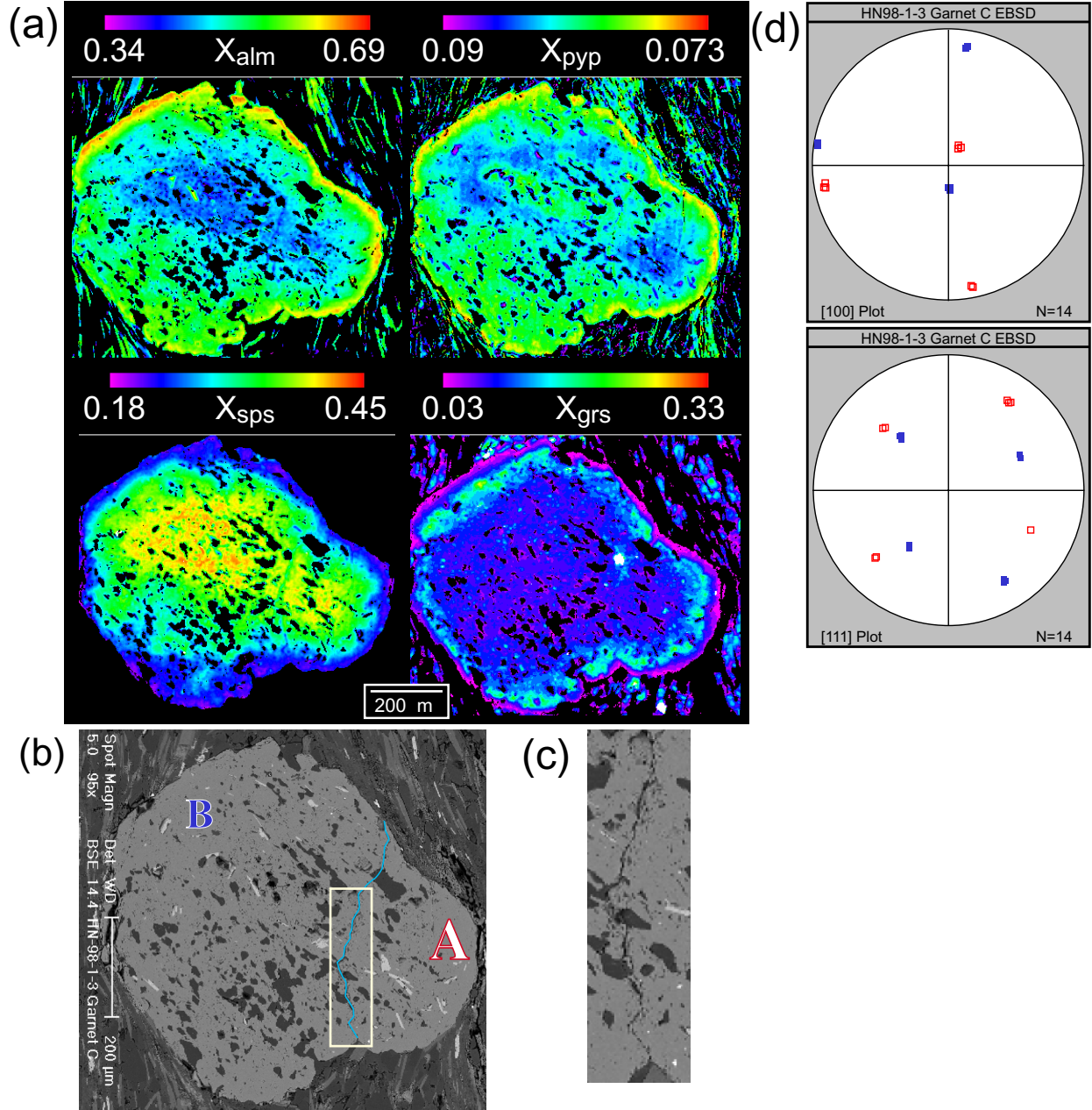
Figure 2.5. (a) Compositional zoning patterns for X_{Alm}, X_{Prp}, X_{Sps} and X_{Grs} in garnet porphyroblast C, sample HN-98-1-3. Note the isolated areas of high X_{Sps} and correspondingly low X_{Alm} and X_{Prp}. (b) Backscattered-electron image showing location of crystallographic misorientation boundary between domains A and B. (Boundary location is based on OCI and EBSP data.) Note congruence between one region of low X_{Sps} and misorientation boundary. Pale yellow box is region shown expanded in Fig. 2.5c. (c) Expanded BSE view of misorientation boundary. Grain boundary is visible in BSE view. (d) EBSP pole plots summarizing 14 EBSP analyses on either side of the boundary. Points correspond to the [001] directions (top) or [111] directions on a stereographic projection; hollow red boxes correspond to analyses of domain A, solid blue boxes correspond to analyses of domain B. The data show that the angular difference between the domains is ~33°. The obvious grain boundary together with the angular difference lead to the interpretation of separate nucleation and impingement.
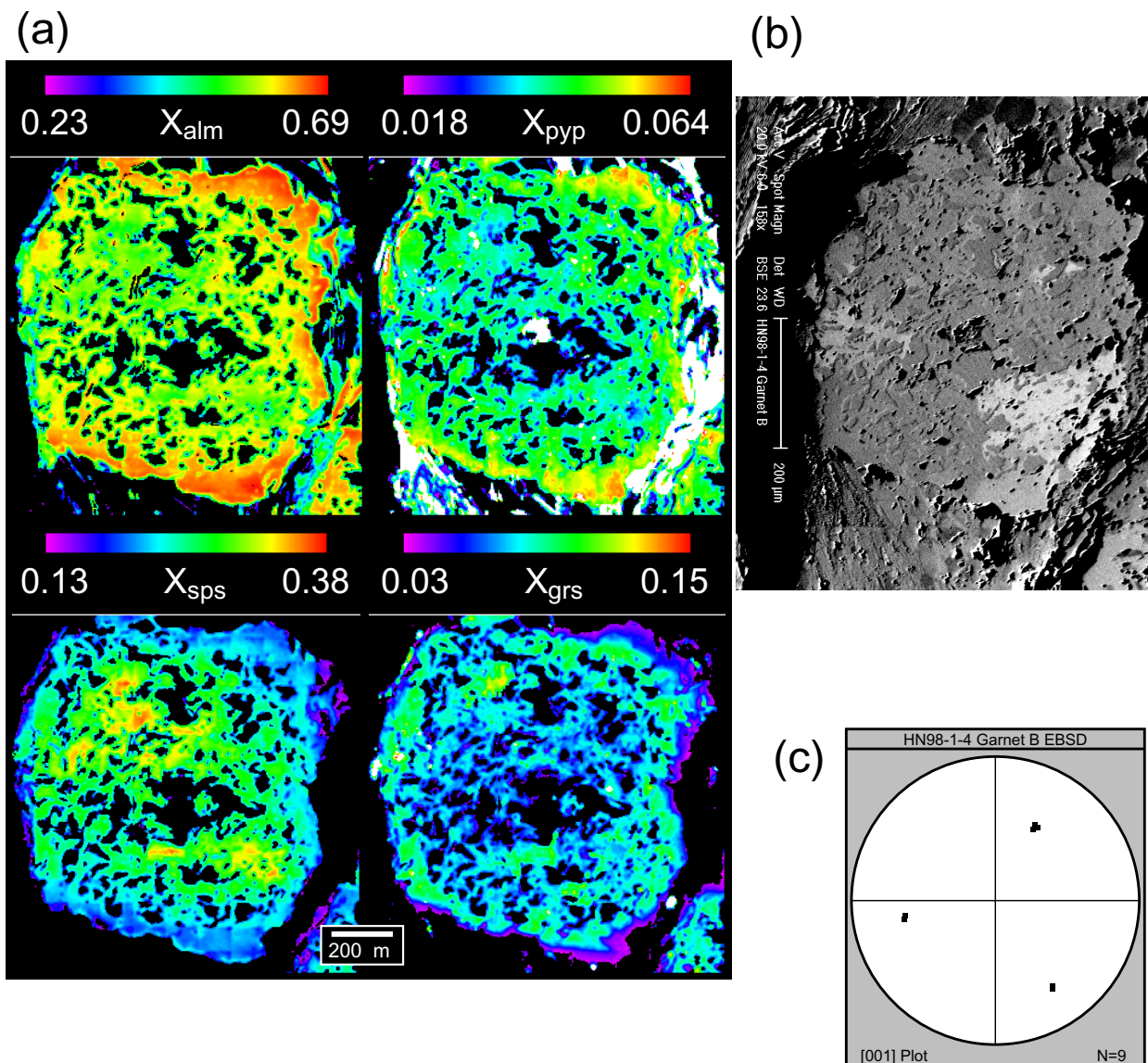
Figure 2.6. (a) Compositional zoning patterns for X_{Alm}, X_{Prp}, X_{Sps} and X_{Grs} in garnet porphyroblast B, sample HN-98-1-4. Note the isolated areas of high X_{Sps} and correspondingly low X_{Alm} and X_{Prp}. (b) Orientation contrast image showing location of misorientation. Image has been re-scaled to aspect ratio portrayed in the zoning maps, although distortion from original image remains. Note lack of congruence between regions of low X_{Sps} and misorientation boundary. (c) EBSP pole plot summarizing nine EBSP analyses on either side of the boundary. Points correspond to the three [001] directions on a stereographic projection. The data show that the angular difference between the domains is less than ~1°; this leads to the interpretation of the crystallographic boundary as a tilt wall.
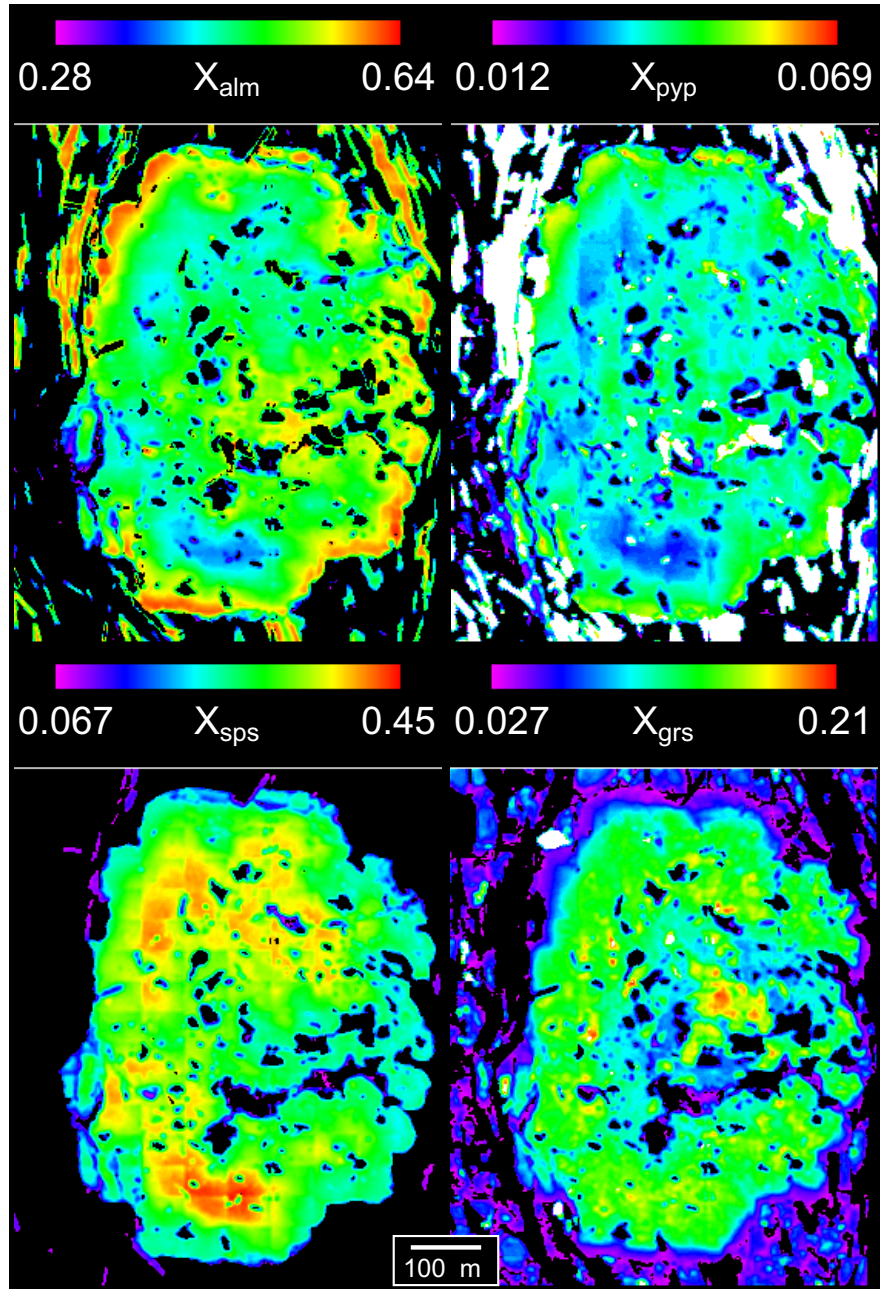
Figure 2.7a. Garnet porphyroblast B, sample HN-98-1-3. Note the isolated areas of high X_{Sps} and correspondingly low X_{Alm} and X_{Pyp}. Boundaries between these areas should, according to the multiple-nucleation hypothesis, correspond to boundaries between randomly oriented crystallographic domains; however, no such boundaries are observed in the OCI data.
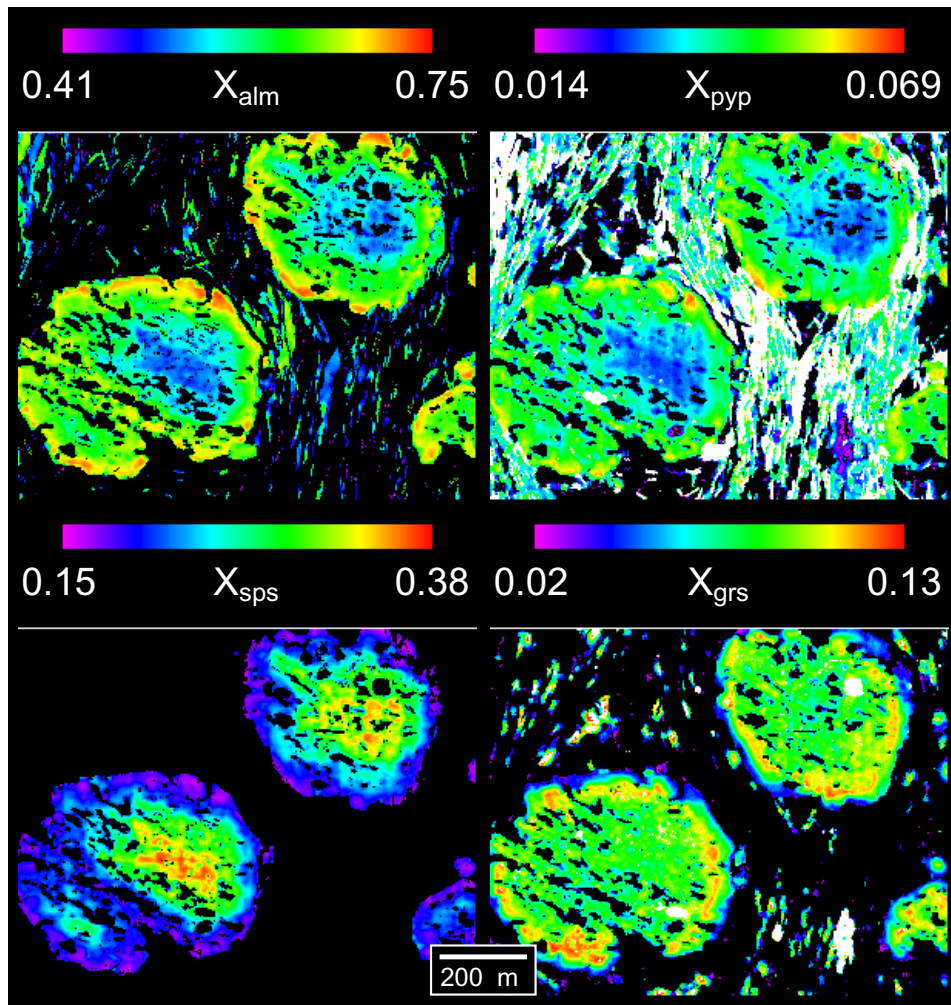
Figure 2.7b. Garnet porphyroblasts C and D (C is to the upper-right), sample HN-98-1-4. Note the isolated areas of high X_{Sps} and correspondingly low X_{Alm} and X_{Pyp}. Boundaries between these areas should, according to the multiple-nucleation hypothesis, correspond to boundaries between randomly oriented crystallographic domains; however, no such boundaries are observed in the OCI data.
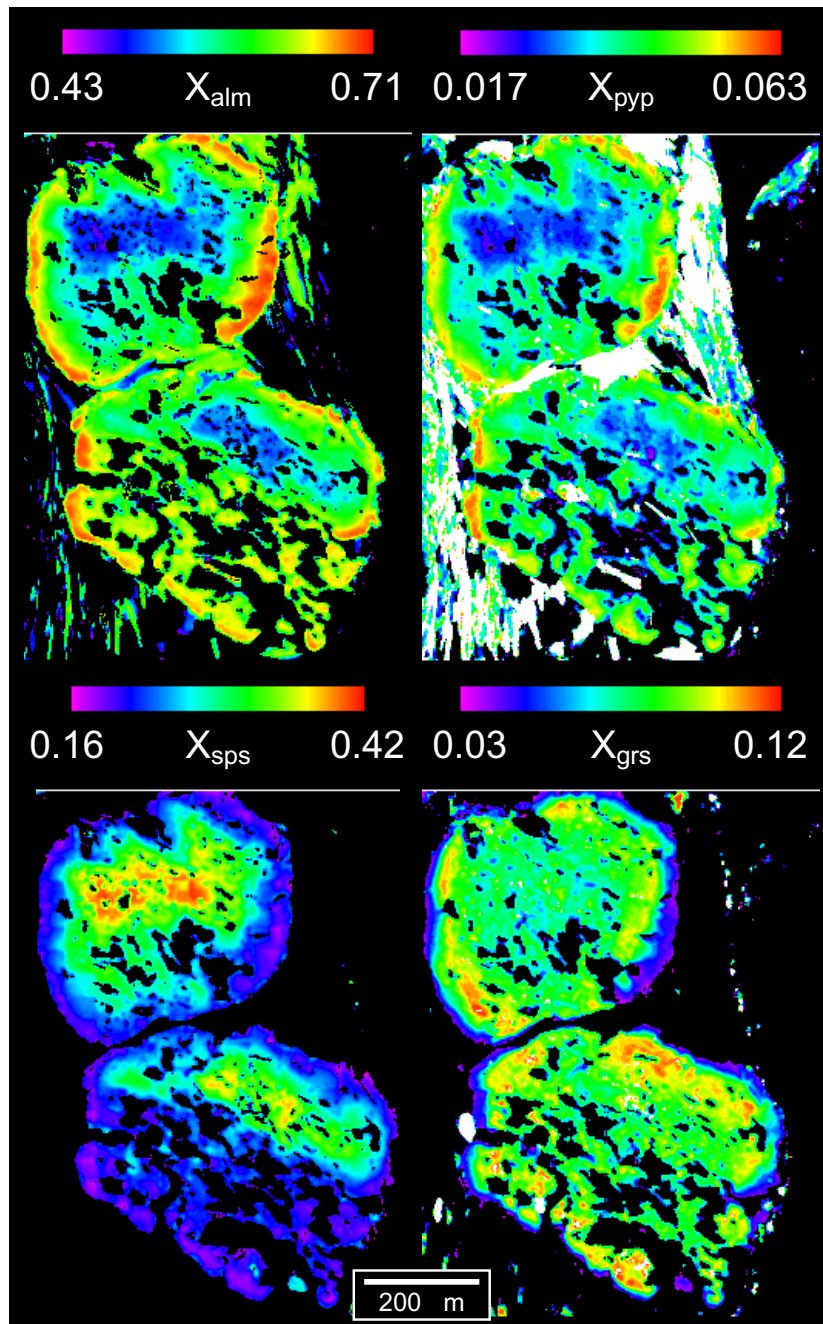
Figure 2.7c. Garnet porphyroblasts E and F (E is to the upper-left), sample HN-98-1-4. Note the isolated areas of high X_{Sps} and correspondingly low X_{Alm} and X_{Pyp}. Boundaries between these areas should, according to the multiple-nucleation hypothesis, correspond to boundaries between randomly oriented crystallographic domains; however, no such boundaries are observed in the OCI data.
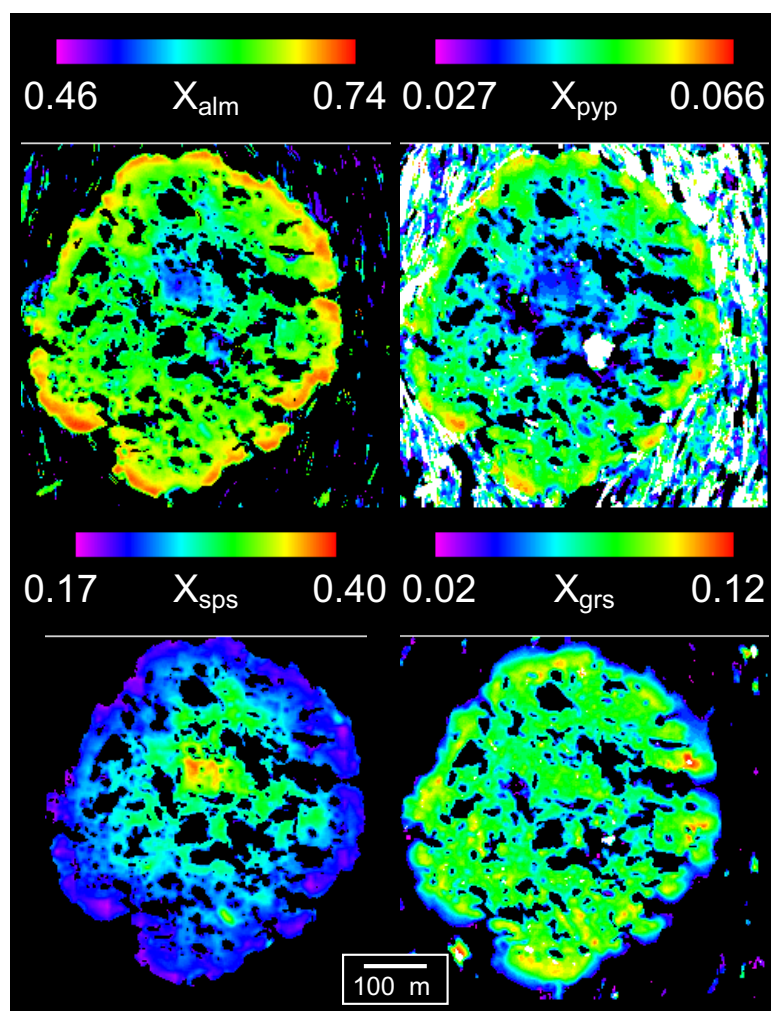
Figure 2.7d. Garnet porphyroblast G, sample HN-98-1-4. Note the isolated areas of high X_{Sps} and correspondingly low X_{Alm} and X_{Pyp}. Boundaries between these areas should, according to the multiple-nucleation hypothesis, correspond to boundaries between randomly oriented crystallographic domains; however, no such boundaries are observed in the OCI data.
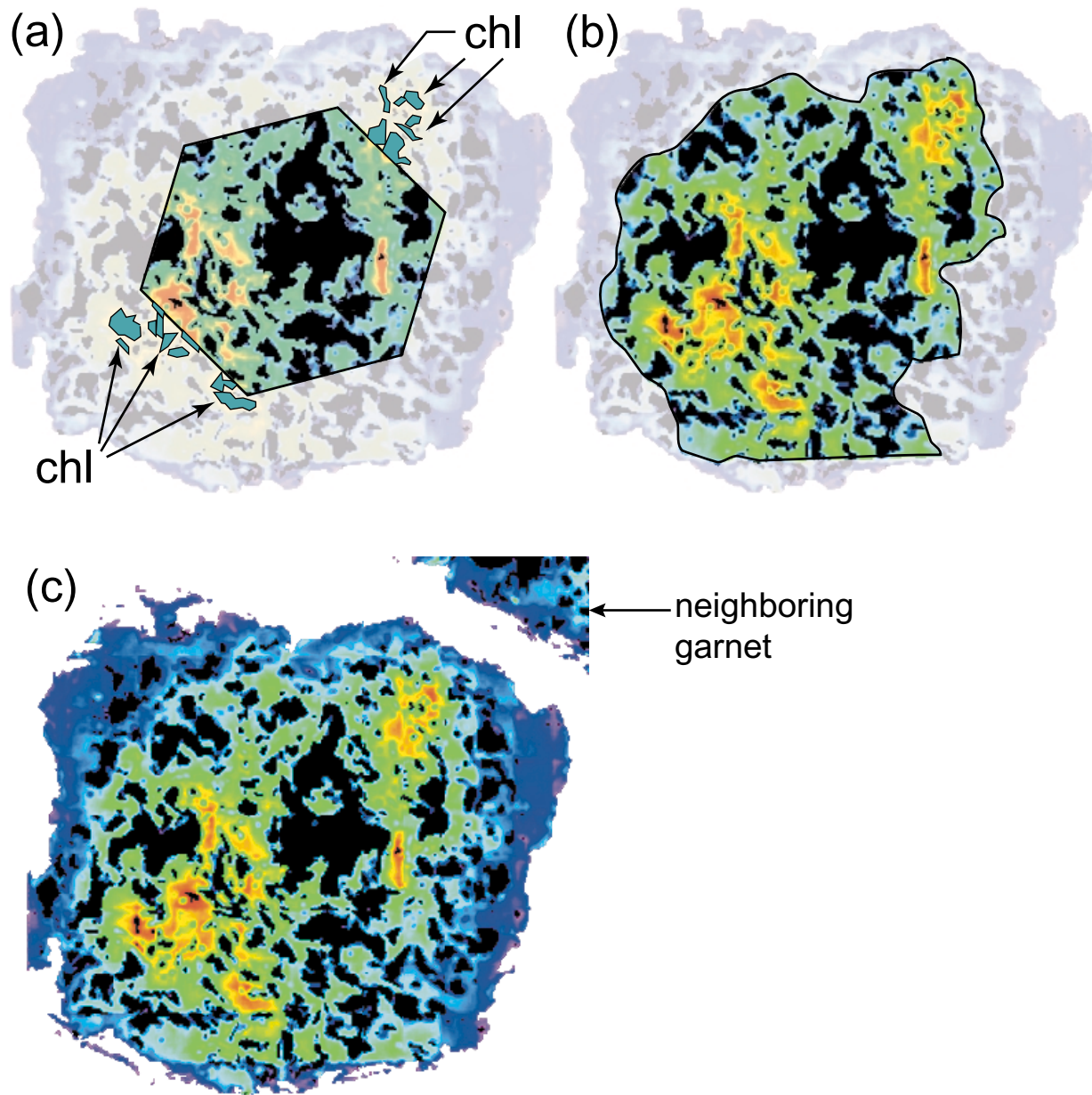
Figure 2.8. Schematic illustration of proposed growth model. Dim region depicts material not yet formed. (a) Early stage - scale of equilibrium is less than or equal to the matrix grain size; high-Mn regions record precursor distribution of Mn-rich phases, perhaps chlorite. (b) Intermediate stage - scale of equilibrium is that of a single garnet porphyroblast. Surface of garnet at this stage has approximately equal Mn content at all points. (c) Late stage - scale of equilibrium is at least that of the nearest-neighbor distance for garnets. Note that surface of partially visible nearby garnet has same Mn content as centered garnet.

Chapter 3. Nucleation vs. growth effects in metamorphism as revealed by a layered biotite-garnet porphyroblast schist

ABSTRACT

The crystallization of porphyroblasts is the result of a competition between nucleation of new crystals and growth of already-nucleated ones. The factors that govern this interplay are not yet fully understood. In order to examine this aspect of textural development of metamorphic rocks, I analyzed a sample of pelitic schist from the Picuris Mountains of New Mexico that contains both garnet and equant blocks of biotite. The results of this examination require distinctly different rates of biotite nucleation in two cm-scale adjacent layers.

The biotite porphyroblasts record a planar fabric in their inclusion patterns, one that is sub-parallel to the matrix schistosity; the garnets record a different fabric at a high angle to that in the biotites. I interpret the textures as suggesting garnet growth after biotite growth. In this sample, the size and abundance of biotite porphyroblasts vary from layer to layer on a ~3 cm scale; no difference is observed for garnet. This variation in biotite crystal size and abundance between small adjacent layers offers the opportunity to study mechanisms of nucleation and growth in specimens with identical thermal histories and strong compositional similarity.

The nature of the biotite layering was discovered to be threefold, on the basis of data on crystal sizes and locations obtained from high-resolution X-ray computed tomography. One layer has a larger mean crystal volume (10×10^{-4} vs. 2.4×10^{-4} cm^3), fewer biotite crystals per unit volume (229 vs. 574 crystals per cm^3), and a higher volume fraction of biotite (20% vs. 13%).

The similarity in assemblage and mineral chemistry between the two layers, coupled with their shared pressure-temperature-time history, suggests that the onset and cessation of biotite crystallization was nearly simultaneous for the two layers. They both show evidence for diffusional control of nucleation and growth, and the rate of diffusion must have been nearly the same in both layers. The bulk-compositional difference between the layers has an effect on the biotite sizes that is quantifiable and insufficient to account for the variation observed, requiring differences in nucleation rate during crystallization.

Textural modeling, intended to reproduce the crystallization process with the constraints provided by these samples, was unable to achieve the correct distribution of nucleation events over the crystallization

interval, requiring unreasonably high values for the activation energy for nucleation (Q_N>500 kJ/mol) in order to produce crystal size distributions that mirror those observed in the rock. This limitation of the model has been observed in previous work, and likely results from an inhomogeneous distribution of biotite-forming nutrients in the precursor, or the operation of a rate law for nucleation different from that included in the model.

Nevertheless, calculations could be performed that bracket the duration of crystallization, and thereby permit estimation of the average nucleation rates over the interval. Growth-duration estimates, based on both the scale of diffusion and time-explicit nucleation-and-growth simulations, agree on a approximate duration of 12 m.y., implying average nucleation rates of 19.1 and 47.8 nuclei cm^{-3} $m.y.^{-1}$ for the two layers.

INTRODUCTION

Porphyroblast crystallization in metamorphic rocks results from the interplay of several atomic-scale processes of nucleation and growth. One avenue to understanding the kinetics of this process is through quantitative analysis of metamorphic textures.

This study examines the competition between nucleation of new crystals and growth of already-nucleated ones through the analysis of a single sample of pelitic schist from the Picuris Mountains of New Mexico that contains both garnet and equant blocks of biotite (Figure 3.1). The biotite occurs in two distinct layers with different mean crystal size; this study examines the causes of the crystal size difference, and by extension, sheds light on the controls of crystal size in metamorphic rocks in general.

Crystal sizes and locations in three dimensions offer an insight into their nucleation and growth environment. This has been discussed in depth in previous work (e.g., Kretz, 1974; Walther and Wood, 1984; Carlson, 1989). Briefly, the relative rates of diffusion of chemical species to the site of the growing porphyroblast and attachment of those materials to the growing crystal will have implications for the spatial distribution and sizes of porphyroblasts in the rock. Slow diffusion relative to attachment will lead to a reduction in the chemical affinity for the reaction near the site of a growing porphyroblast, reducing the probability of nucleation there. This effect can be measured by quantifying the ordering of porphyroblast centers. Similarly, slow diffusion will lead to a reduction in the size of nearby crystals, because the domains from which they draw their "nutrients" will impinge upon each other. This effect can be measured by quantifying size-separation correlations in the crystal array. The above method of analysis has been documented in detail in earlier work (Carlson, 1989, 1991; Carlson and Denison, 1992; Carlson et al., 1995; Denison and Carlson, 1997; Denison et al., 1997; Daniel and Spear, 1999; Hirsch et al., 2000), but this study introduces two new factors: the analysis is performed for a new mineral (biotite) and with a second porphyroblast phase (garnet) that introduces complications, as discussed below.

PETROLOGY

Sample HCR2-3 is from the R2 member of the Precambrian Rinconada Formation exposed on the southern limb of the Copper Mountain Anticline in the Picuris Range of north-central New Mexico (UTM Zone 13 0426912E 4008746N). It is a biotite-garnet schist in which both garnet and biotite form equant crystals. The sample is layered at hand-sample scale; the bottom layer has significantly larger biotite

porphyroblasts than the top. In both layers the assemblage is bio+grt+mus+qtz+ilm, with sparse late chlorite, possibly after chloritoid. Modes are given in Table 3.1.

Garnet-biotite thermometry from the area has suggested that these rocks achieved peak temperatures of about 520 °C and about 4 kb in a Proterozoic regional metamorphic event (Grambling, 1988; Carlson, 1989). Because porphyroblast composition is linked to the minimum temperature at which the porphyroblast is stable, and therefore to the temperature of onset of nucleation, the composition of biotite in each layer was measured. Analyses were performed using the JEOL 733 Superprobe electron microprobe using 15 kV accelerating voltage and a beam current on brass of 30 nA. Counting for each peak terminated at 40s or after accumulation of 100,000 counts. Representative analyses are listed in Table 3.2, and show no significant difference in biotite or garnet composition between the two layers.

Petrofabric Analysis

Other work in the area has documented a complex metamorphic and deformational history (McIntyre, 1981; Chernoff, 1992; Bauer, 1993). McIntyre (1981), in particular, has concluded that garnet and biotite growth in this area were "probably synchronous". However, in this sample, the garnet porphyroblasts record one planar fabric in their inclusion patterns, while the biotite blocks record another (Figure 3.2), suggesting that it may be possible to determine the sequence of crystallization.

The fabric in the biotites is at a low angle to S_0, which is a compositional layering seen in outcrop that is parallel to the size-layering present in this sample. I interpret this included fabric as S_1. Other workers (e.g., Bauer, 1987, pp. 86, 49, 165) have made a similar interpretation for fabrics included in porphyroblasts in these rocks, although biotite is not specifically mentioned. Following growth of the biotites, the fabric was transposed into S_2, and this fabric was crenulated by S_3. Garnet growth began following the development of S_2, and ceased before S_3, or just following its onset, as shown by the incipient crenulation of the fabric in the garnet of Figure 3.2b. As the extension direction implied by the abundant quartz-rich pressure shadows around biotite is consistent with the contraction direction indicated by S_2, I interpret these pressure shadows as forming during S_2. Notably, no pressure shadows are found around garnet, lending credence to this interpretation. At a minimum, the presence of pressure shadows only around biotite requires that biotite crystallization began before the onset of garnet crystallization.

Interpretation of fabrics for garnet-biotite growth relations

Modeling of the biotite crystallization requires an understanding of the relative timing of garnet and biotite nucleation and growth. Unfortunately, the lack of lower-grade precursors precludes knowledge of the precise biotite-forming reaction, which might aid this understanding. The mineral textures are, in a strict sense, inconclusive as to whether biotite or garnet grew earlier. Nevertheless, they argue strongly against synchronous growth, as shown in Figure 3.2, because that would require an implausible scenario in which biotite and garnet grew synchronously, yet included two different planar fabrics at high angles to one another. As discussed above, the textural relations in Figure 3.2 are instead interpreted as indicating garnet growth following biotite growth.

It is important for the purposes of textural analysis to know whether biotite was a reactant during the formation of garnet. An analysis of the garnet textures indicates diffusion-controlled nucleation and growth (Appendix 3A). In light of this, if biotite were a reactant, one would expect a sparser and/or smaller set of biotites in the vicinity of garnet porphyroblasts, which is not observed (Fig. 3.2a). The textures are interpreted as supporting garnet growth following biotite, from a reaction such as chl + qtz = grt + H_2O. Note that although biotite is not a primary reactant, there must be some explanation for the lack of biotite inclusions within garnet. I interpret the textures as suggesting a biotite-consuming reaction localized near the growing garnet, such as bio + qtz = grt + msc + H_2O. This very localized reaction might be balanced by a biotite-producing reaction in the matrix more distant from garnets (cf., Foster, 1986, 1999).

The above interpretation of the garnet-biotite growth relations is not unequivocal. However, two facts mitigate this uncertainty. First, the volume fraction of garnet in the rock is small relative to that of biotite, and so if the above interpretation were incorrect, and biotite were involved in the garnet-forming reaction, the observed biotite radii would be altered only slightly (~10% for bottom layer, ~15% for top layer). Second, for other possible garnet-biotite growth relations (such as garnet preceding biotite, or garnet and biotite growing simultaneously), the method of quantitative textural analysis detailed below would be unchanged.

DATA COLLECTION

The data required for the quantitative analysis of textures are three-dimensional: knowledge of the sizes and locations of all porphyroblasts in the sample volume. For this study, such data were obtained using the high-resolution X-ray computed tomographic scanner at The University of Texas at Austin, Department

of Geological Sciences. The data are extracted from a set of grayscale images, in which brightness roughly correlates to density. A typical scan image from the study is shown in Figure 3.3.

The biotite crystals in each slice are located, as are the garnets (separately). This is performed in the BLOB program (Appendix), in which contiguous regions of a user-determined range of grayscales are identified, and their area and centroid are recorded (Figure 3.4). These sections through each crystal are integrated into 3-D objects using the program INTEGRATE (Appendix), in which the stacks of 2-D sections are combined using heuristics and user decisions into separate 3-D regions, whose volume and 3-D centroid are recorded. The rock up to this point was treated as one data set, and the data set was split to segregate the two layers after integration into a 3-D array by inspection of crystal size statistics (Figure 3.5). Finally, the array of 3-D objects is analyzed for ordering and clustering trends using the program REDUCE3D (Appendix).

RESULTS

Primary Textural Measures

Primary measures of textural features of the biotite porphyroblasts (Table 3.3) offer important clues to the causes of the difference in biotite size between the layers. The garnet data reveal no variation with position in the sample, and are treated as a single data set for the complete specimen (Table 3.3). These data are notable in two ways, which are discussed below: they demonstrate a significant difference in volume fraction and in crystal number density between the two layers.

Statistical Analysis

The presence of an additional porphyroblast phase adds significant complication to statistical analyses of the type described in Hirsch et al. (2000). The interpretation given above, that of biotite growth preceding garnet growth, with biotite sizes and locations largely unaffected by later crystallization of garnet, determines the analytical approach taken to study this dual-porphyroblast rock. In this growth model, garnet crystals are essentially regions that masked the biotite textures that they overgrew, but did not have an appreciable effect on biotite textures outside their volume. Because of this, volumes occupied by garnet can be treated as "no-data regions." In practice, this approach is implemented by treating the surfaces of the garnet crystals in the same way that one treats the exterior boundaries of the sample itself – the garnets then create "holes" in the data volume. It is of note that most other plausible interpretations of the relationship between biotite and garnet growth (e.g., biotite reacting to form garnet, or biotite growth following garnet growth) would be treated identically to the favored model, with the garnets treated as "no-data regions." One interpretation not

tractable with this method is biotite displacement through dissolution (near garnet) and precipitation (distant from garnet). Under this model, however, one would expect decreased biotite crystal size near garnet and biotite overgrowth textures (of different composition or inclusion density), neither of which are observed.

The first step in understanding the biotite crystallization in HCR2-3 is to ascertain the rate-controlling step in its nucleation and growth process: was it diffusion-controlled (slow diffusion relative to interface processes) or interface-controlled (rapid diffusion relative to interface processes)? Two types of statistics can shed light on this issue: single-scale measures (ordering, clustering, and impingement indices) and multi-scale measures (L' function, Pair Correlation Function and Mark Correlation Function). These statistical tests were introduced by Raeburn (1996) and Daniel and Spear (1999). The implementation used here is discussed in detail in Hirsch et al. (2000).

Values of the single-scale statistics are shown graphically in Figure 3.6, and all indicate significant ordering relative to a null hypothesis of interface-controlled nucleation and growth. This result is the same for both layers.

Figure 3.6 also shows values for the Correlation Function statistics at a range of scales given on the horizontal axis. These graphs diagram the relationship between the sample data and a set of 100 Monte Carlo interface-controlled null-hypothesis simulations, the 96th-percentile bounds for which are shown in pink. Sample values that fall below the null-hypothesis region indicate excess ordering relative to the interface-controlled case, and values that fall above the region indicate excess clustering. Values that fall within the null-hypothesis region provide no information. These data show that the two layers share many of the same features: ordering of crystal centers up to about the mean nearest-neighbor distance, and suppression of growth of nearby porphyroblasts to somewhat greater distances. It is of interest that only the top layer (with smaller crystals) shows strong clustering at larger scales of measurement.

All the single-scale and multi-scale statistics agree: they indicate a diffusion-limited nucleation and growth history for both layers.

DISCUSSION

The differences in the textural measures between these two layers provide constraints on nucleation rates in HCR2-3, and analysis of these textures demonstrates variation in nucleation rate across a single hand sample. The two layers experienced the same temperature-time history, and although small differences in bulk chemistry (Table 3.4) obscure the effect somewhat, this shared temperature-time history allows the

identification of variation in nucleation rate between the layers and semi-quantitative modeling of the layers' nucleation and growth.

The layers have a similar history in many ways. Because they are separated only by millimeters, they must have had identical pressure-temperature-time histories. The similarity in mineral chemistry between the layers, coupled with the similarity in pressure and temperature, suggests that the onset and cessation of biotite crystallization was the nearly simultaneous in the two layers. Because they both show evidence for diffusional control, they must have been governed by the same rate laws for nucleation and growth. Moreover, the parameters for the diffusion rate law are likely to have been closely similar as well. This final point may not be intuitive, and merits further discussion.

The slowest-diffusing component for garnet growth is thought to be aluminum (Whitney and McLelland, 1973; Thompson, 1975; Johnson and Carlson, 1990; Carlson and Johnson, 1991; Ashworth et al., 1992). The diffusion rate of aluminum can be linked to two other factors: temperature and the nature of the intergranular medium. As mentioned above, temperature must have been the same in both layers, so the only other factor likely to lead to a difference in diffusion rates is the nature of the intergranular medium. The medium could potentially vary in its chemical composition, volume, or shape of its network. Although information about the intergranular medium is impossible to obtain directly, petrologic and petrographic evidence suggests that the medium did not vary appreciably between the two layers.

It is inferred that the chemical composition of the medium was similar in both layers, because the present mineral assemblage and chemical composition of the phases in each layer are indistinguishable (e.g., Table 3.2). Any fluid present must have had similar influence on the chemical composition of the minerals in each layer. It should be noted however, that if the fluid did not interact significantly with the assemblage, then it may have differed in volume and perhaps in composition between the layers. The observed variation in crystal size with position (Fig. 3.5) may resemble those displayed by layer-perpendicular fluid-flow. The small scale of the layering (~3 cm) makes this an unlikely explanation for the observed variation in crystal size. The shape and volume of the intergranular medium network are dictated largely by the matrix grain size, and the distribution of various minerals within the matrix. Both in the present matrix, and in the remnants of matrix preserved as inclusions within the biotite porphyroblasts, the mineralogy and grain size show no variation between the layers.

On the basis of these lines of evidence, it is concluded that the rates of diffusion, and therefore the diffusion rate law parameters, were similar, if not identical, between the two layers. The only factors that are

likely to have differed between the layers are the amount of biotite nutrients per unit volume, and perhaps the nucleation-rate parameters.

The difference in biotite nutrients and difference in nucleation density each has an effect on biotite porphyroblast size that is quantifiable, and that cannot account for the full range of size variation observed. Assuming a closed system (and there is no evidence to the contrary), the difference in volume fraction of biotite between the layers (after accounting for garnet growth) requires that there was more overall biotite crystallization in the layer with the greater volume fraction, which happens to be the layer with the larger biotite crystals. But this variation in volume fraction can account only for part of the size difference observed between the layers. For example, if the top layer had the same number density of biotites as the bottom, then apportioning the observed volume fraction for the top layer (less than in the bottom layer) among the identical number of crystals would yield a smaller mean biotite volume than in the bottom layer. However, this reduced size, 6.0×10^{-4} cm^3, is still larger than the observed size of 2.4×10^{-4} cm^3, although both are smaller than the bottom layer's 10×10^{-4} cm^3. This "excess size variation" must be due to differences in the nucleation rates between the two layers. Conversely, the difference in nucleation density (observed in the rock as crystal number density), is also insufficient to account for the observed variation in crystal size. If the top layer had the same volume fraction of biotite as the bottom layer, then apportioning the identical volume of biotite among more numerous crystal in the top layer would yield smaller mean crystal size than in the bottom layer. However, this reduced size, 3.7×10^{-4} cm^3, is still larger than the observed size of 2.4×10^{-4} cm^3. Variation in both the amount of biotite nutrients (volume fraction), and nucleation density (crystal number density) are required to account for the observed variation in crystal size.

Textural modeling

Because the computational model of Carlson et al. (1995) incorporates all of the factors discussed above, it was hoped that its use would allow the distribution of nucleation events over time in both layers to be quantified. However, as has been observed previously, the model is unable to produce matches to some crystal size distributions using reasonable parameters for the nucleation rate law. Nevertheless, the model does yield valuable information that for the first time constrains average nucleation rates for biotite.

Using the statistical evidence for diffusional suppression of biotite growth (Fig. 3.6), one can model the diffusion-controlled nucleation and growth of each layer. The numerical model incorporates explicit time and temperature variables, and its inputs include the activation energies and pre-exponential constants for

nucleation and diffusion, the temperature of onset of porphyroblast growth, and the prograde heating rate (Carlson et al., 1995).

The goal of this modeling was to further test the above conclusions as to the causes of the size layering, by modeling the two layers with identical intensive variables and diffusion-rate constants, varying only the volume fraction of biotite-forming material and the nucleation-rate constants. Unfortunately this goal proved elusive. In order to correctly model the biotite crystal size distributions shown in Figure 3.7, unreasonable values for Q_N, the activation energy for nucleation, were required as model inputs. Values in excess of 500 kJ/mol were required in order to generate the very strong positive skewness of the size distributions; these values exceed those for breaking Si-O bonds, and are therefore unreasonable for modeling nucleation. This problem has been encountered before (Carlson et al., 1995, p. 221), and represents the failure of the model to correctly capture the distribution of nucleation events through time. By requiring an excessively large Q_N, the model moves a disproportionate number of nucleation events to later stages of the crystallization interval, and therefore to higher temperatures. To illustrate, the nucleation rate in the undepleted portions of the volume would vary over the course of a possible range of temperature (350 - 450 °C) by a factor of about 210, given a value for Q_N of 200 kJ/mol (a reasonable value), but given the extreme values such as those observed of 500 kJ/mol, the nucleation rate in the undepleted portions of the volume would vary by a factor of about 1×10^7!

There are a number of potential explanations for this inability to model the true distribution of nucleation times. The two most-favored alternatives are an inhomogeneous distribution of the slowest-diffusing element, probably aluminum, or a rate law for nucleation other than that given in Carlson et al. (1995), specifically, the existence of various sets of nucleation sites, each with their own activation energy for nucleation. The former explanation could increase the skewness by allowing crystals nucleating in "nutrient-rich" regions to grow larger than would be predicted by the model. The latter explanation could act by allowing a small number of early-nucleated biotites to grow larger than would be expected from the model.

Work is underway to develop a more complex model of porphyroblast nucleation and growth. This more refined model will, it is hoped, be able to adequately model the development of the biotite textures observed in these layers. Nonetheless, it is possible to extract useful data from the model for these layers of HCR2-3.

Estimates for the time scale of nucleation for each layer were obtained through the use of diffusional parameters and mean nearest-neighbor separation. The characteristic length scale of diffusional processes can be estimated from the relation

$$x \approx \sqrt{Dt}. \tag{3.1}$$

This provides a means of estimating the mean duration of biotite growth from mean crystal separations, and therefore provides an approximate lower bound on the duration of the nucleation interval. In this equation, the diffusion rate in the temperature range of biotite formation is given by

$$D = D_\circ\, e^{-Q_D/RT} \tag{3.2}$$

where D is the diffusion rate, $D_\circ$ is a constant, Q_D is the activation energy for diffusion (taken as 140 kJ/mol), and R is the ideal gas constant. A value for $D_\circ$ of $5 \times 10^{-7}\,\mathrm{cm^2 s^{-1}}$ was obtained using as its basis results from previous modeling of rocks in the area (Carlson et al., 1995). That work identified values for Q_D and $D_\circ$ of 84 kJ/mol and $7 \times 10^{-11}\,\mathrm{cm^2 s^{-1}}$, respectively. At a temperature in the region of interest, 480°C, these values produce a diffusion rate (using equation 3.2) of $1 \times 10^{-16}\,\mathrm{cm^2 s^{-1}}$. The chosen value for $D_\circ$ is that which produces an identical diffusion rate given a value for Q_D of 140 kJ/mol. This is combined with an estimate of the scale of diffusion, x, calculated as half the mean nearest-neighbor distance (Table 3.3). This calculation for the duration of nucleation provides one estimate for each layer; the top layer provides an estimate of approximately 11 m.y., and the bottom layer provides an estimate of approximately 6 m.y.. These values are reasonable in light of published estimates for the duration of metamorphism: England and Thompson (1984, p. 918) used thermal modeling to obtain estimates for the overall duration of metamorphism of 100-200 m.y., of which garnet growth will be only a fraction. Smith et al. (1994, p. 506) used radioisotopes to obtain estimates for the duration of metamorphism in the Himalayas of 5-10 m.y., and Vance (1995, p. 249) used Sm-Nd radioisotopes to obtain a duration for garnet growth of 10.5 ± 4.2 m.y..

Using these estimates for diffusion-rate parameters and the duration of the nucleation-and-growth event, simulations were performed with the computational model of Carlson et al. (1995) with the goal of reproducing the crystal size distributions observed in the two layers of HCR2-3. The model parameters for heating rate, and the nucleation rate law parameters were constrained by a fit to the measured crystal size distributions. Good matches to the measured crystal size distributions were obtained (Fig. 3.8), with crystallization periods in the range predicted by the $x \approx \sqrt{Dt}$ calculations above, 6 - 11 m.y.. Complete model parameters are listed in Table 3.5.

The extremely high values for Q_N can be used to bracket the duration of nucleation; because they require much of the crystallization to occur very late in the event, there is a relatively long period of little growth. This should provide an upper bound on the duration of the crystallization event. To try to obtain a lower bound, additional simulations were performed with the same heating rate and diffusional parameters as those given in Table 3.5, but rather than allowing nucleation to occur throughout the episode, the required number of nuclei were induced at the outset. This serves to remove nucleation as a delaying factor, and only the sluggishness of diffusion limits the crystallization for these models. These results are also listed in Table 3.5, and the crystallization durations are shorter than the previous simulations by only about 3 m.y.. The results one would expect for more reasonable values of Q_N should fall between these two extremes (Fig. 3.9). This approach to bracketing the distribution of nucleation events over time allows us to circumvent partially the known limitations in the model's treatment of nucleation rate, and to instead estimate an average nucleation rate for each layer (Table 3.5).

CONCLUSIONS

This work is the first to quantitatively examine the textural features of a porphyroblastic sample with multiple porphyroblast phases. The unusually equant character of the biotite porphyroblasts has allowed the first analysis of a non-garnet porphyroblast phase, leading to the conclusion that the crystallization of biotite in this instance is diffusionally controlled, as has been seen to be commonplace for garnet. It is of note that both phases are aluminous; this fact supports the notion that the diffusion of aluminum is the slowest of the elements involved, and that this is the rate-limiting step in the crystallization of these phases. Similar analysis of non-aluminous porphyroblasts can be expected to show quantitatively and qualitatively different textures, given that a different process may be the rate-limiting step in their crystallization.

Through the use of basic textural measures and time-explicit, thermally accelerated simulations of nucleation and growth, estimates for the duration of the nucleation interval were obtained. Two different methods of calculating this interval agree on a duration of 11-14 m.y. for the bottom layer and 10-13 for the top layer.

This study has for the first time demonstrated a difference in nucleation rate across a hand sample, and, despite model limitations, provided some numerical estimates for nucleation rate of biotite porphyroblasts during metamorphism. Average nucleation rate estimates of 19.1 and 47.8 nuclei per cm^3 per m.y. for the bottom and top layers, respectively, are the first such values of their kind obtained.

REFERENCES CITED

Ashworth, J. R., Birdi, J. J. and Emmett, T. F., 1992. Diffusion in coronas around clinopyroxene; modelling with local equilibrium and steady state, and a non-steady-state modification to account for zoned actinolite-hornblende. *Contributions to Mineralogy and Petrology*, **109**, 307-325.

Bauer, P. W., 1993. Proterozoic tectonic evolution of the Picuris Mountains, northern New Mexico. *Journal of Geology*, **101**, 483-500.

Bauer, P. W., 1987. Precambrian geology of the Picuris Range, North-Central New Mexico. *Unpub. Doctoral Thesis, Institute of Mining and Technology, Socorro, New Mexico.*

Carlson, W. D., 1991. Competitive diffusion-controlled growth of porphyroblasts. *Mineralogical Magazine*, **55**, 317-330.

Carlson, W. D., 1989. The significance of intergranular diffusion to the mechanisms and kinetics of porphyroblast crystallization. *Contributions to Mineralogy and Petrology*, **103**, 1-24.

Carlson, W. D. and Denison, C., 1992. Mechanisms of porphyroblast crystallization: Results from high-resolution computed X-ray tomography. *Science*, **257**, 1236-1239.

Carlson, W. D., Denison, C. and Ketcham, R. A., 1995. Controls on the nucleation and growth of porphyroblasts; kinetics from natural textures and numerical models. *Geological Journal*, **30**, 207-225.

Carlson, W. D. and Johnson, C. D., 1991. Coronal reaction textures in garnet amphibolites of the Llano Uplift. *American Mineralogist*, **76**, 756-772.

Chernoff, C. B., 1992. Microstructural analysis of poly-deformed Mid-Proterozoic metasediments of the western Picuris Range, New Mexico: A deformational history of the Piedra Lumbre region. *Unpub. B.S. Thesis, University of Texas at Austin, Austin, TX.*

Daniel, C. G. and Spear, F. S., 1999. The clustered nucleation and growth processes of garnet in regional metamorphic rocks from north-west Connecticut, USA. *Journal of Metamorphic Geology*, **17**, 503-520.

Denison, C. and Carlson, W. D., 1997. Three-dimensional quantitative textural analysis of metamorphic rocks using high-resolution computed X-ray tomography. Part II: Application to natural samples. *Journal of Metamorphic Geology*, **15**, 45-57.

Denison, C., Carlson, W. D. and Ketcham, R. A., 1997. Three-dimensional quantitative textural analysis of metamorphic rocks using high-resolution computed X-ray tomography. Part I: Methods and techniques. *Journal of Metamorphic Geology*, **15**, 29-44.

England, P. C. and Thompson, A. B., 1984. Pressure-temperature-time paths of regional metamorphism; I, Heat transfer during the evolution of regions of thickened continental crust. *Journal of Petrology*, **25**, 894-928.

Foster, C. T., Jr., 1999. Forward modeling of metamorphic textures. *The Canadian Mineralogist*, **37**, 415-429.

Foster, C. T., Jr., 1986. Thermodynamic models of reactions involving garnet in a sillimanite/staurolite schist. *Mineralogical Magazine*, **50**, 427-439.

Grambling, J. A., 1988. A summary of Proterozoic metamorphism in northern and central New Mexico; the regional development of 520 degrees C, 4-Kb rocks. In: *Metamorphism and crustal evolution of the Western United States* (ed Ernst, W. G.), pp. 446-465, Los Angeles, CA, United States.

Hirsch, D. M., Ketcham, R. A. and Carlson, W. D., 2000. An evaluation of spatial correlation functions in textural analysis of metamorphic rocks. *Geological Materials Research*, **2**, 1-41.

Johnson, C. D. and Carlson, W. D., 1990. The origin of olivine-plagioclase coronas in metagabbros from the Adirondack Mountains, New York. *Journal of Metamorphic Geology*, **8**, 697-717.

Kretz, R., 1974. Some models for the rate of crystallization of garnet in metamorphic rocks. *Lithos*, **7**, 123-131.

McIntyre, J. F., III, 1981. Structural and metamorphic interrelationships across the Copper Hill Anticline, Picuris Mountains, New Mexico. *Unpub. Master's Thesis, University of Texas, Austin, Austin, TX, United States.*

Raeburn, S. P., 1996. New methods in quantitative metamorphic petrology. *Unpub. Ph.D. Thesis, Pennsylvania State University.*

Smith, H. A., Chamberlain, C. P. and Zeitler, P. K., 1994. Timing and duration of Himalayan metamorphism within the Indian Plate, Northwest Himalaya, Pakistan. *Journal of Geology*, **102**, 493-508.

Thompson, A. B., 1975. Calc-silicate diffusion zones between marble and pelitic schist. *Journal of Petrology*, **16**, 314-346.

Vance, D. and Boyle, A. P., 1995. Rate and time controls on metamorphic processes. *Geological Journal*, **30**, 241-259.

Walther, J. V. and Wood, B. J., 1984. Rate and mechanism in prograde metamorphism. *Contributions to Mineralogy and Petrology*, **88**, 246-259.

Whitney, P. R. and McLelland, J. M., 1973. Origin of Coronas in Metagabbros of the Adirondack Mts., New York. *Contributions to Mineralogy and Petrology*, **39**, 81-98.

TABLE 3.1. MINERAL MODES.

Layer	Garnet	Biotite	Quartz	Muscovite	Ilmenite	Chlorite
Bottom (large)	7	21	48	21	3	<1
Top (small)	7	13	47	31	2	<1

Biotite and garnet modes obtained from CT data, other phases estimated petrographically.

TABLE 3.2. REPRESENTATIVE BIOTITE AND GARNET ANALYSES.

Layer	crystal	point	SiO_2	TiO_2	Al_2O_3	FeO[1]	MnO	MgO	CaO	K_2O	Total
Biotite -	2	1	33.2	1.73	19.3	27.6	0.01	4.07	n.a.[2]	8.98	94.9
Bottom	2	2	32.2	1.65	18.7	27.3	n.d.[3]	3.90	n.a.	8.81	92.5
(large)	5	1	32.5	1.70	19.2	27.5	n.d.	4.04	n.a.	8.85	93.7
	5	2	33.3	1.60	19.4	27.5	0.01	4.12	n.a.	8.71	94.5
	5	3	32.2	1.68	19.0	27.3	n.d.	4.06	n.a.	8.74	93.0
Biotite -	3	1	32.9	1.10	19.2	28.7	0.01	4.12	n.a.	9.06	95.0
Top	4	1	33.3	1.65	19.5	27.8	0.02	4.18	n.a.	9.07	95.4
(small)	6	1	32.2	1.13	19.1	28.1	n.d.	4.15	n.a.	9.05	93.8
	6	2	33.0	1.66	19.3	27.3	0.02	4.17	n.a.	9.09	94.5
	7	1	33.1	1.11	19.6	27.6	n.d.	4.15	n.a.	9.06	94.6
	7	2	32.8	1.07	19.2	28.1	0.01	4.22	n.a.	8.53	93.9
Garnet -	1	1	36.3	0.03	20.4	39.9	0.22	0.82	1.71	n.a.	99.3
Bottom	1	2	35.4	0.02	20.5	41.2	0.026	0.94	1.16	n.a.	99.2
(large)	2	1	34.0	0.09	20.6	40.6	0.10	0.89	1.73	n.a.	98.0
	2	2	34.7	0.03	20.6	40.5	0.08	0.91	1.25	n.a.	98.0
	3	1	35.9	0.03	20.5	41.2	0.08	0.86	1.52	n.a.	100.1
	3	2	35.9	0.04	20.6	41.6	0.02	0.92	1.01	n.a.	100.1
Garnet -	1	1	36.3	0.03	20.2	41.6	n.d.	1.01	1.02	n.a.	100.1
Top	2	1	36.1	0.001	20.5	40.5	0.42	0.79	1.47	n.a.	99.9
(small)	2	2	35.5	0.03	20.5	41.1	0.01	0.92	1.15	n.a.	99.2
	3	1	36.1	0.04	20.4	41.2	0.06	0.94	1.21	n.a.	99.9
	3	2	36.1	0.02	20.3	40.8	0.03	0.89	1.13	n.a.	99.3

all values are weight percent oxides
[1]Total Fe as FeO
[2]Not analyzed
[3]Not detected

TABLE 3.3. PRIMARY TEXTURAL MEASURES

Statistic	Biotite		Garnet
	bottom(lg)	top(sm)	
Number of crystals	596	2239	337
Mean crystal volume (10^{-4} cm^3)	9.7	2.4	311
Median crystal volume (10^{-4} cm^3)	4.3	1.3	201
Maximum crystal volume (10^{-4} cm^3)	72	29	1560
Volume fraction	0.212	0.128	0.07
Number density (crystals/cm^3)	236	574	2.3
Mean nearest-neighbor separation (cm)	0.10	0.074	0.4

TABLE 3.4. ESTIMATED BULK COMPOSITION OF TWO LAYERS.

| Oxide	Bottom	Top
SiO$_2$	67.3	67.8
TiO$_2$	0.42	0.18
Al$_2$O$_3$	13.7	15.0
FeO	9.1	6.5
MnO	0.01	0.59
MgO	1.01	0.73
CaO	0.10	0.07
N$_2$O	n.a.	0.35
K$_2$O	3.5	4.1
Total	95.1	95.3
Fe/Mg	9.0	9.0

Values based on estimated modes and idealized mineral compositions (qtz, ilm) or mineral compositions from microprobe analysis (bio, grt, msc, chl).

TABLE 3.5. SIMULATION PARAMETERS AND RESULTS

Values for the inputs and output from thermally accelerated nucleation and growth simulations of biotite crystallization. Parameter descriptions are given in the text. The results "t_{95}" and "t_{95} - instantaneous" indicate the interval of crystallization required for 95% of the volume to be depleted such that its chemical affinity for the biotite-forming reaction decreased below the level required to nucleate new biotite. "Average dN/dt" is the nucleation rate calculated from the number of biotite crystals, the nucleation interval (t_{95}), and the sample volume.

	Units	bottom	top
Parameter			
T_{crit}	°C	350	350
dT/dt	K/m.y.	15	15
Q_D	kJ mol^{-1}	140	140
$[dN/dt]_{t=0}$	Nuclei s^{-1} cm^{-3}	3×10^{-21}	1×10^{-31}
D	cm^2 s^{-1}	5×10^{-7}	5×10^{-7}
	K^{-1}	0.2	0.35
Q_N	kJ mol^{-1}	750	1300
Result			
t_{95}	m.y.	14	13
t_{95} - instantaneous	m.y.	11	10
average dN/dt	Nuclei cm^{-3} m.y.$^{-1}$	19.1	47.8
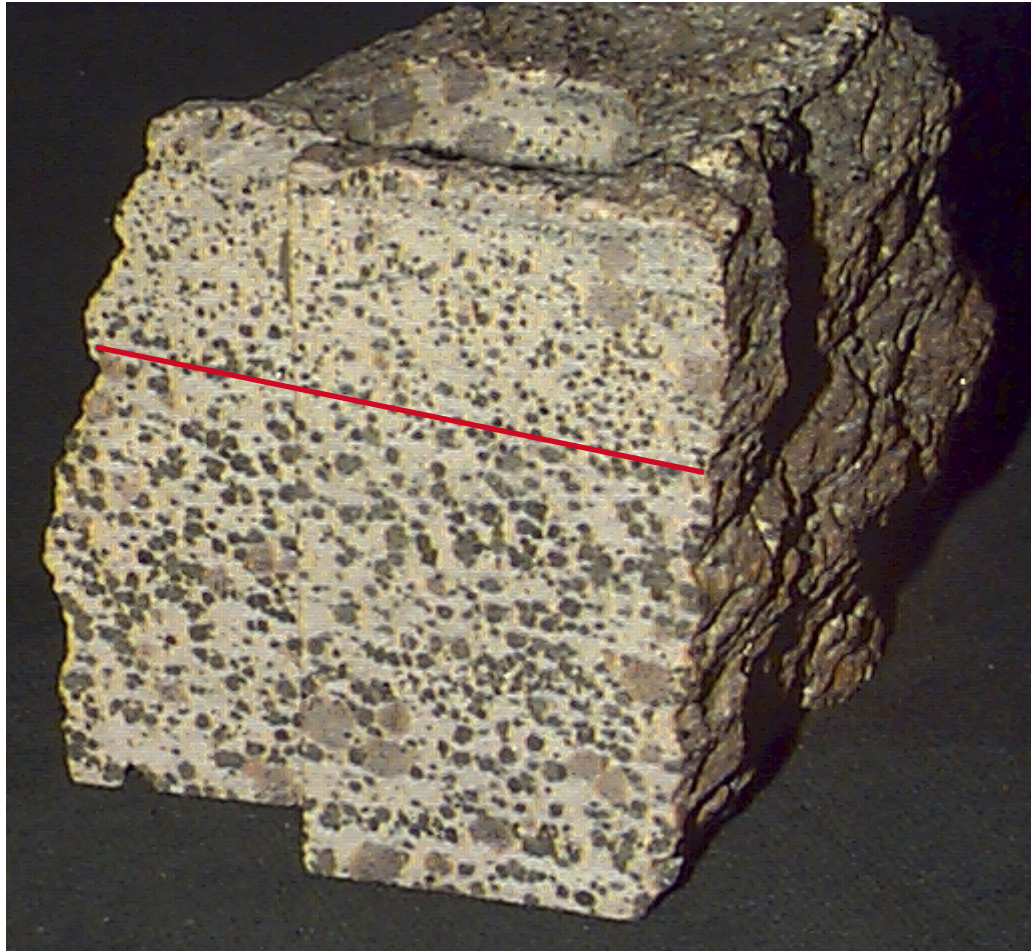
Figure 3.1. Photograph of sample HCR2-3 showing the layering in biotite crystal size, and the equant nature of the biotite porphyroblasts. The approximate location of the layer boundary is marked by a line.
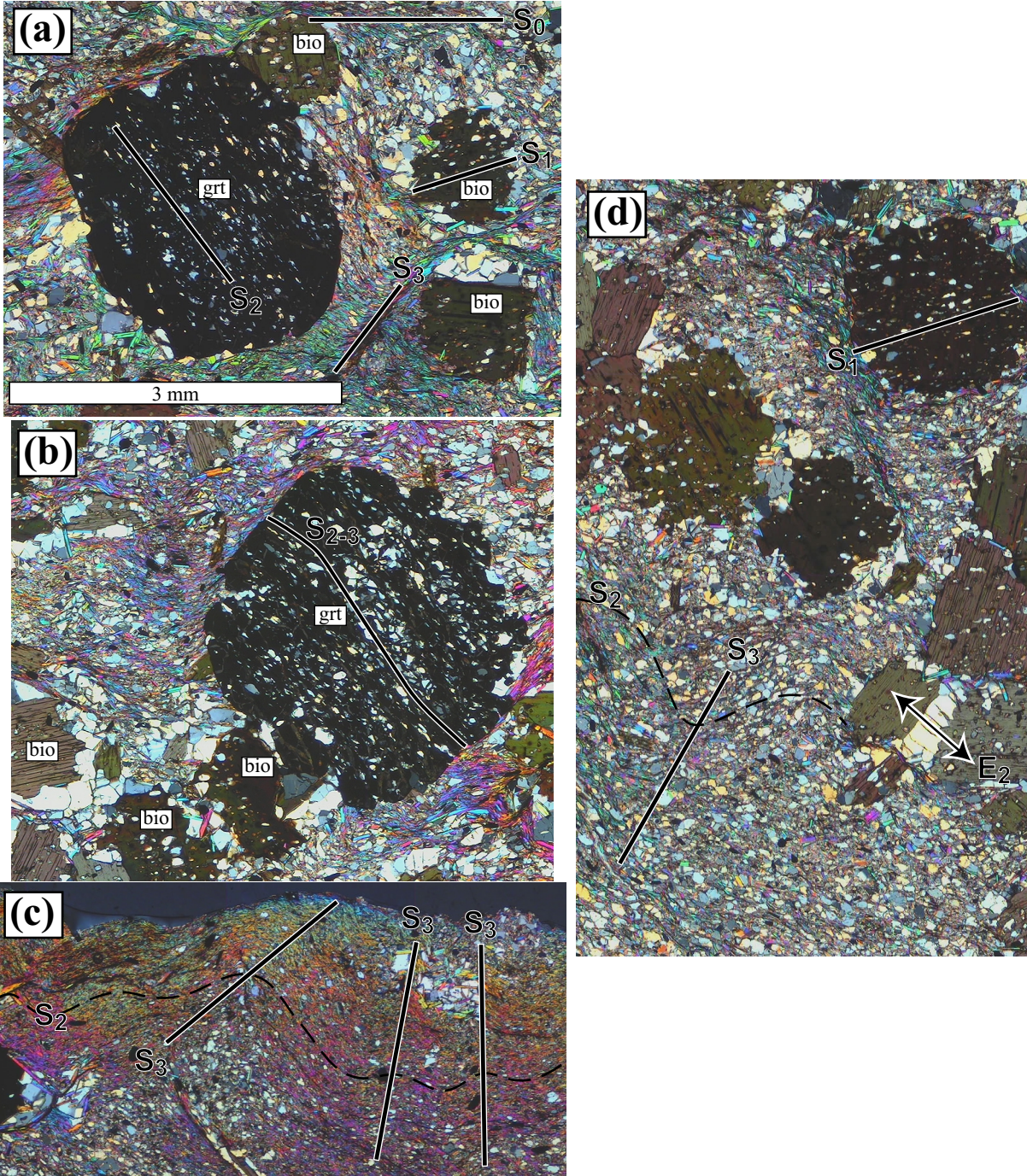
Figure 3.2. Photomicrographs of sample HCR2-3 illustrating the fabric orientations. The photomicrographs are the same scale and orientation, and represent different regions of a standard thin section. The garnets (grt) and some biotites (bio) are labeled. The dominant fabric found in the matrix is now sub-parallel to S_0, which is a compositional banding parallel to the biotite size-layering. Note that the biotites include a fabric sub-parallel to S_0, interpreted as S_1, while the garnets include a fabric at a high angle to S_0, interpreted as S_2. E_2 is a rarely-expressed extensional fabric in the biotite pressure shadows, sub-parallel to S_2. S_3 is a crenulation cleavage; the included S_2 fabric within the garnet in (b) shows incipient crenulation and is labeled S_{2-3}.
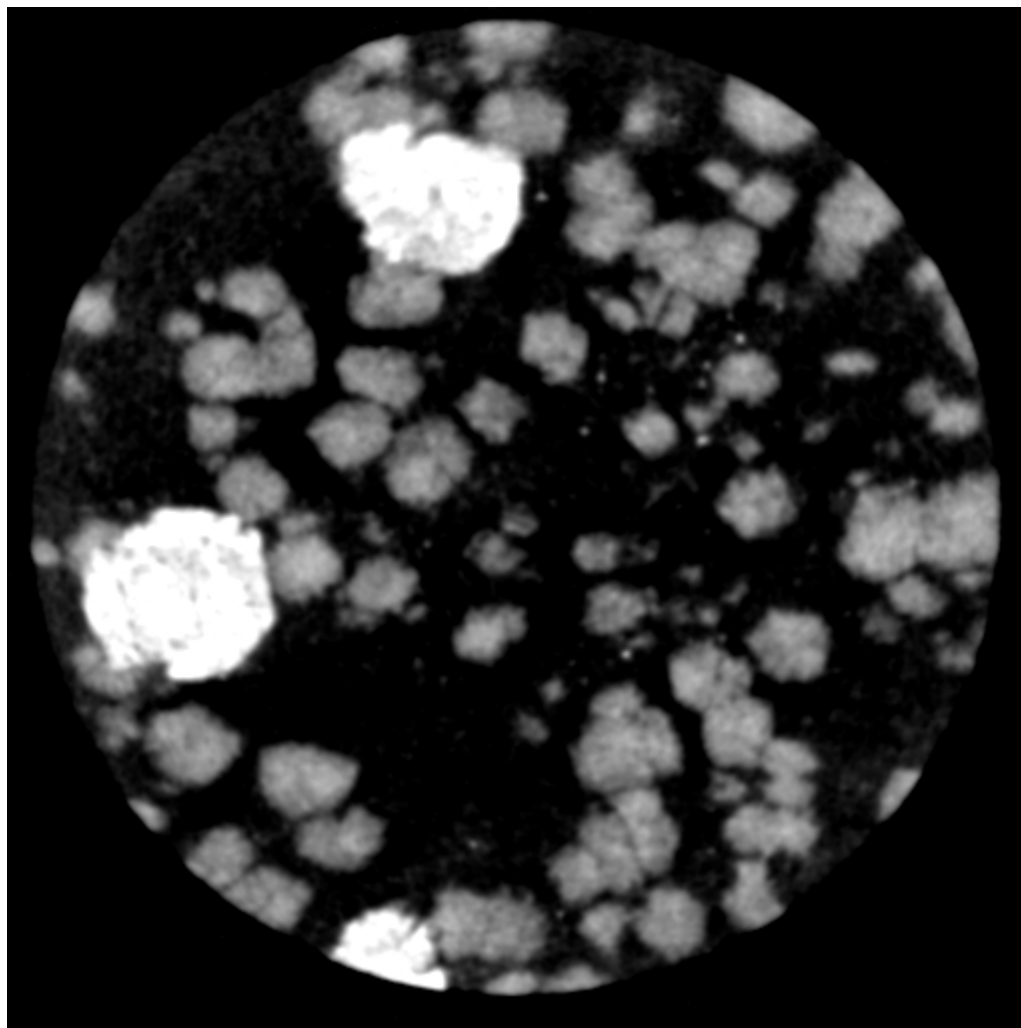
Figure 3.3. Typical high-resolution X-ray computed tomographic scan, representing a horizontal slice through a 2.5-cm diameter cylinder whose axis is oriented perpendicular to the size layering. The light objects are garnet, the gray objects are biotite, and the black insterstitial region is a matrix of fine-grained muscovite, quartz and feldspar.
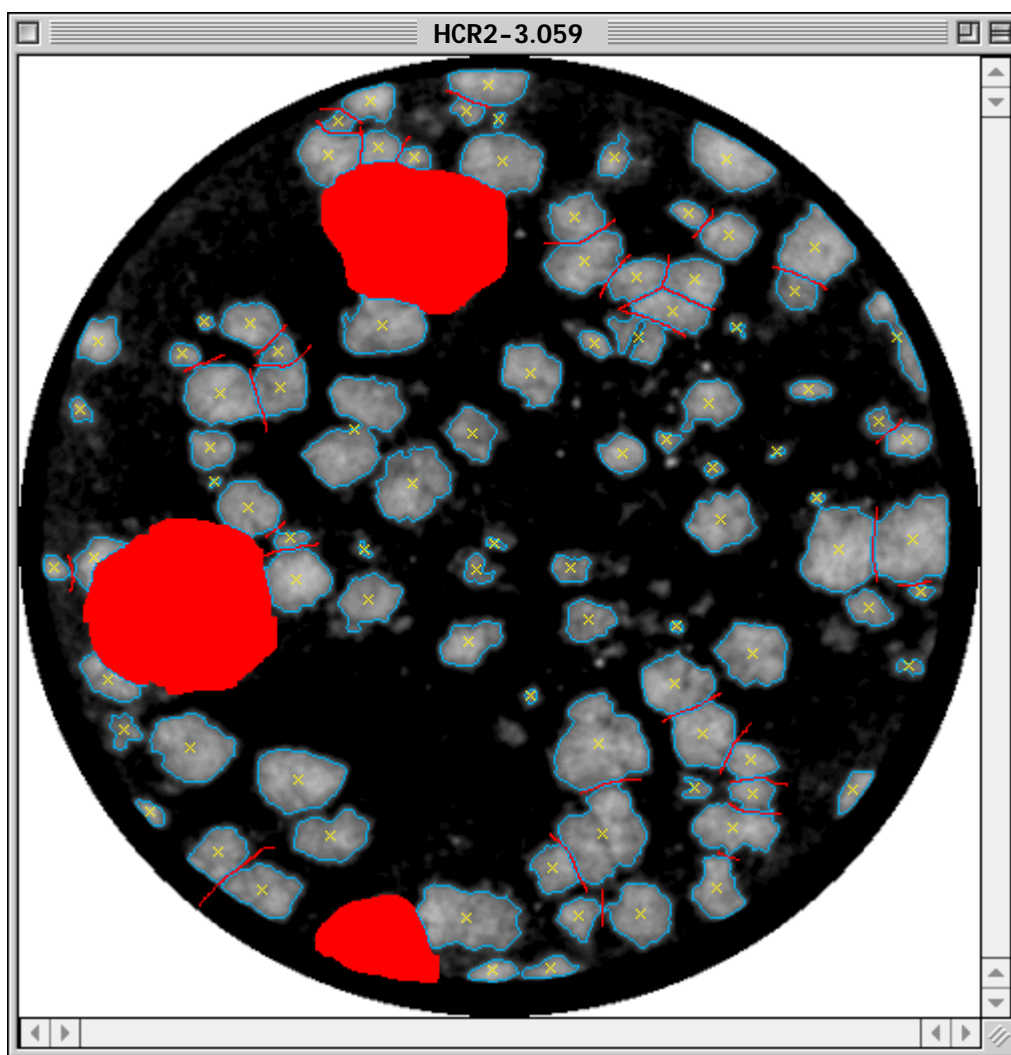
Figure 3.4. Screen capture during identification of individual biotite porphyroblasts in the scan slice of Figure 3.3. Note that garnets are masked (red) and are identified in a separate process. Each resulting biotite porphyroblast is marked by a blue outline and a yellow "x" in its sectional center of mass. Many biotites are in close contact, and although some in contact are easily distinguishable from this image alone (e.g., lower-right region), frequently images of the planes just above and just below are required to make the judgment as to whether a region represents a single biotite, or multiple biotites in contact (e.g., upper-right region). Thin-section observations are used frequently for reference during this process.
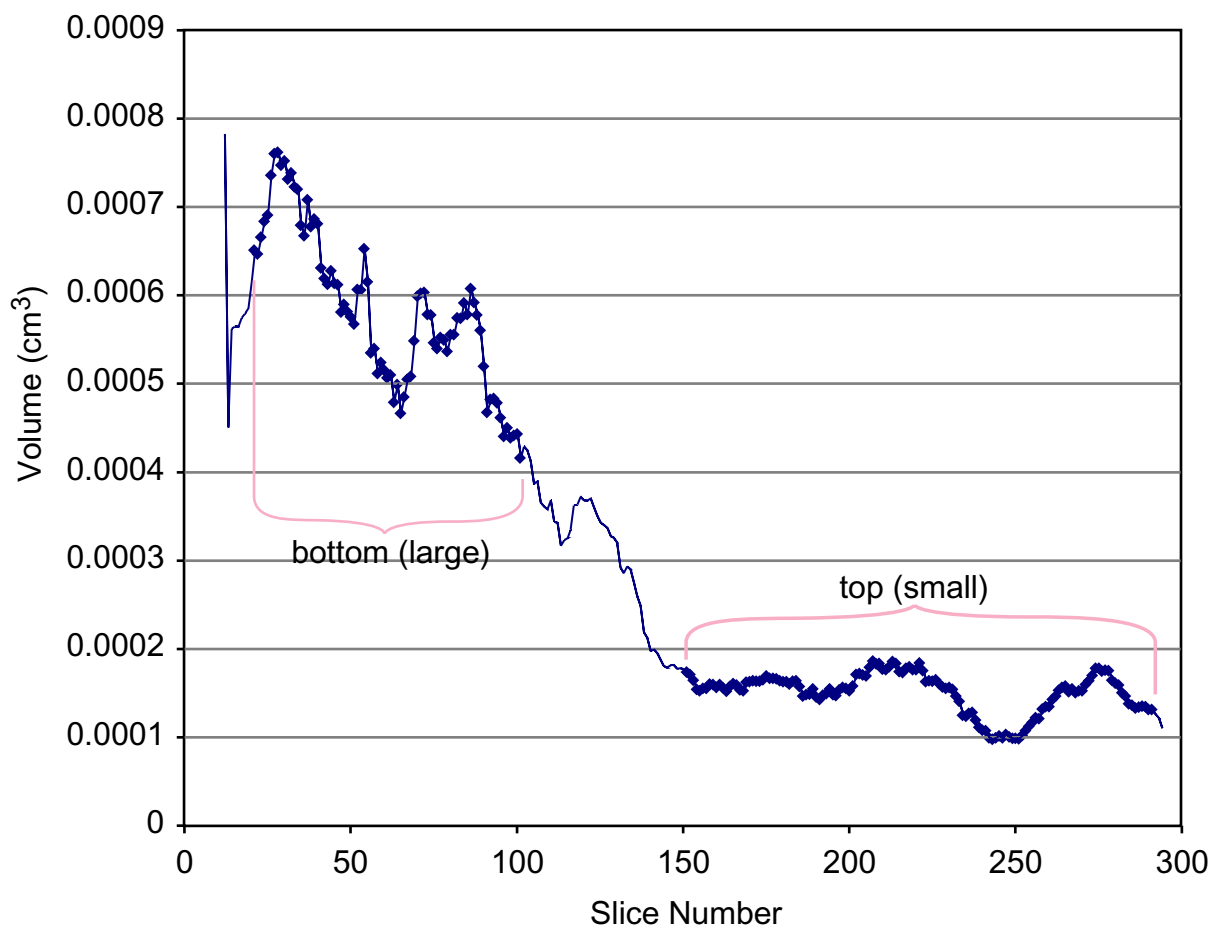
Figure 3.5. Mean biotite crystal volume as a function of position in specimen (slice number) in HCR2-3. Data were smoothed using a moving average over 21 slices. Sections of graph with diamond symbols indicate regions used for further analysis.
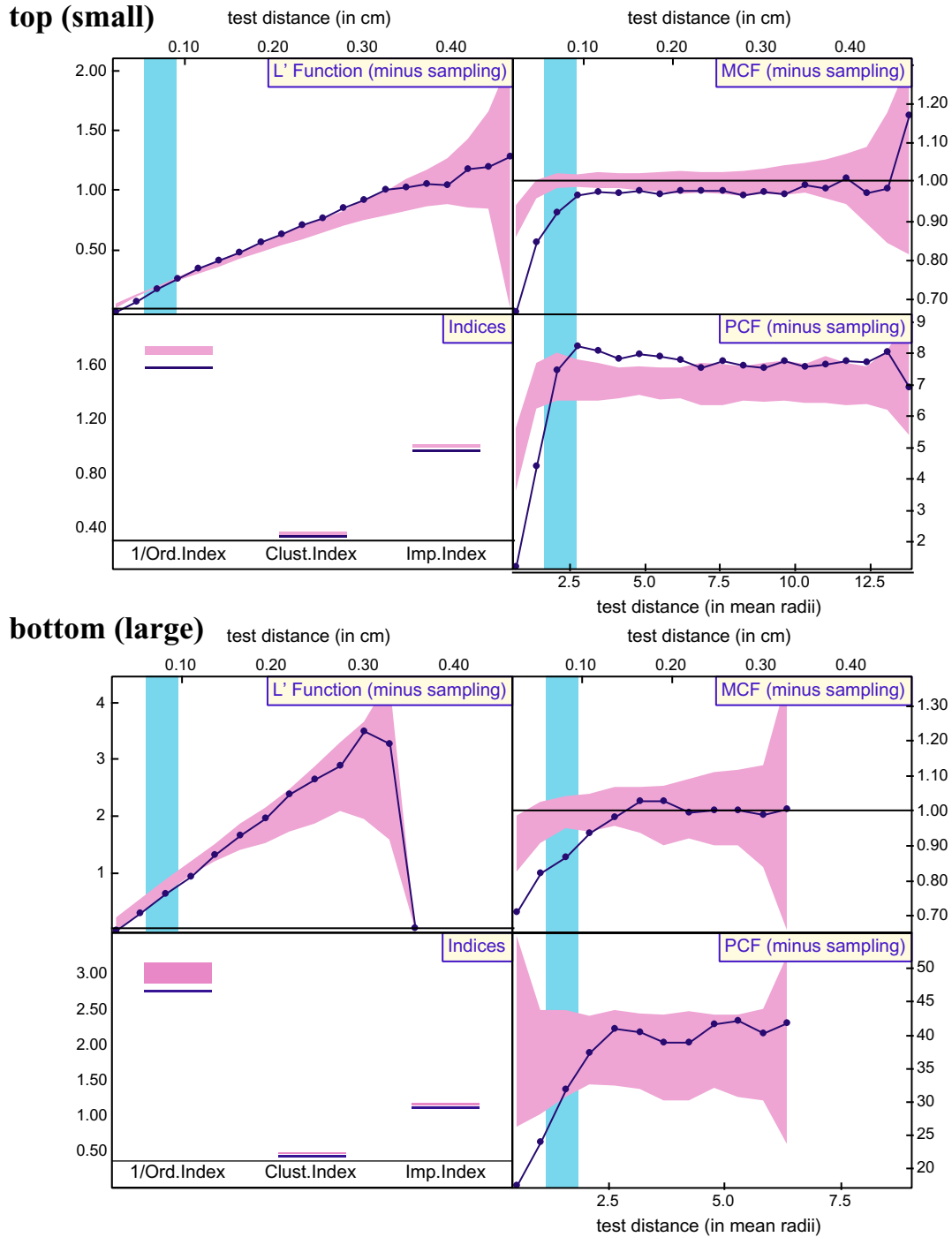
Figure 3.6. Results of statistical analysis of three-dimensional biotite size and location data sets for the two layers. Data values (dark blue curve) that fall below the null-hypothesis interface-controlled envelope (pink region) indicate ordering; data that fall above indicate clustering. Both layers show similar trends, with the exception that the top layer shows clustering of nucleation sites at scales slightly above the mean nearest-neighbor distance (blue vertical bar; centered on mean, width equal to 2σ).
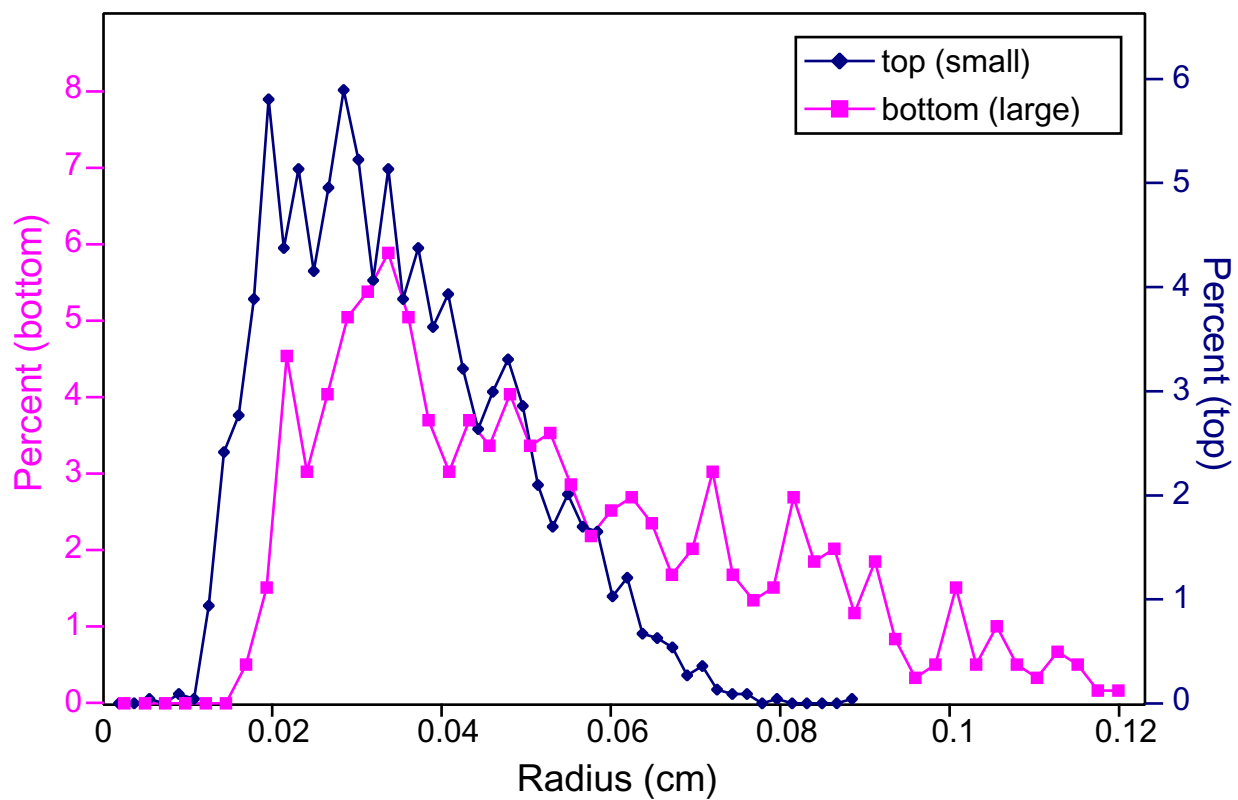
Figure 3.7. Crystal size distributions (CSDs) for the two layers, plotted so areas under curves are equal. This normalization is required because histogram bin sizes are narrower in curve for top layer.
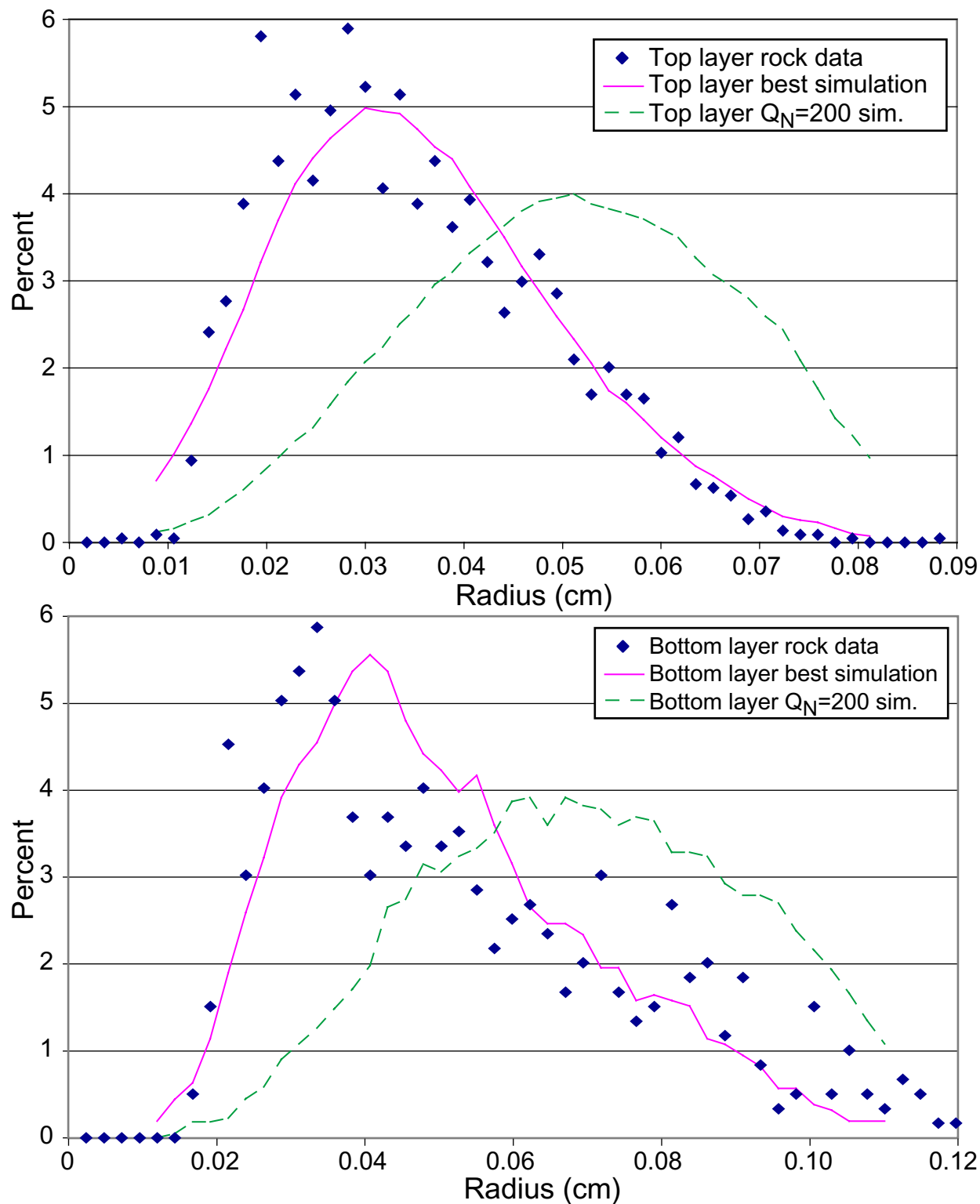
Figure 3.8. Crystal size distributions of top and bottom layers, best-fit simulations whose parameters are given in the text, and best-fit simulations with activation energy for nucleation of 200 kJ/mol. Simulation curves were smoothed with a moving average over 0.016 cm for the top layer, and 0.022 cm for the bottom layer. Note the relatively poor fits obtained using reasonable (200 kJ/mol) activation energies for nucleation.
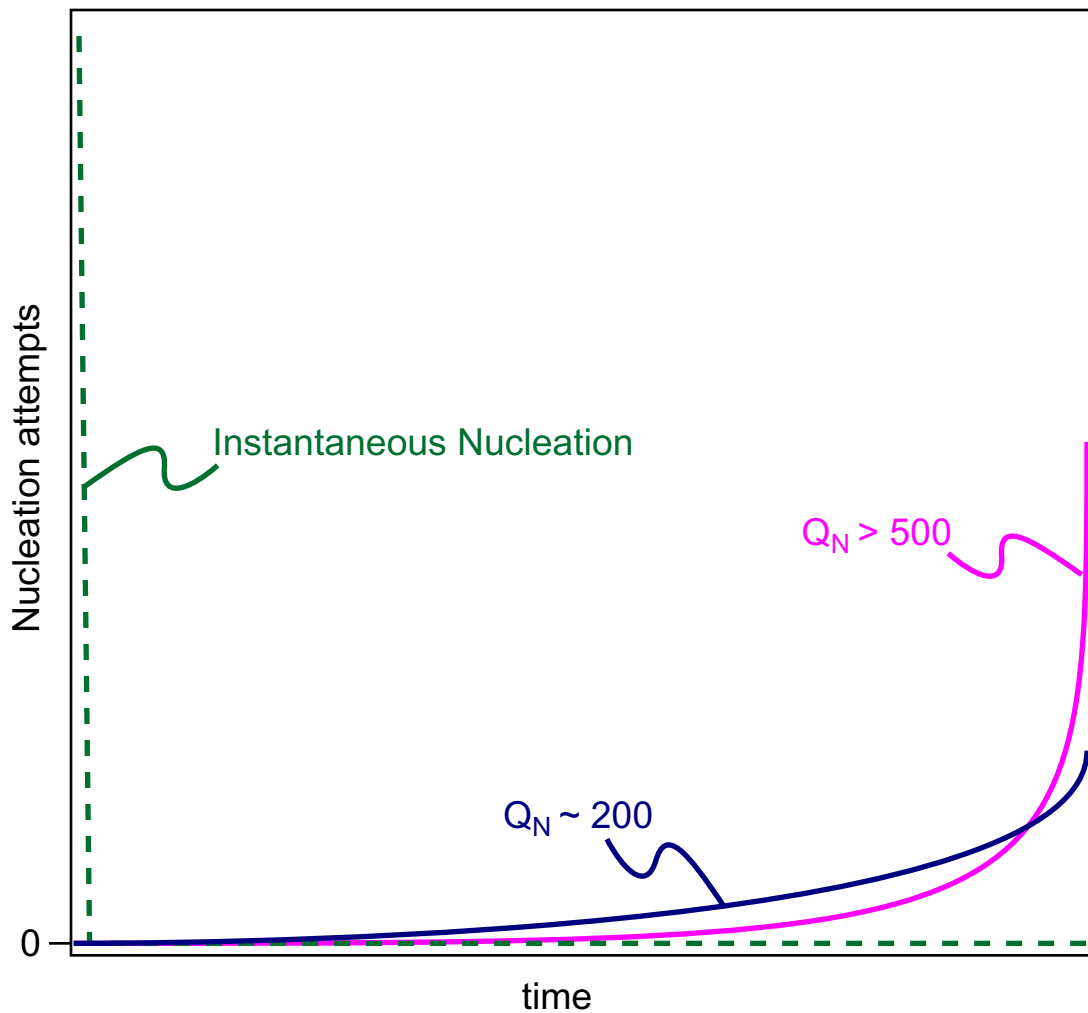
Figure 3.9. Schematic diagram of bracketing simulations used to constrain duration of crystallization episode. Instantaneous nucleation at the outset of a simulation produces the final set of nuclei at the initial time step, and crystallizes most rapidly. Simulations performed with the computational model that include an exponential dependence of nucleation rate upon temperature require unreasonably high values for Q_N, and produce many of the final set of nuclei at the end of the crystallization episode; these simulations require longer time spans for crystallization. Using more reasonable values of Q_N, the duration should be intermediate between these two extremes. Note that nucleation attempts represents the nucleation rate without considering the fraction of the rock already crystallized or diffusionally depleted; it can be conceptualized as the nucleation rate in the portions of the rock unaffected by crystallization.

APPENDIX 3A. DIFFUSION-CONTROLLED GROWTH OF GARNET

An analysis of tendencies towards ordering and clustering similar to that described in the text for biotite was also performed for garnet. Because garnet is present in larger, sparser crystals, a larger sample was required. The sample from which HCR2-3 was cored was analyzed. This sample was 147 cm^3, and 337 garnets were identified and located. The statistical analysis of Hirsch et al. (2000) was performed and the results show diffusional control of garnet nucleation and growth (Fig 3A.1).
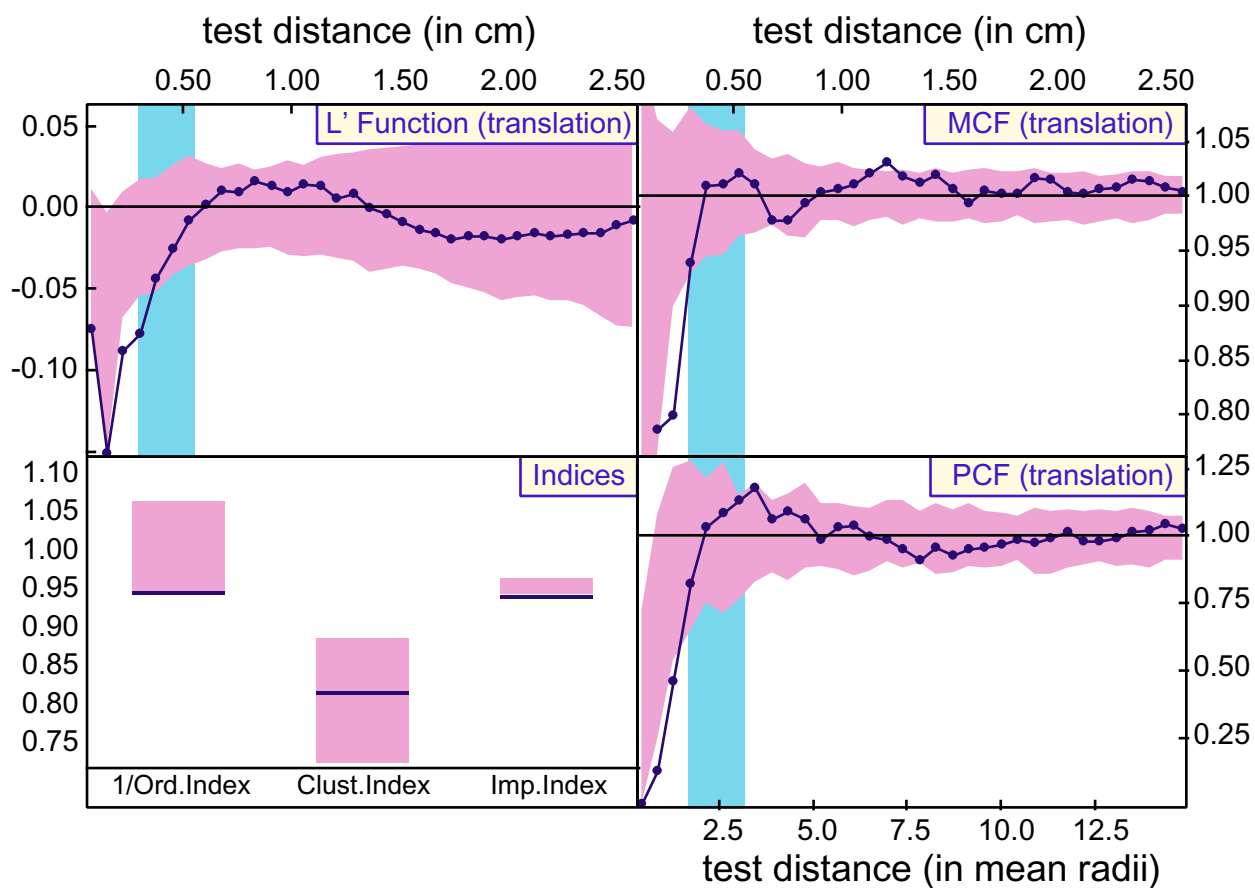
Figure 3A.1. Results of statistical analysis of three-dimensional garnet size and location data sets for the garnet population of the rock adjacent to sample HCR2-3. Data values (dark blue curve) that fall below the null-hypothesis interface-controlled envelope (pink region) indicate ordering; data that fall above indicate clustering. All statistics but the clustering index indicate diffusional control up to about the mean nearest-neighbor distance (blue vertical bar).

Chapter 4. Quantitative examination of variation in porphyroblast textures along a regional metamorphic field gradient

ABSTRACT

Garnet-bearing schists from the Waterville Formation of south-central Maine provide an opportunity to examine the factors governing porphyroblast size over a range of metamorphic grade. Three-dimensional sizes and locations for all garnet porphyroblasts were determined for three samples along the metamorphic field gradient spanning lowest garnet through sillimanite grade. Statistical analysis shows that the garnets in each rock crystallized in a diffusion-controlled nucleation and growth regime. Comparison of crystal size distributions to previous data sets obtained by stereological methods for the same samples reveals significant differences in mode, mean, and shape of the distributions.

Garnet-biotite Fe-Mg exchange thermometry provides peak temperatures of 480, 515, and 650 °C (all ± ~35°C), and garnet - aluminum silicate - quartz - plagioclase barometry provides a peak pressure estimate of 4.75 ± 0.8 kbar; these values were used to constrain pressure-temperature paths in numerical simulations of garnet crystallization in these samples. Numerical simulations of thermally accelerated, diffusion-controlled nucleation and growth for the three samples, which differ only in initial densities of nucleation sites and temperatures at the onset of nucleation, closely match measured crystal size distributions. This supports earlier predictions that post-crystallization annealing (Ostwald ripening) plays a negligible role in determining crystal size distributions; instead, an increase in crystal size and decrease in crystal number density is a direct consequence of increasing nucleation temperature, either as a result of decreasing spessartine content of garnet, or along a metamorphic field gradient.

This work confirms previous hypotheses linking the temperature at which a garnet begins to crystallize in a rock to the resulting crystal size: because nucleation is a function of the thermal overstepping and diffusion is a function of temperature, variation in the temperature of the garnet-forming reaction leads to variation in crystal size. This variation in the onset temperature of nucleation explains the observation of porphyroblast coarsening with metamorphic grade.

INTRODUCTION

The metamorphic crystallization of any phase places it on a continuum along which crystal number density varies inversely with crystal size. This variation reflects differences in the competition between the nucleation of new crystals and growth of pre-existing crystals (by diffusing material to the site of already-nucleated crystals). What controls whether a new phase in a rock crystallizes as a few large crystals or as numerous smaller ones? Metamorphic temperature has been correlated to crystal size, documenting the tendency for high-grade rocks to have relatively few, relatively large crystals, whereas lower-grade rocks generally contain more numerous, smaller crystals of the same phase (e.g., Spry, 1969, p. 125-127). In addition, an inverse correlation between garnet size and central Mn content has been frequently documented (e.g., Chinner, 1960; Carlson, 1989; Spear and Daniel, 1998). This work seeks to examine these correlations and explain their influence on garnet porphyroblast size. It is also possible to affect the distribution of crystal sizes after crystallization is complete, by the action of Ostwald ripening (post-crystallization surface-energy-driven coarsening of distributed grains), as suggested by Cashman and Ferry (1988); this study shows that such an explanation is unnecessary to explain the observed textures.

Much of this study rests on the connection between intensive variables during crystallization and the porphyroblast textures that result. Although this has been treated previously (Kretz, 1974; Walther and Wood, 1984; Carlson, 1989), a brief review is useful here. The relative rates of diffusion of chemical species to the site of a growing porphyroblast and attachment of those materials to the growing crystal will influence the spatial distribution and sizes of porphyroblasts in the rock. Slow diffusion relative to attachment will lead to a reduction in the chemical affinity for the reaction near the site of a growing porphyroblast, decreasing the probability of nucleation there. This suppression of nucleation near existing crystals can be detected by quantifying the ordering of porphyroblast centers. Similarly, slow diffusion will lead to a reduction in the size of nearby crystals, because neighboring crystals will compete with each other for nutrients when the diffusional domains from which they draw these nutrients impinge upon one another. This competition can be detected by quantifying size-separation correlations in the crystal array. Other factors, such as inhomogeneity in the distribution of nucleation sites or nutrients for garnet growth, can obscure the ordering and growth-suppression signals, if present.

This work focuses on garnet from three specimens representing a range of grades along a regional metamorphic field gradient, in which crystal size and number density vary. I examine some of the influences

on crystal size and crystal number density, and conclude that a prime influence is the temperature at which nucleation begins, supporting the hypothesis of Carlson (1999). Nucleation at higher temperatures leads to enhanced diffusion rate (a function of absolute temperature), but not necessarily enhanced nucleation rate (a function of thermal *overstepping* of the reaction). Variations in the temperature of onset of nucleation, or "critical temperature" (T_{crit}), may be due to a number of factors. Those examined here are variations in pressure-temperature paths (so the rock crosses the positively-sloped garnet-forming reaction at higher temperatures on a high-grade path) and variations in the spessartine content of the garnet (moving the garnet-forming reaction to lower temperatures with greater spessartine content).

SPECIMEN DESCRIPTION AND PETROGRAPHY

Samples were generously provided by J. Ferry, and derive from the Silurian Waterville Formation of south-central Maine, the metamorphic rocks of which consist of pelitic, semi-pelitic, and calcium-rich schists (1980). Metamorphic rocks are intruded by syn-metamorphic quartz monzonite stocks. Three samples were analyzed (Fig. 4.5): number 160A from just above the mapped garnet isograd, number 191A from the middle of the garnet zone, and number 711A from the sillimanite zone. Although these samples have been described previously as part of a larger suite (Ferry, 1980, 1982, 1984), the focus on them here warrants brief descriptions of them. These specimens were chosen because they were previously studied by Cashman and Ferry (1988), who concluded that their crystal size distributions and crystal number densities were strongly modified by post-crystallization annealing (Ostwald ripening). They are calcium-rich pelitic schists that experienced a single metamorphic episode, in which metamorphism followed most or all deformation (Ferry, 1980, p. 721). Sample 711A has the assemblage grt + bio + qtz + an + ilm + sil (abbreviations here and throughout follow Kretz, 1983). The feldspar is anorthite (Table 4.4); the sillimanite is fibrolitic, sparse and tiny, and best observed as inclusions within garnet; the garnet is euhedral to subhedral; and opaque minerals are abundant and fine-grained, present as inclusions within all the other phases as well as matrix grains (Fig. 4.1). Sample 160A has the assemblage grt + bio + an + cc + opaques, and the opaques are present as sparse, coarse-grained anhedral crystals (Fig. 4.2). This sample has both garnet inclusions and patchy retrogression, which appears not to have significantly altered the sizes of the garnets. Sample 191A has the assemblage grt + bio + msc + an + qtz + cc +opaques, and the garnets are subhedral to anhedral, with linear inclusion patterns and sparse inclusion-free rims (Fig. 4.3). Estimated modes are given in Table 4.1.

In samples 711A and 160A, the garnets have unusual inclusion patterns (Fig. 4.4). The regions of high inclusion density appear to correspond to dodecahedral edges and, depending on the particular section through the crystal, can show a range of morphology. These are likely due to variations in surface energies in particular directions during garnet growth.

PETROLOGY

Modeling of the nucleation and growth of garnet in these rocks requires estimates both for the temperature at the onset of garnet nucleation and for the (pressure-) temperature-time path, to model the heating rate. Ferry (1980) performed electron microprobe chemical analysis and garnet-biotite geothermometry on these and nearby rocks, as well as geobarometry using barometers based on intersecting equilibria. However, the availability of more recent calibrations of the garnet-biotite thermometer suggested the need for new estimates of temperature and potentially pressure as well.

Mineral compositions of garnet, biotite, and feldspar were obtained by electron microprobe analysis in order to perform garnet-biotite geothermometry and garnet-quartz-sillimanite-plagioclase geobarometry. Analyses were performed using the JEOL 733 Superprobe electron microprobe using a 15 kV accelerating voltage and a beam current on brass of 20 nA. Counting times for each element terminated at 40s or after accumulation of 100,000 counts. Best analyses (based on weight percent totals) are listed in Tables 4.2, 4.3, and 4.4; for garnet analyses, points are labeled as either core or rim analyses. Averages were also computed for thermobarometry purposes; these represent at least two crystals, and comprise from 3-13 individual analyses (most comprise from 7-13 analyses). Weight percent totals for the average analyses are 1-2% lower than "best" analyses. There is little variation among crystals in the mineral composition for each sample.

These data were converted into mole fractions of garnet end-members by normalizing to 8 cations; ferrous iron was calculated as Fe_{total}–(2–Al). Calculation of spessartine content is important for estimation of the temperature of onset of garnet nucleation, as discussed below.

As demonstrated by the variation in modes and assemblage among the three samples, there is significant variation in the bulk composition of the rocks of the Waterville Formation. This variation precludes definite determination of the garnet-forming reaction in these three samples, and raises the question of whether they experienced the same garnet-forming reactions. In the absence of any external constraints, the simplest case of a single garnet-forming reaction was used. Probably the simplest plausible reaction, given the measured garnet composition, is *chlorite + muscovite + wollastonite + anorthite + calcite = garnet*

+ *biotite* + H_2O + CO_2. An attempt was made to compute the position of this reaction in pressure-temperature space for various spessartine contents of garnet, but problems with computing the activity-composition relations for Mn-chlorite have so far frustrated this attempt. Spear and Cheney (1989) produced a petrogenetic grid with isopleths of Mn-content for the garnet-forming reaction *chloritoid + biotite = garnet + chlorite*, and although this was probably not the exact garnet-forming reaction in these rocks, the variation in temperature that corresponds to variation in spessartine content is likely to be similar for a number of garnet-forming reactions. This is because, as Mn is incorporated into the system, the free-energy change in the garnet will be identical among reactions, and the free-energy changes in other phases are likely to be broadly similar to those for chlorite (or whatever the true Mn-bearing reactants were). The temperature at which the postulated pressure-temperature path for each of the three samples intersects the appropriate isopleth of spessartine for the measured garnet core composition is chosen as the best available estimate of the temperature at which garnet crystallization began (Fig. 4.6). These temperatures are 455°C for sample 711A, 410°C for sample 160A, and 375°C for sample 191A.

Although the peak temperature experienced by each sample is not as important to the modeling of its porphyroblast texture as is the onset temperature for garnet nucleation (models typically conclude nucleation and growth well before peak temperatures are attained), peak conditions help to constrain model pressure-temperature paths. Analyses for geothermometry were obtained from garnet rims and matrix biotites distant from garnet surfaces in the two dimensions recorded by the thin section, in order to obtain peak temperatures (Fig. 4.7). For each rock, average compositions representing several analyses (Tables 4.2 and 4.3) were used as input to the garnet-biotite geothermometer of Holdaway (2000). This calibration of the garnet-biotite geothermometer, which is better able to account for high-Mn compositions than its predecessors, calculates temperatures for these samples 100-200 °C higher than those obtained with other calibrations (Ferry and Spear, 1978; Hodges and Spear, 1982; Perchuk and Lavrent'eva, 1983; Berman, 1990). The Holdaway temperature values are more reasonable than those from other calibrations in light of the isograd pattern; for example, other calibrations yield temperatures for the sillimanite-zone sample, 711A, in the range 443 - 505 °C, below the sillimanite stability field of Holdaway (1971), whereas the Holdaway (2000) calibration gives a temperature of ~650°C, well within the sillimanite stability field. The Holdaway (2000) thermometer provides temperatures of ~570°C for sample 191A and ~535°C for sample 160A. The uncertainty of these values was estimated from pairs of garnet and biotite analyses that yield the highest and lowest possible values for $[(Fe/Mg)_{bio}/(Fe/Mg)_{grt}]$. The range of values indicates an uncertainty of approximately ±25°C.

Uncertainty in the calibration is estimated to be the same, about 25°C (Holdaway, 2000), so net uncertainty (assuming independent errors) is estimated at 35°C.

Feldspar and garnet from sample 711A were used to calculate a pressure for this rock using garnet-aluminum silicate-quartz-plagioclase (GASP) barometry. This was hampered by the high spessartine content (X_{sps}=0.28) relative to pyrope (X_{pyp}=0.08) of the garnet, placing the composition slightly out of the recommended range from the application of the GASP barometer ($X_{sps}/X_{pyp} < 3$). However, because no other geobarometers were available for these samples, the calibrations of Newton and Haselton (1981), and Koziol and Newton (1988) were used. These provided pressures of 4.4 and 4.9 kbar, respectively, for sample 711A. These values are significantly greater than the 3.5 kbar estimate determined by Ferry (1980). Note that the specific pressures do not have much impact on the modeling. Changes in pressure affect the modeling only insofar as they alter either the temperature of onset of nucleation or the heating rate, and the modeling conclusions, as discussed below, rely on *differences* in critical temperature for nucleation among samples. Notably, if all three samples were modeled with a single pressure-temperature path intermediate to those in Figure 4.6, T_{crit} would be altered by no more than 8 °C in any case, and differences in T_{crit} among samples would be altered by no more than 6 °C. Thus, the error introduced by the use of the GASP barometer for compositions outside the calibration does not greatly affect the conclusions, nor does the choice of the GASP pressure over the 3.5 kbar value from Ferry (1980).

DATA COLLECTION

The data required for the quantitative analysis of textures are three-dimensional: knowledge of the sizes and locations of all porphyroblasts in the sample volume. For this study, such data were obtained using the high-resolution X-ray computed tomographic scanner at The University of Texas at Austin, Department of Geological Sciences. The data are extracted from a set of grayscale images, in which brightness roughly correlates to density. A typical scan image from each sample is shown in Figure 4.8; scanning parameters are documented in Table 4.5.

For each sample, the garnet crystals are first located in each slice using the BLOB program (Appendix), in which contiguous regions of a user-determined range of grayscales are identified, and their areas and centroid locations are recorded. These sections through each crystal are integrated into 3-D objects using the program INTEGRATE (Appendix), in which the stacks of 2-D sections are combined using heuristics and user decisions into separate 3-D regions, whose volumes and 3-D centroid locations are recorded.

RESULTS

Primary Textural Measures

Primary measures of textural features of the garnet porphyroblasts (Table 4.6) offer insight into the nature of the observed textural variation with metamorphic grade. These data reveal that the specimens' monotonic changes in crystal size, volume fraction, nearest-neighbor separation, etc. do not correlate with sample location relative to the isograds (Fig. 4.5), and thus are not correlated with peak metamorphic conditions.

Statistical Analysis

Quantitative modeling of porphyroblast textures requires identification of the rate-controlling step in the nucleation-and-growth process, which can be determined from statistical analysis of the three-dimensional array of porphyroblast sizes and locations (Kretz, 1973; Carlson, 1989). The method of statistical analysis used here has been detailed elsewhere (Hirsch et al., 2000), but a brief review is merited here.

For each sample, a number of statistics are measured that are sensitive to ordering of crystal centers or to correlations between crystal size and separation. Among these are both single-scale statistics and scale-dependent correlation functions. These statistics are measured first on the data set for the rock, and then on each of 100 interface-controlled crystallization simulations constructed to share as many features as possible with the rock's data set. These 100 results for each statistic constitute a "null-hypothesis region" for the statistic, to which the value measured on the rock's data set can be compared in order to test if the interface-controlled hypothesis can be rejected. Values for the function or statistic that fall below the null-hypothesis region indicate, with 95% confidence, excess ordering of crystal centers or reduced crystal size relative to that expected for an interface-controlled nucleation and growth history. These negative excursions indicate diffusional controls on nucleation (ordering of crystal centers) and growth (reduced crystal size).

All measured statistics agree for each sample, falling below the interface-controlled null-hypothesis region at scales up to about the mean nearest-neighbor distance (Figs. 4.9, 4.10, 4.11). These data indicate ordering and suppression of growth in all three samples, which implies diffusional control on nucleation and growth of garnet porphyroblasts in all three rocks. Although these data strongly support diffusional control of nucleation and growth, further evidence for diffusion-controlled growth could be potentially obtained from radius-rate analysis (Kretz, 1974; Carlson, 1989) of garnet zoning patterns. Although zoning in the analyzed

crystals appears to be minor, the chemical analyses were not performed on central sections through the crystals, and thus the true zoning profiles may be significantly steeper than the core/rim data imply (Table 4.2).

Textural modeling

The identification of diffusional controls on nucleation and growth allows forward modeling of the textures using the computational model of Carlson et al. (1995). This numerical model incorporates explicit time and temperature variables, and its inputs include the activation energies and pre-exponential constants for nucleation and diffusion, the temperature of onset of porphyroblast growth, and the prograde heating rate. The heating rate was taken to be 10°C/m.y. for all samples; although the actual heating rate is likely to have varied among the samples, the lack of constraints on this parameter led to the choice of an identical value for the three samples. The value chosen is within the range of heating rates obtained from thermal modeling of regional metamorphism (e.g., Spear, 1993, Fig. 3-12b). The critical temperature was obtained from the spessartine content of the garnet, in combination with the Spear and Cheney (1989) calibration of their garnet-forming reaction (Fig. 4.6). The activation energy for diffusion was taken as 140 kJ/mol, a value derived by Farver and Yund (1998) for bulk diffusion of Si in hydrous novaculite. Although Al diffusion is likely the rate-limiting process, this Si diffusion measure is presently the best available estimate for Al diffusion. The previous estimate for the activation energy for diffusion used in published work (e.g., Carlson et al., 1995) was 84 kJ/mol, from Fisher (1977), and was estimated from published data for grain-boundary diffusion in metals and unpublished data for calc-silicate nodule development.

The model was computed iteratively, adjusting input parameters until the resulting crystal size distributions closely matched those of the rock sample (Fig. 4.12). The only simulation parameters that differ among the three samples are the temperature of onset of nucleation and the initial nucleation rate, $[dN/dt]_{t=0}$ (Table 4.7). The activation energy for nucleation, Q_N, is linked to the input variable   (an acceleration factor relating nucleation rate to thermal overstepping of the reaction), given a temperature of interest (Carlson et al., 1995, Fig. 6), and the values of Q_N that correspond to   for each sample are 375, 350, and 315 kJ/mol for samples 711A, 160A, and 191A, respectively. Although little is known about nucleation kinetics during metamorphism, these values seem broadly reasonable: for garnet in these samples, nucleation must be difficult, or it would not crystallize as porphyroblasts.

The variation in $[dN/dt]_{t=0}$, the initial nucleation rate, may not be merely an artifact of the modeling; rather, it corresponds to petrographic observations. One might expect the initial nucleation rate to be a function of the density of nucleation sites, and for this density to be inversely related to grain size. Although there would certainly have been changes in mean matrix grain size during and after garnet nucleation, current matrix grain size may bear some relation to grain size during garnet nucleation, and therefore, to $[dN/dt]_{t=0}$. The average grain diameter of biotite crystals (the only phase other than garnet present in all three specimens) in the three samples decreases from sample 160A, which has the smallest value for $[dN/dt]_{t=0}$, to sample 191A, which has largest value for $[dN/dt]_{t=0}$ (Figs. 4.1 - 4.3, Table 4.6). The biotite in these rocks is somewhat porphyroblastic, however, and the matrix minerals (qtz + an + opaques in 711A, cc + an in 160A, and an + qtz in 191A) do not show as clear a gradation in grain size.

The close matches to observed textures obtained from simulations using the parameters given in Table 4.7 suggest that those values may be near the actual values governing the crystallization of these garnet samples. Exploratory attempts to match observed textures, but varying Q_D by a factor of two in either direction (70 and 280 kJ/mol) produced significantly poorer fits of crystal size distributions than those of Figure 4.12. This suggests that 140 kJ/mol is not far from the true value of the activation energy for diffusion operating during the crystallization of these samples. Similar exploratory numerical simulations varying heating rate by a factor of two (5 and 20 °C/m.y.) produced mixed results. For sample 711A, the fits of crystal size distributions were somewhat improved at *both* the faster and slower heating rates. For sample 160A, the faster heating rate produced an improved fit, while the slower heating rate produced a somewhat poorer fit. For sample 191A, both the faster and slower heating rates produced somewhat poorer fits. These results suggest that although the conclusions are not strongly dependent on the particular choice of heating rate, minor improvements in fits of simulated crystal size distributions to observed distributions may be obtained through more sophisticated modeling of regional metamorphic temperature-time histories.

DISCUSSION

Comparison to previous studies

These particular samples have been examined previously, as part of a study of Ostwald ripening (Cashman and Ferry, 1988). Ostwald ripening is a process driven by reduction in surface free energy, in which distributed crystals are annealed. It results from differences in surface free energy between large and small grains that drives diffusion of material from the small grains to the large grains. Cashman and Ferry

(1988) postulated initially linear log-normalized crystal size distributions of the type shown in Figure 4.13, and called upon Ostwald ripening to remove large numbers of smaller crystals.

Cashman and Ferry (1988) used stereological techniques to infer three-dimensional crystal size distributions from two-dimensional distributions. The crystal size distributions they calculated show significant differences with those documented above (Fig. 4.13), measured from the three-dimensional data sets obtained through high-resolution X-ray computed tomography. The most notable difference is in the maximum crystal size documented. This difference likely does not stem from the stereology method used in Cashman and Ferry (1988), that of Saltykov (1967), because the large-sized crystals also are documented in their 2-dimensional sectional data set. Barring any systematic errors, this difference can only be due to real differences between the samples. Although the analyses were performed on the same hand samples, the analyzed regions are separated by up to ~7 cm.

The crystal size distributions measured in this study (both the shapes of the individual distributions and the variation among the distributions for the three specimens) do bear a broad resemblance to those calculated by Cashman and Ferry (1988), and could be regarded as evidence for Ostwald ripening (Fig. 4.14). However, Carlson (1999) demonstrated that surface free energy reduction is highly unlikely to have a significant effect on aluminous porphyroblasts for grain sizes above micron-scale, due to the small surface energy driving forces for intergranular diffusion at these grain sizes. Moreover, Ostwald ripening is not required in order to explain crystal size distributions of the sort observed in these samples; they are common products of a thermally accelerated nucleation and growth process, as has been noted before (Carlson, 1991; Carlson et al., 1995). Nor is Ostwald ripening required to produce the variation among the samples in their crystal size distributions. As this work shows, these can be produced by variations in the critical temperature for nucleation and the initial number of nucleation sites. In the present simulations, the variation in T_{crit} is linked both to the spessartine content of the garnet and the pressure-temperature path the garnet followed, as predicted by Carlson (1999).

Cashman and Ferry (1988, p. 411 and Fig. 6) link the degree of annealing to increasing grade, using the three samples studied here along with a chlorite zone sample. However, these samples *lack* the usual correlation between metamorphic grade and porphyroblast size - their "middle annealed" sample of the three (160A), is actually the lowest-temperature of the three, as is evident from the sample location map (Fig. 4.5) and the peak temperatures calculated in this study (although in Table 1 of Cashman and Ferry, identical peak temperatures of 450°C are given for both 160A and 191A).

Implications for nucleation and diffusion

These results offer the first evidence in support of the hypothesis (Carlson, 1999) that increases in of porphyroblast grain sizes with increasing metamorphic temperature can be a consequence solely of variation in the temperature of onset of nucleation. Variation in this temperature is important because it controls the interplay between diffusional growth of pre-existing crystals and nucleation of new crystals, both of which act to reduce the free energy of the rock. Diffusion rate is a function of temperature while nucleation rate is a function of thermal overstepping of the garnet-forming reaction. Thus, two rocks at a given temperature will, in general, have identical diffusion rates, but may have quite different nucleation rates (in the undepleted portions of the rock). The rate of nucleation will depend on the degree to which the temperature of the garnet-forming reaction is exceeded in each rock.

CONCLUSIONS

These data document significant textural differences among the three garnet schists examined. Cashman and Ferry (1988) sought to explain the textural differences among these samples as a consequence of differential degrees of Ostwald ripening. These results demonstrate that Ostwald ripening is not required to produce the porphyroblast textures observed. Moreover, the textures can be produced solely by differences in the critical temperature for nucleation and the initial nucleation rate, even for samples of varying bulk composition, highlighting the influence of the temperature of onset of nucleation in determining porphyroblast textures. This work for the first time documents that an increase in porphyroblast size with metamorphic grade can be a consequence of differences in the temperature at which the porphyroblast begins to crystallize.

ACKNOWLEDGEMENTS

REFERENCES CITED

Barker, D. S., 1961. Hallowell granite and associated rocks, South-Central Maine. *Unpub. Ph.D. Thesis, Princeton University, Princeton, NJ.*

Berman, R. G., 1990. Mixing properties of Ca-Mg-Fe-Mn garnets. *American Mineralogist*, **75**, 328-344.

Carlson, W. D., 1999. The case against Ostwald ripening of porphyroblasts. *The Canadian Mineralogist*, **37**, 403-413.

Carlson, W. D., 1991. Competitive diffusion-controlled growth of porphyroblasts. *Mineralogical Magazine*, **55**, 317-330.

Carlson, W. D., 1989. The significance of intergranular diffusion to the mechanisms and kinetics of porphyroblast crystallization. *Contributions to Mineralogy and Petrology*, **103**, 1-24.

Carlson, W. D., Denison, C. and Ketcham, R. A., 1995. Controls on the nucleation and growth of porphyroblasts; kinetics from natural textures and numerical models. *Geological Journal*, **30**, 207-225.

Cashman, K. V. and Ferry, J. M., 1988. Crystal size distribution (CSD) in rocks and the kinetics and dynamics of crystallization. *Contributions to Mineralogy and Petrology*, **99**, 401-415.

Chinner, G. A., 1960. Pelitic gneisses with varying ferrous/ferric ratios from Glen Clova, Angus, Scotland. *Journal of Petrology*, **1**, 178-217.

Farver, J. R. and Yund, R. A., 1998. Bulk diffusion of selected cations in a natural quartz aggregate. *Eos, Transactions of the American Geophysical Union*, **79**, 369.

Ferry, J. M., 1984. A biotite isograd in south-central Maine, U.S.A.; mineral reactions, fluid transfer, and heat transfer. *Journal of Petrology*, **25**, 871-893.

Ferry, J. M., 1982. A comparative geochemical study of pelitic schists and metamorphosed carbonate rocks from south-central Maine, USA. *Contributions to Mineralogy and Petrology*, **80**, 59-72.

Ferry, J. M., 1980. A comparative study of geothermometers and geobarometers in pelitic schists from South-central Maine. *American Mineralogist*, **65**, 720-732.

Ferry, J. M. and Spear, F. S., 1978. Experimental calibration of the partitioning of Fe and Mg between biotite and garnet. *Contributions to Mineralogy and Petrology*, **66**, 113-117.

Fisher, G. W., 1977. Nonequilibrium thermodynamics in metamorphism. In: *Thermodynamics in geology* (ed Fraser, D. G.), pp. 381-403, Oxford, United Kingdom.

Hirsch, D. M., Ketcham, R. A. and Carlson, W. D., 2000. An evaluation of spatial correlation functions in textural analysis of metamorphic rocks. *Geological Materials Research*, **2**, 1-41.

Hodges, K. V. and Spear, F. S., 1982. Geothermometry, geobarometry and the Al_2SiO_5 triple point at Mt. Moosilauke, New Hampshire. *American Mineralogist*, **67**, 1118-1134.

Holdaway, M. J., 2000. Application of new experimental and garnet Margules data to the garnet-biotite geothermometer. *American Mineralogist*, **85**, 881-892.

Holdaway, M. J., 1971. Stability of andalusite and the aluminum silicate phase diagram. *American Journal of Science*, **271**, 97-131.

Koziol, A. M. and Newton, R. C., 1988. Redetermination of the anorthite breakdown reaction and improvement of the plagioclase-garnet-Al_2SiO_5-quartz geobarometer. *American Mineralogist*, **73**, 216-223.

Kretz, R., 1983. Symbols for rock-forming minerals. *American Mineralogist*, **68**, 277-279.

Kretz, R., 1974. Some models for the rate of crystallization of garnet in metamorphic rocks. *Lithos*, **7**, 123-131.

Kretz, R., 1973. Kinetics of the crystallization of garnet at two localities near Yellowknife. *Canadian Mineralogist*, **12**, 1-20.

Newton, R. C. and Haselton, H. T., 1981. Thermodynamics of the garnet-plagioclase-Al_2SiO_5 -quartz geobarometer. In: *Thermodynamics of minerals and melts - Advances in physical geochemistry* (eds Newton, R. C., Navrotsky, A., Wood, B. J. and Saxena, S. K.), pp. 131-147, Springer, New York.

Perchuk, L. L. and Lavrent'eva, 1983. Experimental investigation of exchange equilibria in the system cordierite-garnet-biotite. In: *Kinetics and Equilibrium in Mineral Reactions* (ed Saxena, S. K.), pp. 199-239, Springer, New York.

Saltykov, S. A., 1967. The determination of the size distribution of particles in an opaque material from a measurement of the size distribution of their sections. In: *Stereology, Proceedings of the 2nd International Congress for Stereology* (ed Elias, H.), pp. 163, Springer, New York.

Spear, F. S., 1993. *Metamorphic phase equilibria and pressure-temperature-time paths*. Mineralogical Society of America, Washington, D.C., Pages.

Spear, F. S. and Cheney, J. T., 1989. A petrogenetic grid for pelitic schists in the system SiO_2-Al_2O_3-FeO-MgO-K_2O-H_2O. *Contributions to Mineralogy and Petrology*, **101**, 149-164.

Spear, F. S. and Daniel, C. G., 1998. Three-dimensional imaging of garnet porphyroblast sizes and chemical zoning: Nucleation and growth history in the garnet zone. *Geological Materials Research*, **1**, 1-44.

Spry, A., 1969. *Metamorphic textures*. Pergamon Press, Oxford, Pages.

Walther, J. V. and Wood, B. J., 1984. Rate and mechanism in prograde metamorphism. *Contributions to Mineralogy and Petrology*, **88**, 246-259.

TABLE 4.1. MINERAL MODES IN STUDIED SAMPLES.

Sample Number	Qtz	Fsp	Grt[1]	Bio	Opq	Cc	Sil	Msc
711A	20	24	10	28	15	0	2	0
160A	0	16	12	40	2	30	0	0
191A	0	48	7	30	2	3	0	10

[1]Grt modes obtained from 3-D CT data (see text), other modes from petrography

TABLE 4.2. BEST GARNET ANALYSES AND END-MEMBER FRACTIONS.

Sample Number	711A		160A		191A	
	core	rim	core	rim	core	rim
SiO_2	36.9	37.0	36.9	37.0	37.5	37.25
TiO_2	0.06	0.05	0.5	0.03	0.1	0.1
Al_2O_3	20.8	20.8	20.5	20.9	20.3	20.1
FeO^1	23.8	24.1	19.7	22.8	17.2	16.9
MnO	12.2	10.6	15.4	12.6	18.4	20.1
MgO	2.0	2.5	1.2	1.7	1.4	1.5
CaO	3.8	4.8	5.1	4.5	4.6	3.0
Total	99.4	99.8	99.4	99.4	99.5	99.3
X_{alm}	0.53	0.53	0.45	0.52	0.38	0.38
X_{pyp}	0.08	0.10	0.05	0.07	0.06	0.06
X_{grs}	0.11	0.14	0.15 (0.157)	0.13	0.11 (0.149)	0.08
X_{sps}	0.28	0.24	0.35 (0.423)	0.29	0.43 (0.422)	0.47
X_{and}	0.01	0.01	0.002	0.00	0.03	0.01
Fe/(Fe+Mg)	0.87	0.84	0.90 (0.914)	0.88	0.86 (0.909)	0.86

all compositions are weight percent oxides
[1]total Fe as FeO
[2]values in parentheses are from Ferry (1980) for same hand specimens

TABLE 4.3. BEST BIOTITE ANALYSES AND END-MEMBER FRACTIONS.

Sample Number	711A wt %	160A wt%	191A wt%
SiO_2	36.7	36.7	38.2
TiO_2	2.0	1.3	1.6
Al_2O_3	17.9	19.0	18.9
FeO^1	17.1	15.1	16.2
MnO	8.9	0.3	0.53
MgO	11.4	12.4	11.2
K_2O	0.12	8.5	9.3
Total	94.0	94.3	95.8
X_{ann}	0.29	0.31	0.34
X_{phl}	0.35	0.45	0.42

[1]total Fe as FeO

TABLE 4.4. BEST FELDSPAR ANALYSIS AND END-MEMBER FRACTIONS.

Sample Number	711A wt %
SiO_2	44.6
Al_2O_3	35.2
CaO	18.8
Na_2O	0.8
K_2O	<0.009
Total	99.4
X_{or}	n.d.
X_{ab}	0.07
X_{an}	0.93

TABLE 4.5. PARAMETERS OF X-RAY COMPUTED TOMOGRAPHIC SCANNING.

Sample Number	Units	711A	160A	191A
X-ray voltage	kV	180	180	150
X-ray current	mA	0.133	0.133	0.105
Inter-slice spacing	mm	0.100	0.080	0.040
Number of slices		90	72	86
Inter-pixel spacing	mm	0.033	0.024	0.013
Field of reconstruction	mm	23.5	17	9
Wedge material		limestone	limestone	garnet
Offset	%	190	190	160
Number of views		1800	1800	3600

TABLE 4.6. PRIMARY TEXTURAL MEASURES.

Statistic	Units	711A	160A	191A
Number of crystals		2646	2545	1701
Mean crystal radius	mm	0.19	0.16	0.08
Maximum crystal radius	mm	0.42	0.34	0.14
Volume fraction		0.103	0.121	0.075
Number density	10^3 crystals/cm^3	2.7	5.6	30
Mean nearest-neighbor separation	cm	0.045	0.035	0.018

TABLE 4.7. SIMULATION PARAMETERS AND RESULT

Parameters	Units	711A	160A	191A
T_{crit}	°C	455	410	375
dT/dt	K/m.y.	10	10	10
Q_D	kJ mol^{-1}	140	140	140
$[dN/dt]_{t=0}$	Nuclei s^{-1} cm^{-3}	6.6 x 10^{-5}	1.6 x 10^{-5}	9.2 x 10^{-5}
D	cm^2 s^{-1}	1.8 x 10^{-7}	1.8 x 10^{-7}	1.8 x 10^{-7}
	K^{-1}	0.08	0.08	0.08
Q_N	kJ mol^{-1}	375	350	315
Result				
t_{95}[1]	m.y.	5.5	8.2	8.1

[1]The result " t_{95}" indicates the interval of crystallization required for 95% of the volume to be depleted such that its chemical affinity for the garnet-forming reaction decreased below the level required to nucleate new garnet. Note that Q_N, the activation energy for nucleation, is not strictly a separate input parameter, but is calculated from   and the temperature range of crystallization.
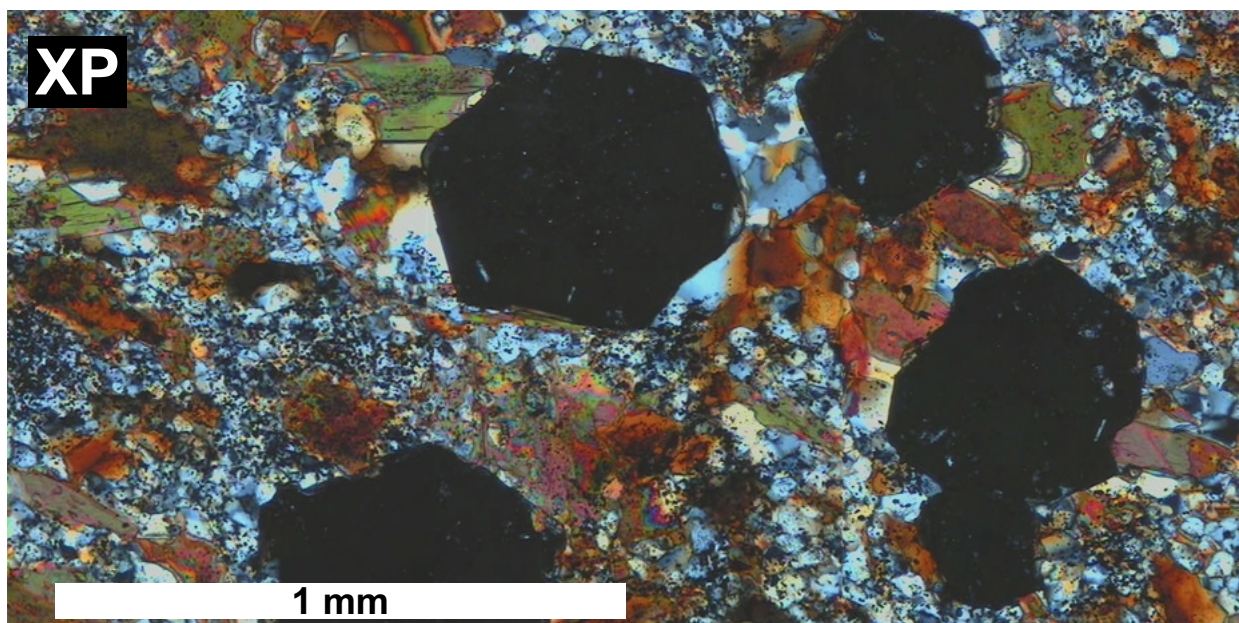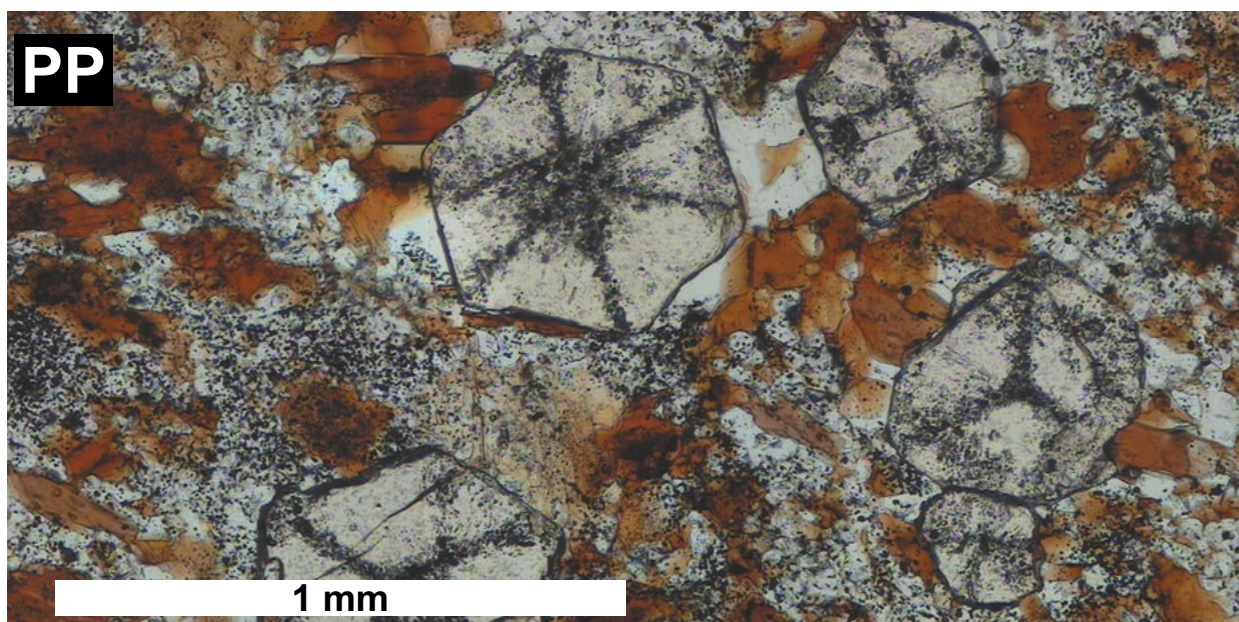
Figure 4.1. Photomicrograph of sample 711A (sillimanite zone). Assemblage is grt + bio + qtz + an + opaques + sil. The garnets are euhedral with radial inclusion patterns and little evidence of retrogression.
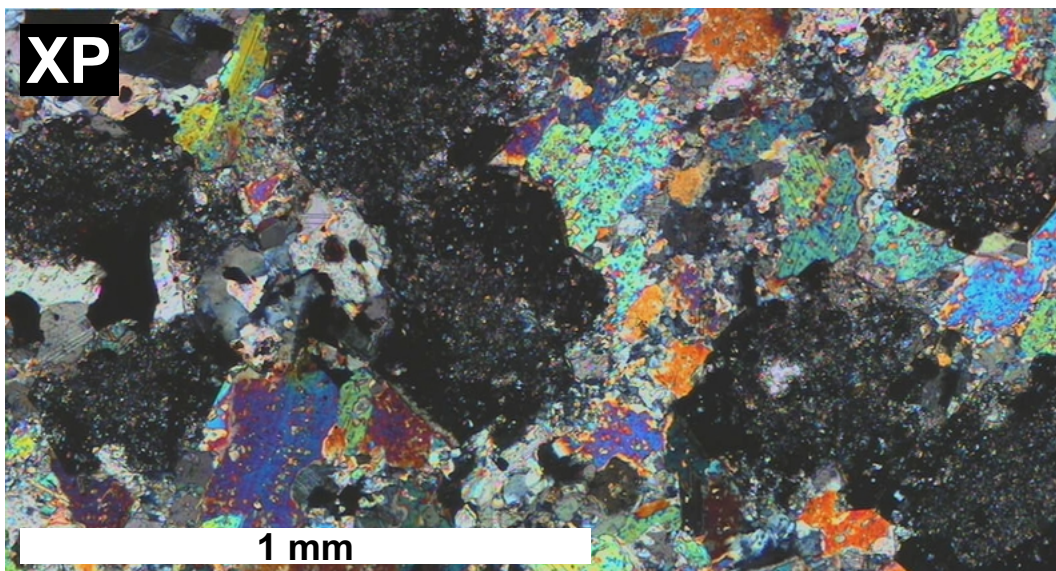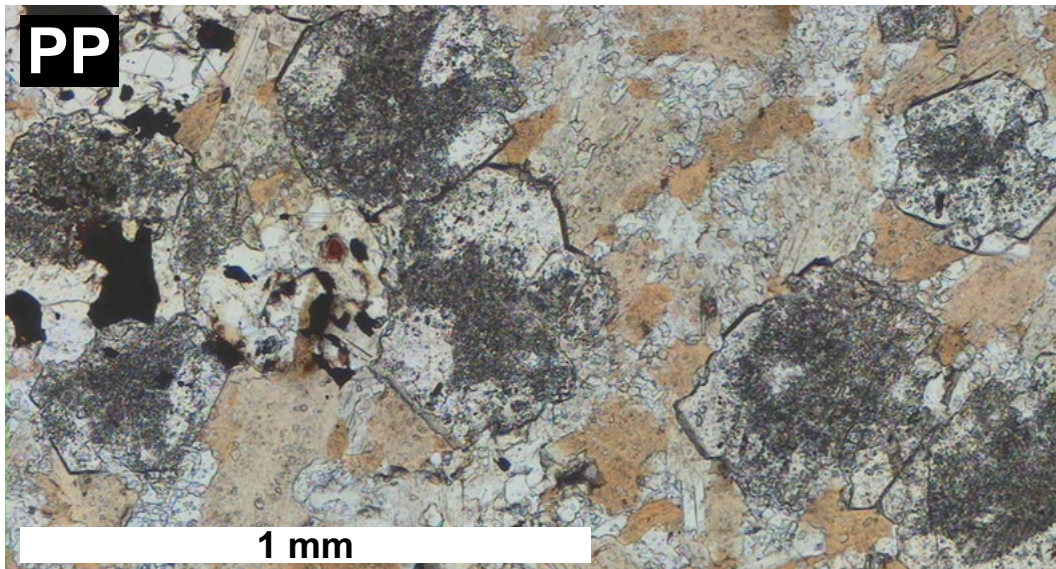
Figure 4.2. Photomicrograph of sample 160A (middle garnet zone). Assemblage is grt + bio + cc + an + opaques. Note generally euhedral to subhedral garnets with both inclusions and patchy retrogression.
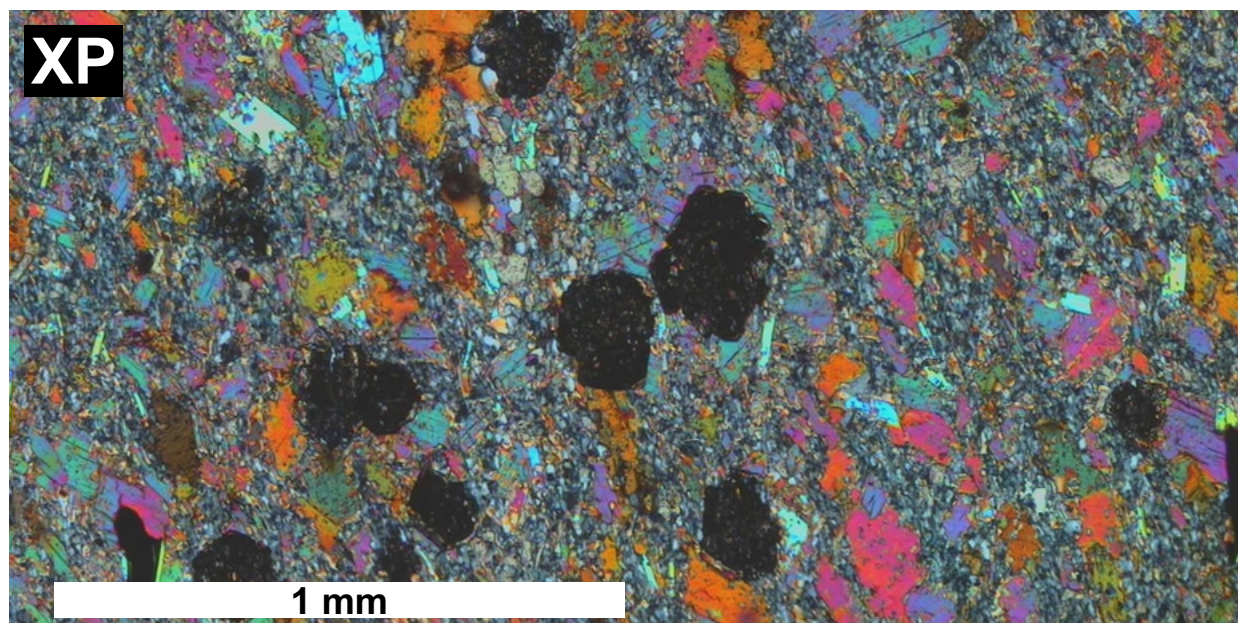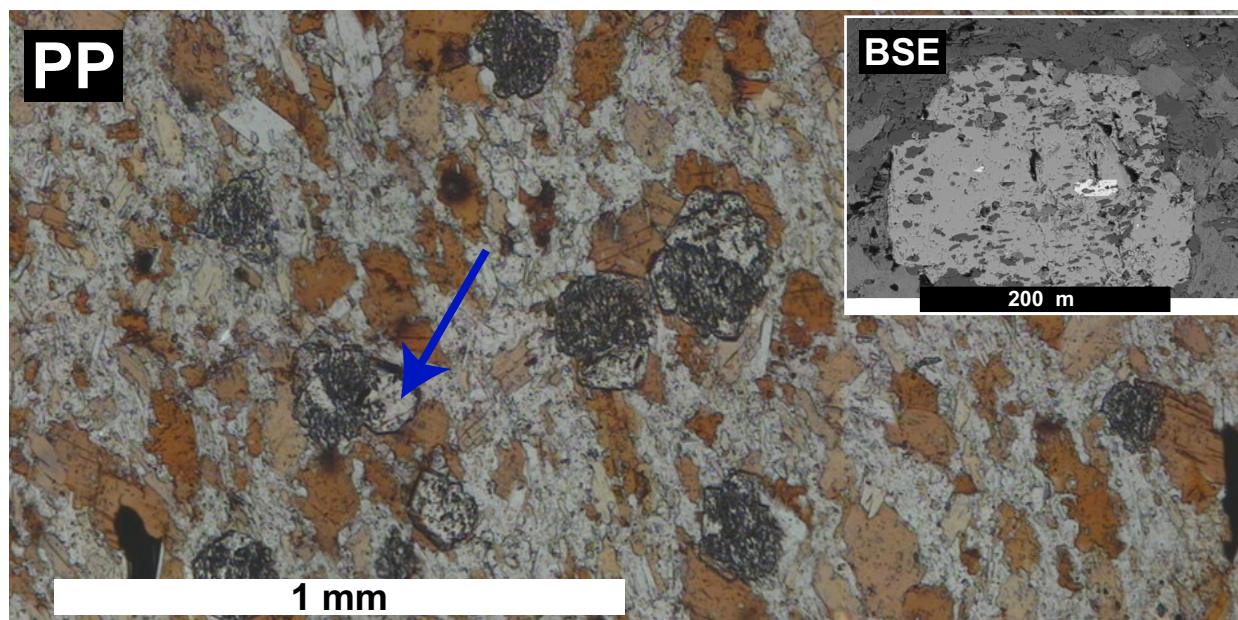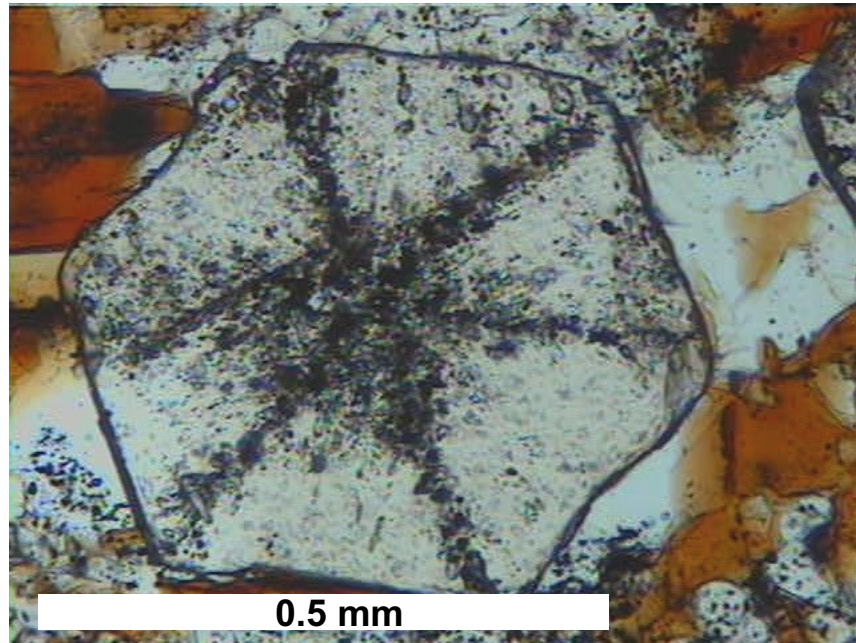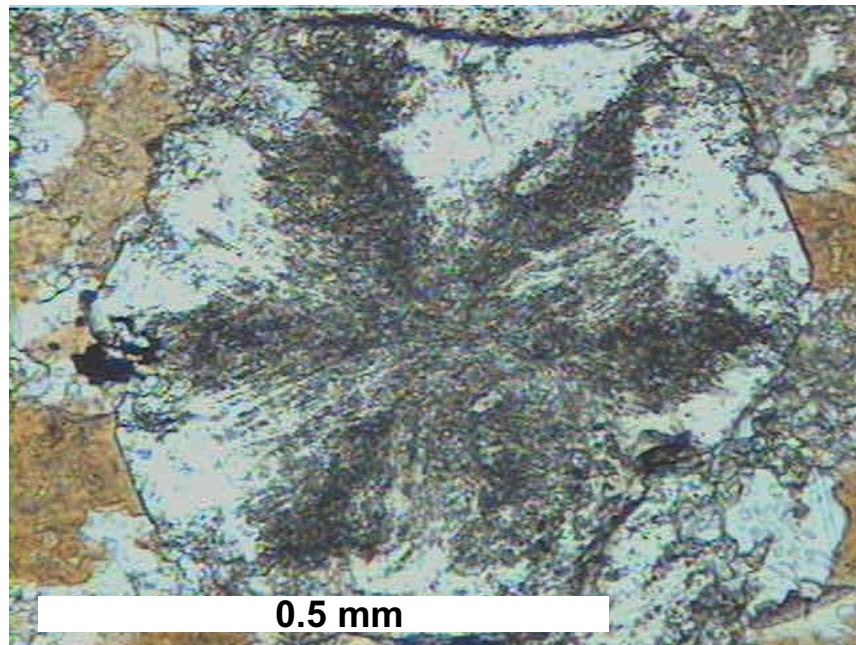
Figure 4.3. Photomicrograph of sample 191A (lowest garnet zone). Assemblage is grt + bio + msc + an + opaques. Note generally anhedral to subhedral garnets with both linear inclusion patterns (particularly evident in backscattered electron image, inset), and sparse inclusion-free subhedral to euhedral rims (blue arrow).

Figure 4.4. (a) Photomicrograph of inclusion patterns in subhedral garnet from sample 711A. Note relationship between inclusion-rich bands and crystallographic orientation, as well as varying orientation of individual inclusions within crystal. The latter effect is more prominent in (b), garnet from sample 160A (lowest garnet zone).
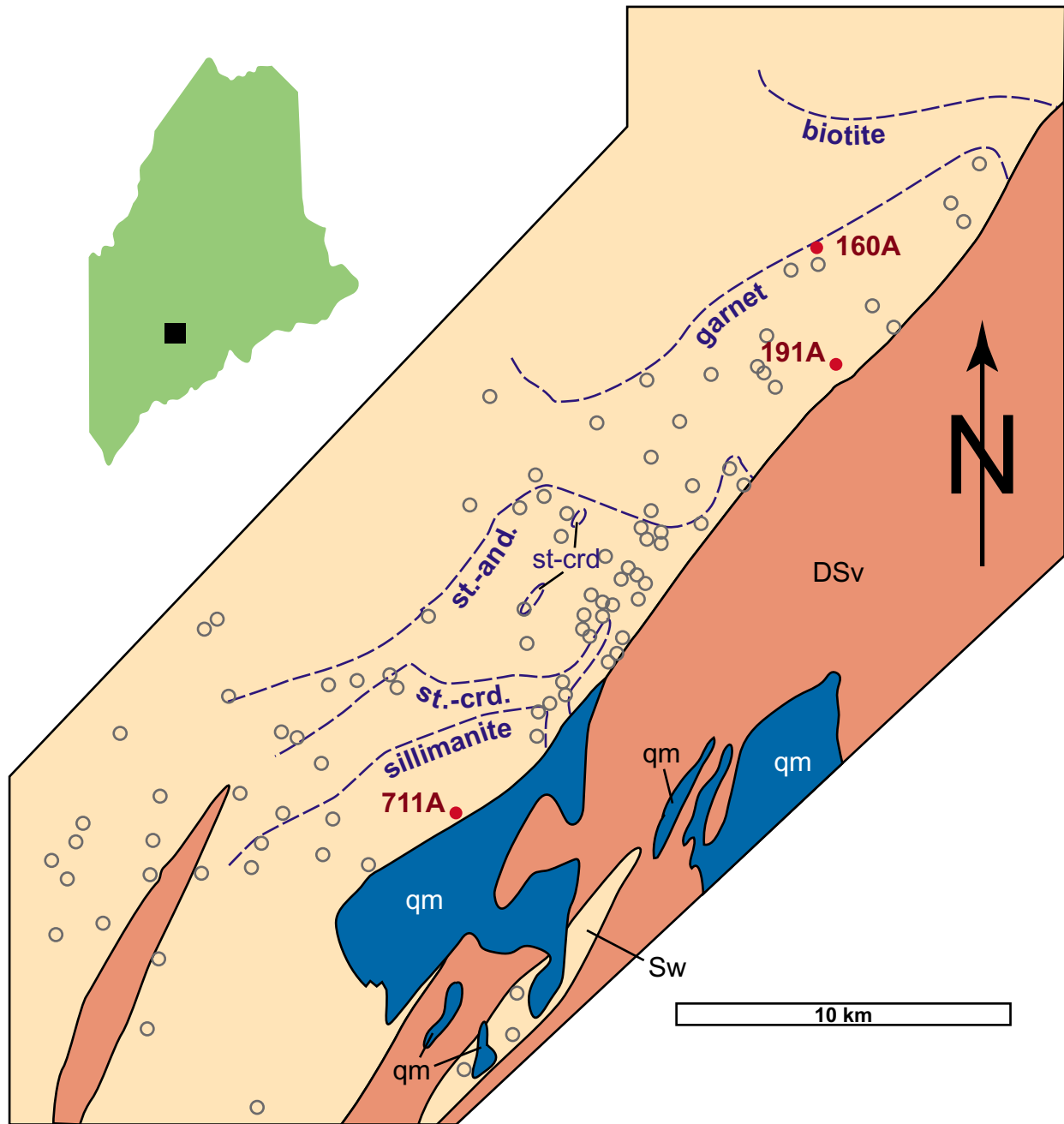
Figure 4.5. Sketch map after Barker (1961) and Ferry (1980) of sample localities in south-central Maine. DSv: Vassalboro Formation; Sw: Waterville Formation; qm: quartz monzonite. Samples for this study are indicated by red filled circles; other samples from Ferry (1980) are indicated by unfilled gray circles. Isograds are indicated by blue dashed lines with pelitic schist assemblage noted on the high-grade side. St.-and. = staurolite + andalusite; st-crd. = staurolite + cordierite.
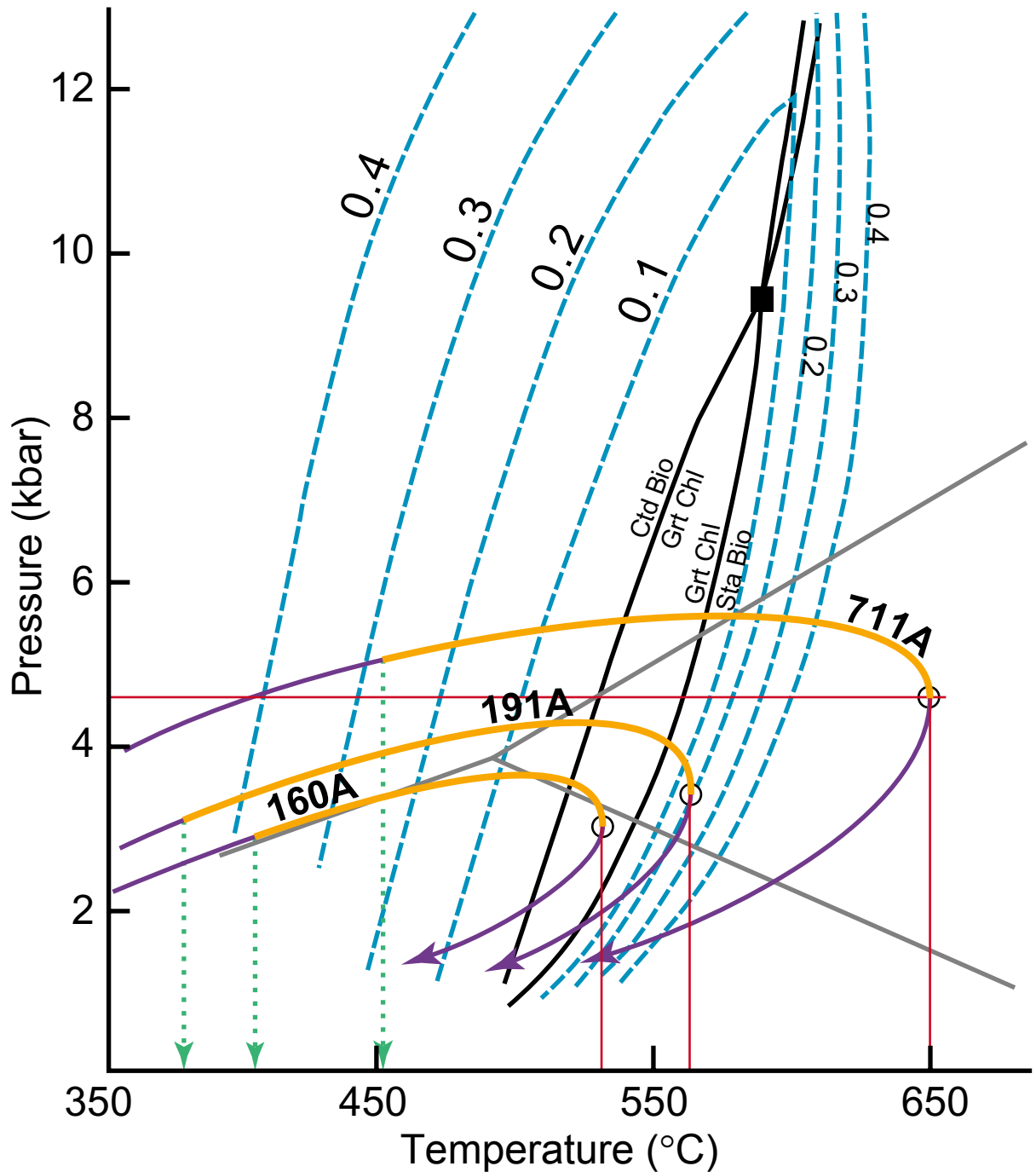
Figure 4.6. Modeled pressure-temperature ("PT") paths for studied samples (violet and gold arrowed curves). Dashed blue lines are contours of Grt + Chl stability field (relative to labeled reactions) with X_{sps} labeled (Spear and Cheney, 1989). Red horizontal and vertical lines indicate peak conditions based on garnet-biotite thermometry and garnet-aluminum silicate-quartz-plagioclase barometry. Within geothermobarometric constraints, PT paths are estimates. Critical temperatures for nucleation were obtained from the intersections of PT paths with garnet core X_{sps} isopleths, as indicated by green dotted lines. Gold regions of PT paths indicate portions of path during which garnet nucleation and growth were possible; growth after peak T is prohibited. In all simulations, crystallization is complete prior to peak T.
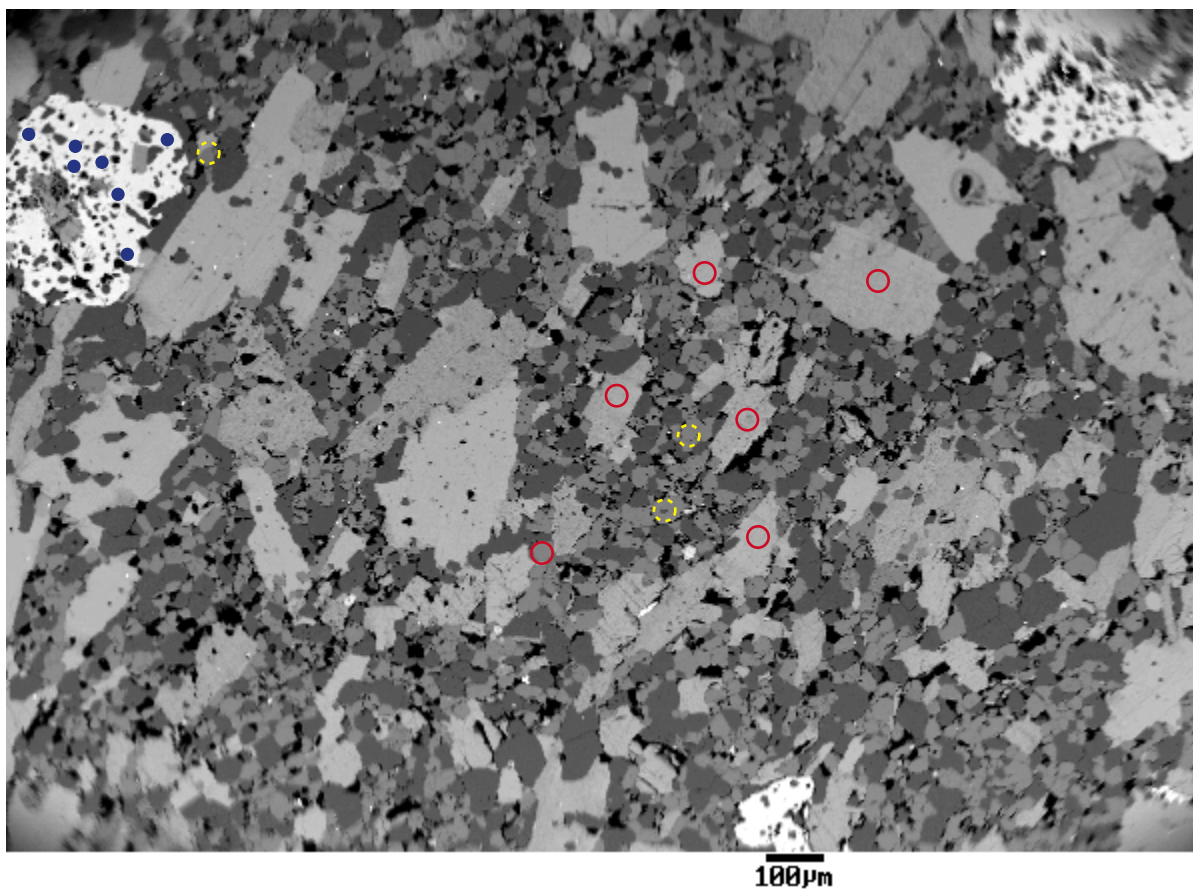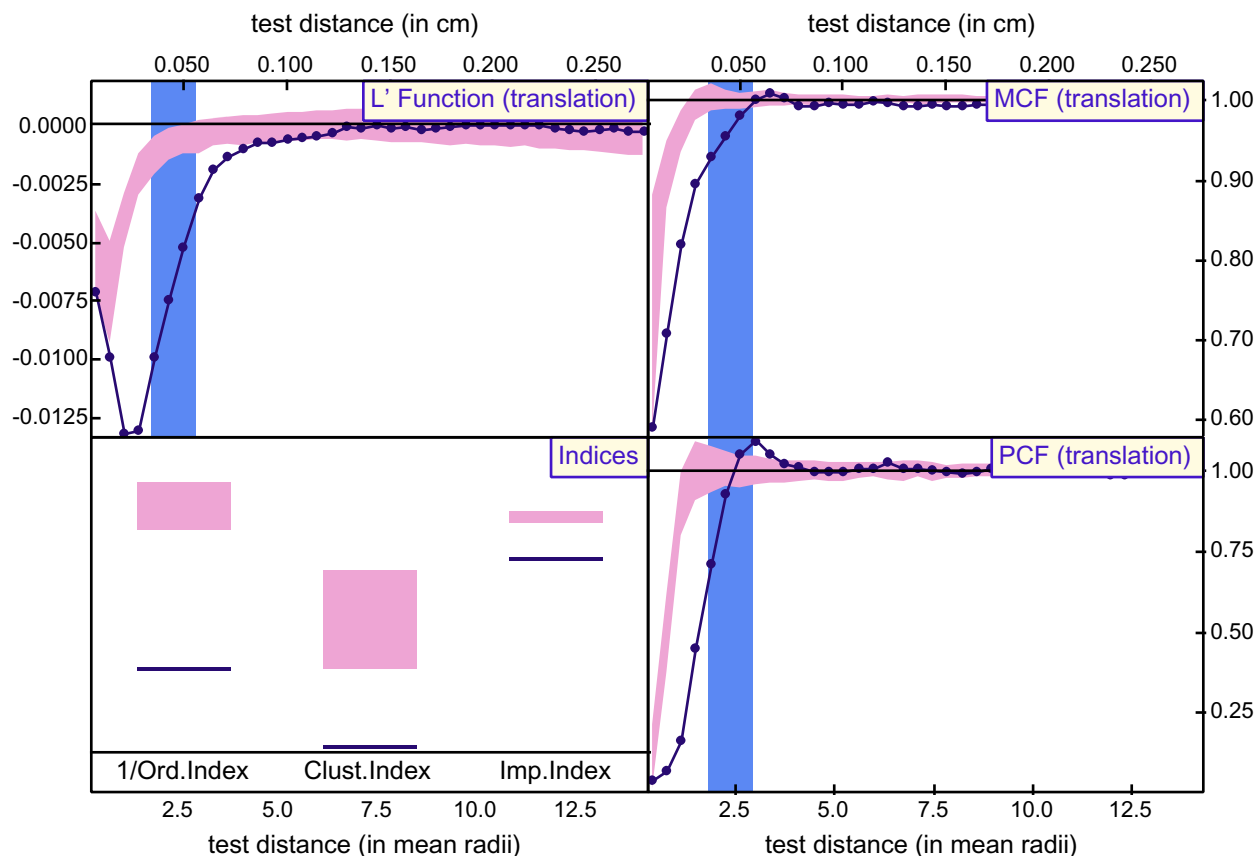
Figure 4.7. Backscattered electron map, including locations of electron microprobe analyses for sample 711A. Garnet analyses are indicated by small blue solid circles, biotite analyses by hollow red circles, and feldspar analyses by hollow yellow dashed circles.
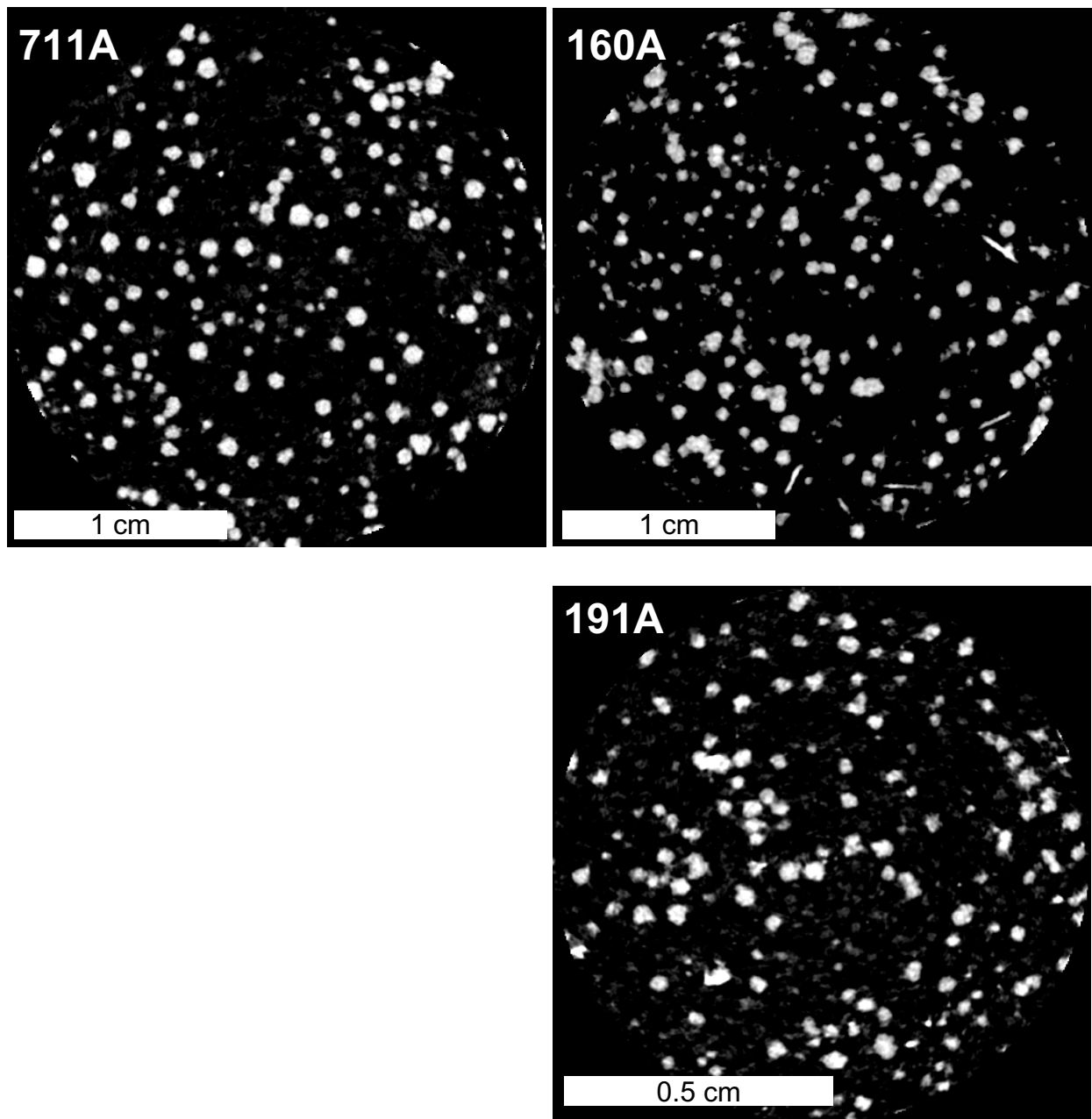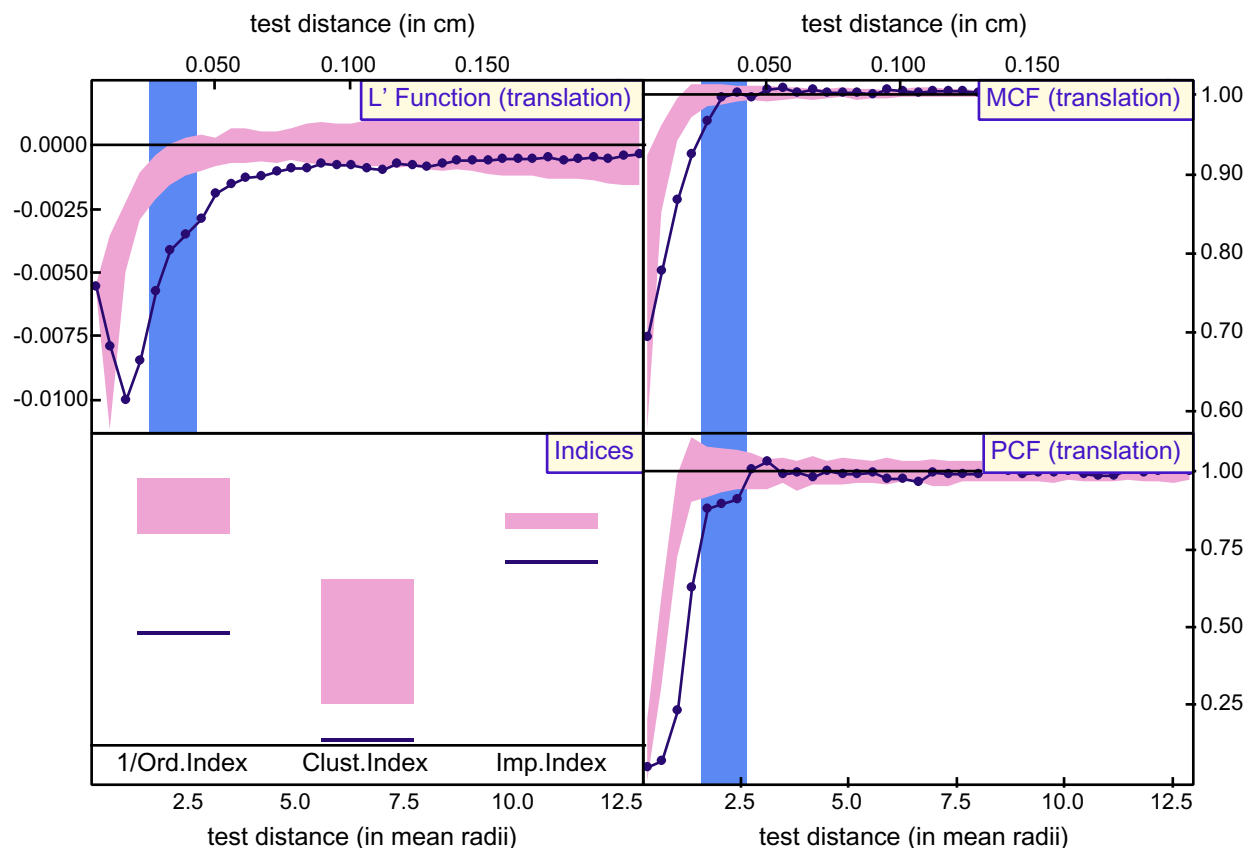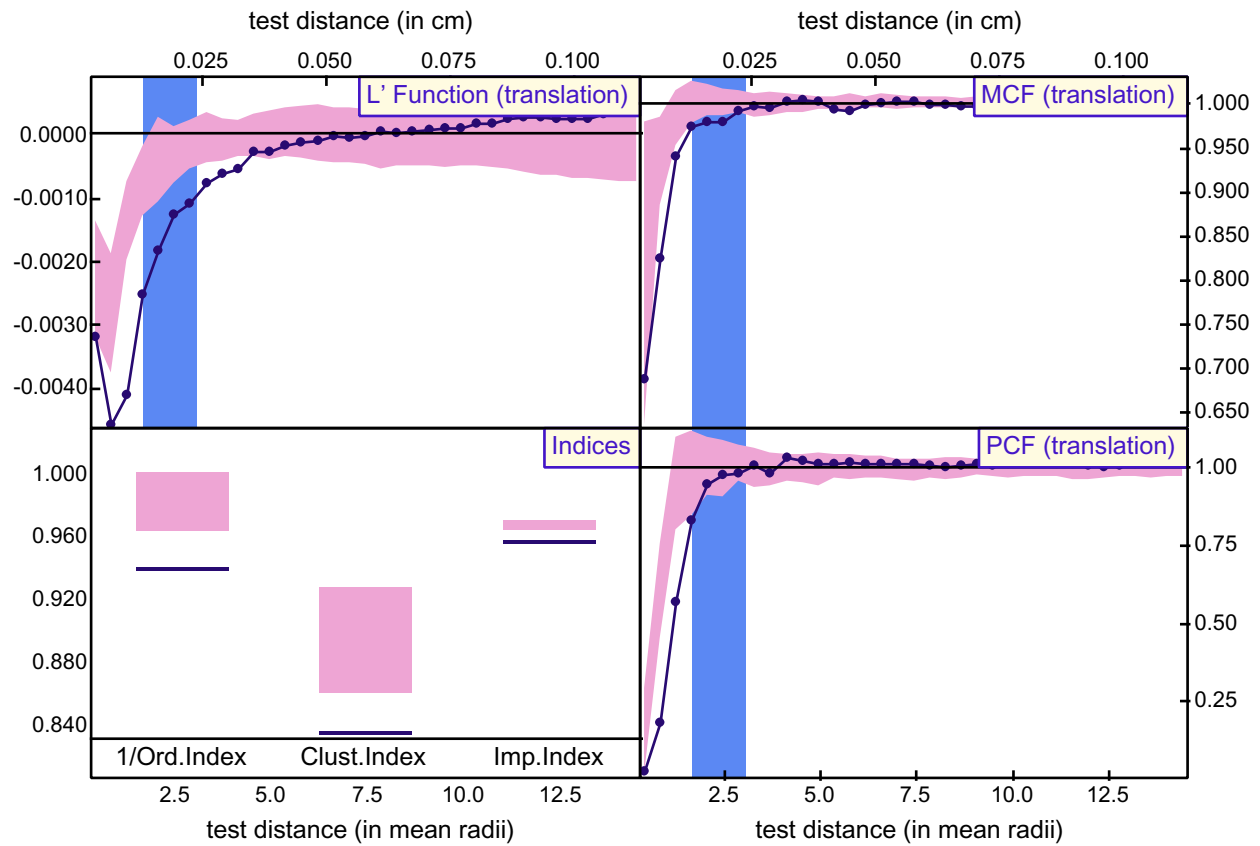
Figure 4.8. Sample X-ray computed tomographic images for each of the three specimens studied.

Figure 4.9. Statistical measures of ordering and growth suppression for sample 711A. Pink regions indicate null-hypothesis envelopes. Statistical values that fall below these regions correspond to ordering or growth suppression relative to the interface-controlled case. Results for all three indices (ordering index, clustering index, impingement index) and all three correlation functions (L' function, Pair Correlation Function, Mark Correlation Function) indicate ordering of crystal centers or suppression of growth of closely spaced crystals up to about the scale of the mean nearest-neighbor distance. Vertical blue bar corresponds to nearest-neighbor distance (center = mean nearest-neighbor distance, half-width = one standard deviation). Complete details of graphs are given in Hirsch et al. (2000).
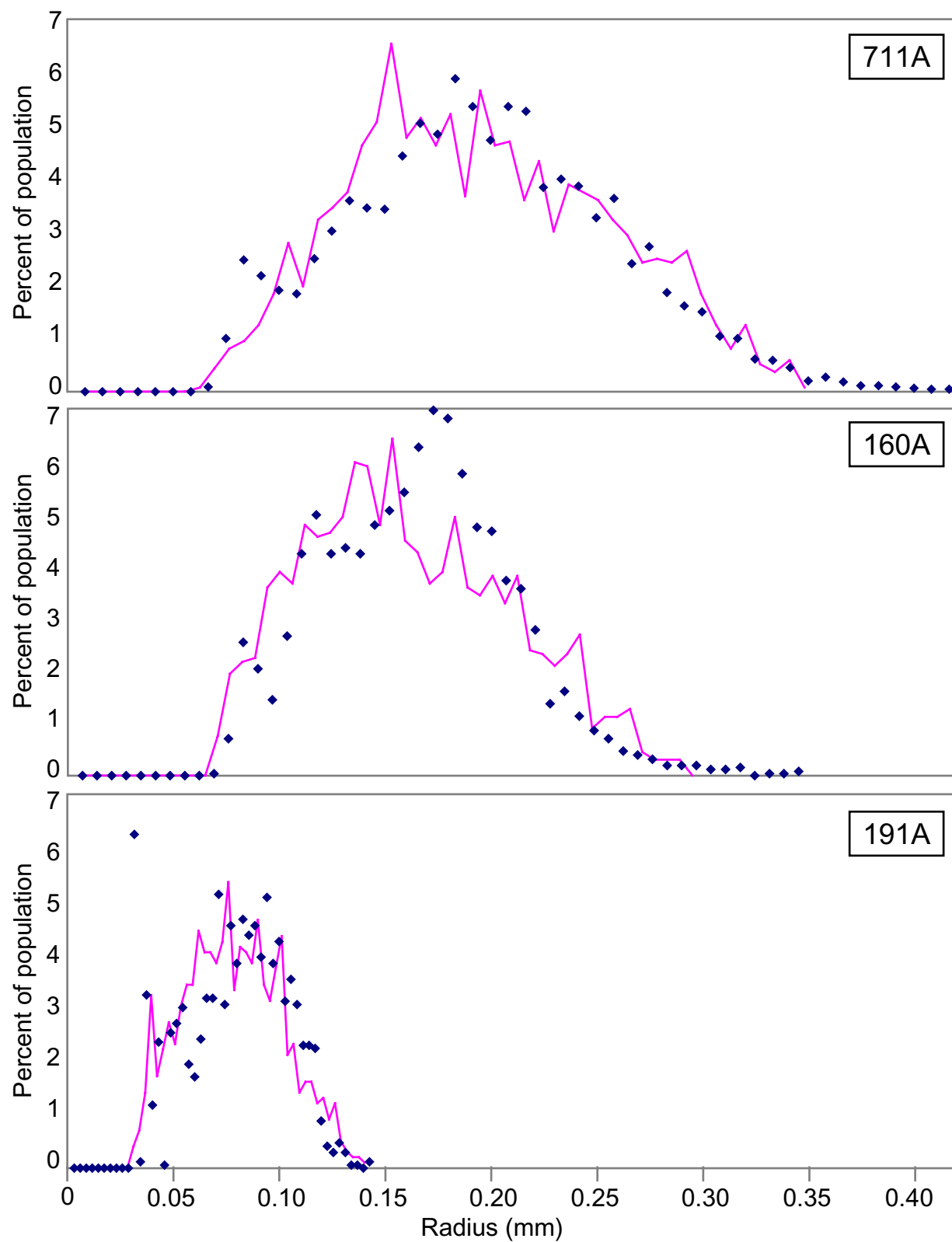
Figure 4.10. Statistical measures of ordering and growth suppression for sample 160A. Pink regions indicate null-hypothesis envelopes. Statistical values that fall below these regions correspond to ordering or growth suppression relative to the interface-controlled case. Results for all three indices (ordering index, clustering index, impingement index) and all three correlation functions (L' function, Pair Correlation Function, Mark Correlation Function) indicate ordering of crystal centers or suppression of growth of closely spaced crystals up to about the scale of the mean nearest-neighbor distance. Vertical blue bar corresponds to nearest-neighbor distance (center = mean nearest-neighbor distance, half-width = one standard deviation). Complete details of graphs are given in Hirsch et al. (2000).

Figure 4.11. Statistical measures of ordering and growth suppression for sample 191A. Pink regions indicate null-hypothesis envelopes. Statistical values that fall below these regions correspond to ordering or growth suppression relative to the interface-controlled case. Results for all three indices (ordering index, clustering index, impingement index) and all three correlation functions (L' function, Pair Correlation Function, Mark Correlation Function) indicate ordering of crystal centers or suppression of growth of closely spaced crystals up to about the scale of the mean nearest-neighbor distance. Vertical blue bar corresponds to nearest-neighbor distance (center = mean nearest-neighbor distance, half-width = one standard deviation). Complete details of graphs are given in Hirsch et al. (2000).

Figure 4.12. Crystal size distributions (blue diamonds) for the three studied samples, and for the best-fit simulations discussed in text (pink curves).
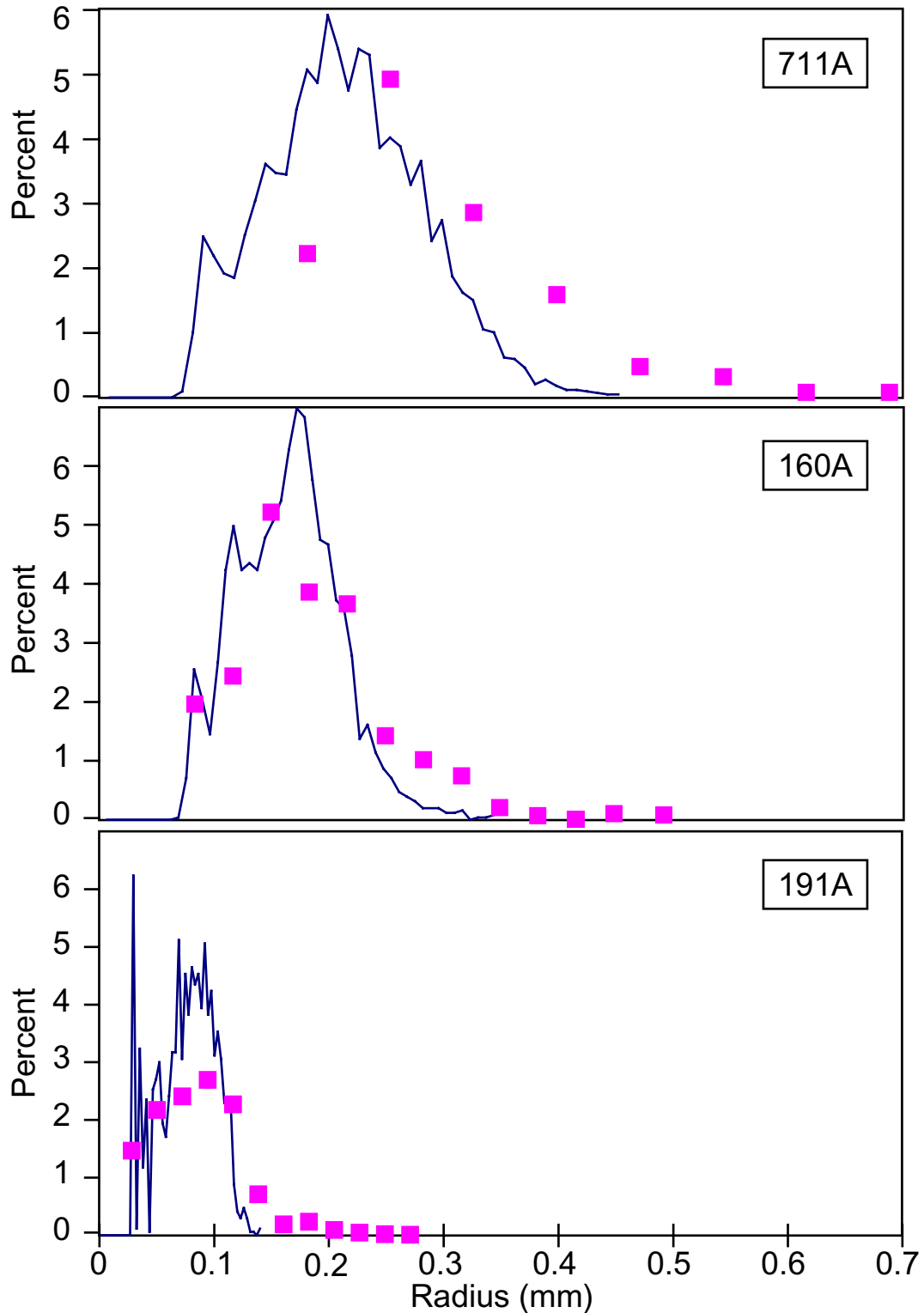
Figure 4.13. Comparison between crystal size distributions from Cashman and Ferry (1988) (pink squares) and this study (blue curve). Vertical axis is percent of population, but the values apply only to the curves, as the Cashman and Ferry (1988) ("C&F") data have been renormalized to allow comparison, given the different bin sizes in the histograms. Note significant variation between data sets for each sample.
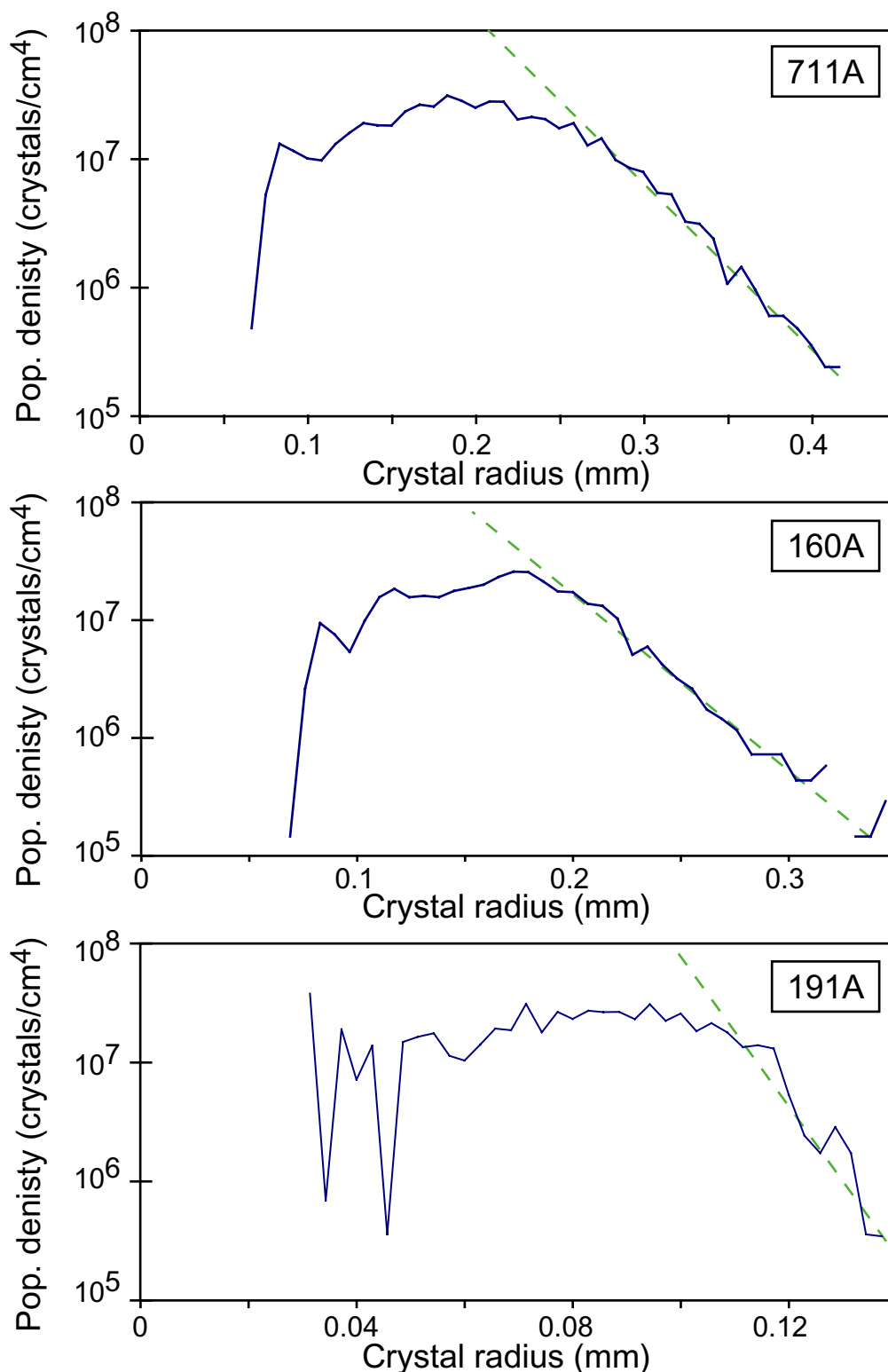
Figure 4.14. Population density function vs. crystal radius as defined by Cashman and Ferry (1988) ("C&F"). This function is defined as $n=dN/dr$, where N is the cumulative number of crystals, and r is the crystal radius. The dashed green line is an approximate fit through the linear portion of the function on this log-normal plot, and has been inferred by C&F to represent the original distribution of crystal sizes.

Appendix

Appended materials for this electronic dissertation are included as separate documents and are accessible through the following links:

Program notes and source code:

BLOB 1.5.1

INTEGRATE 2.3.3

REDUCE3D 2.5.8

RENDER3D 1.0

GRAPHCFS 1.1.4

MAKESIMULATION 1.0

Other Media

3-D interactive renderings of rock data

Data sets

3-D Computed tomographic images and processed data sets

Sample	Format
HCR2-3 (bottom)	**Directory of files**
HCR2-3 (top)	**Directory of files**
711A	**Directory of files**
160A	**Directory of files**
191A	**Directory of files**

The directories contain CT images adjusted for brightness and contrast, blob files for each image, files listing each identified 3-D object, CSD files, output from Reduce3D with statistical data, and in some cases, files listing processing or scanning parameters.

Complete raw electron microprobe data

Sample	Format	
HCR2-3 (bottom)	**Excel**	**HTML**
HCR2-3 (top)	**Excel**	**HTML**
711A	**Excel**	**HTML**
160A	**Excel**	**HTML**
191A	**Excel**	**HTML**

Note that the HTML versions of the Excel workbooks are quite complex. They will require a current browser and an extended rendering time.

Vita

David Marshall Hirsch, son of Edward M. and Judith E. Hirsch was born March 16, 1969, in Los Angeles, CA. His interest in geology began during numerous childhood trips into the Sierra Nevada batholith. He graduated from Chatsworth High School in May, 1987, and began his geologic career at the University of California, Los Angeles. Upon graduation with a Bachelor of Science in May, 1992, he enrolled in the Graduate School of the University of Texas at Austin in Fall 1992. His publications include Kuebler, K. E., et al. (1999). "Sizes and masses of chondrules and metal-troilite grains in ordinary chondrites: Possible implications for nebular sorting." and Hirsch, D. M., et al. (2000). "An evaluation of spatial correlation functions in textural analysis of metamorphic rocks." In the fall semester of 2000, he began his teaching career in earnest, instructing Earth Materials, an introductory mineralogy and petrology course at the University of Texas at Austin.

Permanent address: 22217 Romar St., Chatsworth, CA 91311

This dissertation was typed by the author.